Development of an in-flight EEE component test system with integrated radiation monitoring for TID measurement

Pedro Manuel Gom Moreira

Thesis to obtain the Master of Science Degree in

Engineering Physics

Advisor(s)/Supervisor(s): Patrícia Carla Serrano Gonçalves
Pedro Jorge Dos Santos de Assis

Examination Committee

Chairperson: Mário João Martins Pimenta
Advisor: Pedro Jorge Dos Santos de Assis
Members of the Committee: Luís Filipe dos Santos Garcia Peralta

October 2019

Acknowledgments

I would like to thank my supervisors Patrícia Gonçalves and Pedro Assis for all their help, their teaching, and specially for their guidance, since without them this work couldn't have been possible.

I'd also like to thank everyone in the SpaceRad group at LIP for all their help with this work, specially to Marco Pinto for all his help during all the phases of this work.

I extend these thanks to the LIP personal in the ECRLAB group, specially Miguel Ferreira and Zé Carlos for all their help with the experimental setup, PCB creation, component welding, and software related issues from Marco's deceased PC.

A special thanks to António Falcão and Pedro Santos from IRIS in CTN who provided the premises for the irradiation, their help during the process and even working overtime to make sure the irradiation was successful.

To all my friends who helped me during these challenging 5 years. And finally to my family who supported me and believed in me.

Abstract

Space radiation represents one of the main obstacles for space exploration, therefore it is essential to study the space radiation environment and its effects in electronic and biological systems. However, most of the current equipment for radiation measurements is relatively expensive, thus there is a necessity of low-cost detectors that can make precise measurements of the radiation environment.

In this work, several low-cost components were studied, in order to be able to identify which can be used as radiation detectors on space missions. For testing, the components were embedded in a carrier board, and irradiated up to a 100 kRad dose with a Cobalt-60 source in Campus Tecnológico Nuclear (CTN). The board also allowed to interface the components with a characterization system, a Keithley unit.

It was observed the existence of an exponential relation between the dose and saturation current of a MOSFET, both P and N channel, a linear relation between the dose and dark current of a CCD, and no apparent relation between the chosen OP-AMPs and photodiodes.

Keywords: Commercial Off The Shelf Components, Low Cost Radiation Detectors, Irradiation, Total Ionizing Dose, Radiation Effects on Semiconductors

Resumo

A radiação espacial representa um dos principais obstáculos para a exploração espacial, pelo que é essencial caracterizá-la durante todas as fases duma missao. No entanto, a maior parte do equipamento de medição actual é relativamente caro, pelo que há necessidade de detectores de baixo custo que consigam ter resultados precisos.

Neste trabalho, foram estudados vários componentes de baixo custo de modo a identificar se poderão ser usados como detectores de radiação em missões espaciais. Para este efeito, foi desenvolvida uma placa onde os vários componentes são inseridos e medidos durante uma irradiação com fonte de Cobalto-60 até uma dose de 100 kRad, realizada no Campus Tecnológico Nuclear (CTN).

Foi observada a existencia de uma relação exponencial entre a dose e a corrente de saturação de MOSFETs do tipo P e do tipo N, uma relação linear entre a dose e a corrente negra de saída do CCD, e não se encontrou nenhuma relação entre os OP-AMPs e fotodíodos escolhidos.

Keywords: Componentes Comerciais, Detectores de Radiação de Baixo Custo, Irradiação, Dose Total Ionizante, Efeitos da Radiação em Semicondutores

Contents

List of Tables

List of Figures

Acronyms

CCD Charge Coupled Device. 2, 3, 5, 15, 18, 24, 25, 27, 28, 45

CMOS Complementary Metal-Oxide-Semiconductor. 3

COTS Commercial Off-The-Shelf. 1, 2, 5, 18, 21, 31, 45

EEE Electric, Electronic and Electromechanical. 1, 15, 21, 27

EHP electron-hole pairs. 3, 4, 17

ESA European Space Agency. 1, 2

GCR Galactic Cosmic Radiation. 8, 11–13

GEO Geostationary Earth Orbit. 13

LET Linear Energy Transfer. 7

LIP Laboratório de Instrumentação e Física Experimental de Partículas. 1, 21

MEO Medium Earth Orbit. 13

MOS Metal-Oxide-Semiconductor. 2, 20

MOSFET Metal-Oxide Semiconductor Field-Effect Transistor. 2, 3, 5, 18, 20–22, 28, 31, 33, 45

OP-AMP Operational Amplifier. 4, 5, 20, 22, 23, 28, 45

RADFET Radiation-Sensitive Metal-Oxide-Silicon Field-Effect Transistor. 2

SEE Single Event Effects. 15

SEP Solar Energetic Particle Event. 9, 11

SMU Source Measure Unit. 21

TID Total Ionizing Dose. 3–5, 13, 15, 16, 18, 19, 27, 45

VAB Van Allen Radiation Belts. 11–13, 26

Chapter 1

Introduction

1.1 Motivation

Space exploration is a fundamental part for the progress of our society. While the common folk may be unaware, multiple applications from communication to navigation were only possible due to advances in space research.

The space radiation environment presents itself as one of the main obstacles for space exploration. The risks that radiation represents affect directly the mission planning, and therefore the knowledge of these values, during every phase of a mission, is essential. As our presence in space and its exploration tend to increase, space radiation becomes an important obstacle to overcome.

While the combination of certain conditions, such as the large temperature modulations, low pressure and harsh radiation environment can make it exceedingly hard for continuous instrument operation, radiation can hasten the degradation of Electric, Electronic and Electromechanical (EEE) components and lead to partial or total failure of instruments.

For unmanned missions, cost plays a huge role, therefore new and more viable strategies are required in order to ensure a high quality space research at a lower price. A possible strategy, for developing more cost efficient missions, is through the implementation of high quality Commercial Off-The-Shelf (COTS) components, which are known for being very cheap for the high quality that they present. However, one of their disadvantages is due to the fact that there is still little information about their tolerance to the radiation found in the space environment, since it is expensive to qualify them. Another one, is the fact that since they're commercial, one cannot easily determine which ones are from the same batch, since they may behave slightly different depending on how and where they were manufactured.

The European Space Agency (ESA) has been supporting the development of the state-of-the-art and high innovative technology demonstration Modules for In-Orbit Demonstration, and this work will be performed with the "Space Radiation Environment and Effects Group" from "Laboratório de Instrumentação e Física Experimental de Partículas (LIP)", in the framework of its activities with ESA.

1.2 State Of The Art

The first influence of radiation on electronic components was discovered during the nuclear bomb tests, where several malfunctions were observed in the measuring equipment. These malfunctions were mainly caused by the neutron single event effects and the modification of important parameters of those components by the gamma radiation. Since then, further anomalies have been detected in electronic systems in space. By measuring those anomalies it may be possible to correlate the gamma radiation a system was exposed to, with its electrical parameters modifications.

Currently there are studies on several COTS components that could be used to detect radiation, where the most notable are Charge Coupled Devices (CCDs), Metal-Oxide Semiconductor Field-Effect Transistors (MOSFETs) and photodiodes. For Metal-Oxide-Semiconductor (MOS) components, ESA has been trying to analyze their response to different values of absorbed radiation doses. Some results are presented in the plots of figure 1.1 from [11].

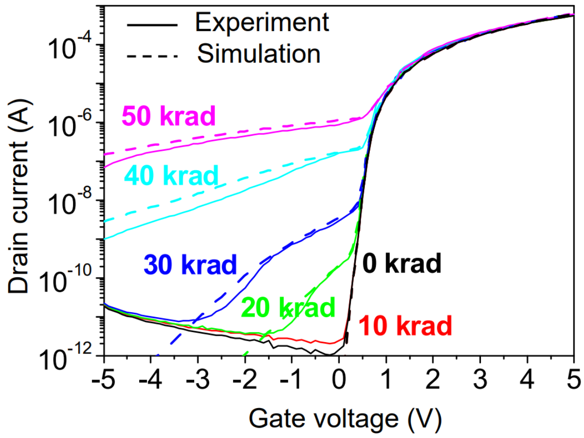

(a) Charge buildup in the CMOS field oxides causes increase of the leakage current (Ferlet HDR05)

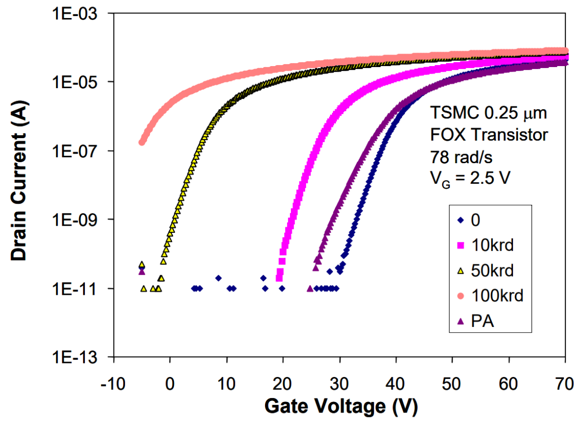

(b) Another radiation-induced leakage current (R. C. Lacoe, et. al. TNS Dec. 2000)

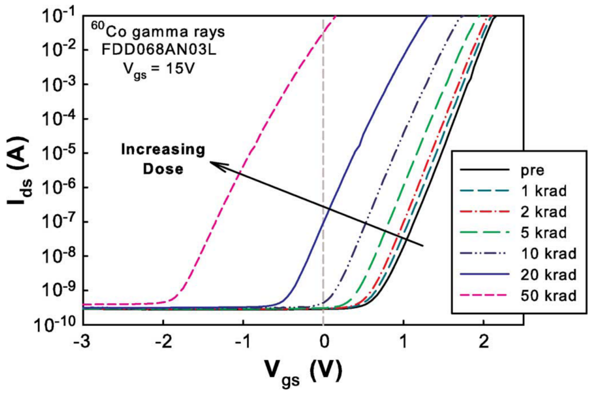

(c) Increasing total ionizing dose effects in a power MOSFET (Shaneyfelt et. al., TNS 2008)

Figure 1.1: Change of the system's parameters with the amount of absorbed radiation (where 1 kRad is equal to 10 Gy).

Some more results are presented in figure 1.2 from [4].

From the previous results, there is a noticeable degradation of the threshold voltage, leakage current and most importantly, a shift of the i-v curves.

There is also the Radiation-Sensitive Metal-Oxide-Silicon Field-Effect Transistor (RADFET), a type of MOSFET with enhanced thickness of the SiO_2, that allows the monitoring of radiation, with a small volume, simple circuits, low power and gives a DC output as analyzed in [12]. They are based on the principle of converting threshold voltage shifts into absorbed dose. However, like the normal MOSFET, they are temperature sensitive and vulnerable to neutrons.

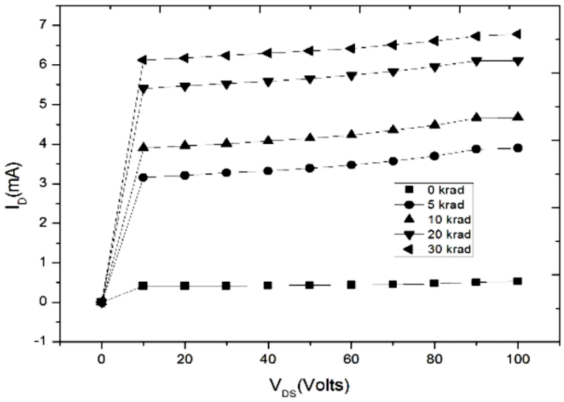

(a) Output characteristics of MOSFET 2N6796.

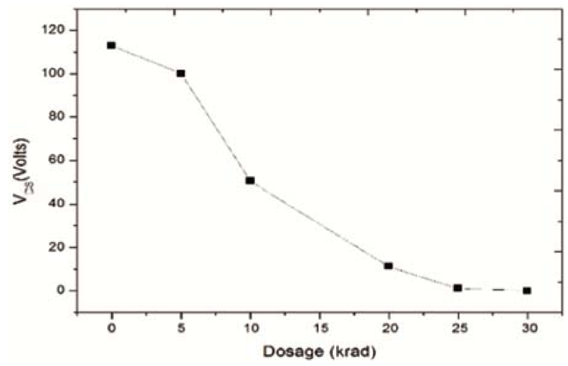

(b) Plot of V_{DS} as a function of gamma dose for a MOSFET 2N6796.

Figure 1.2: Dependency of some electrical parameters of MOSFET 2N6796 with the gamma dose as seen in [4].

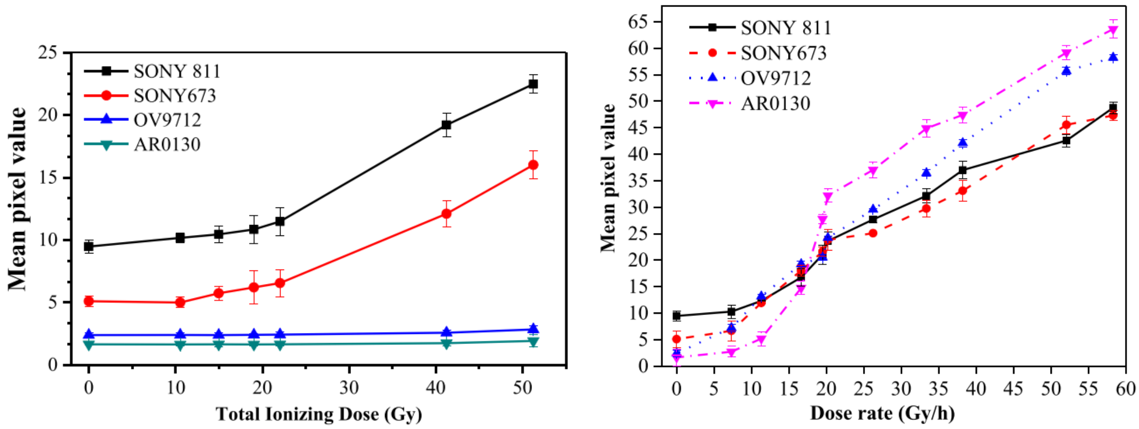

Figure 1.3: Mean pixel value as a function of the Total Ionizing Dose (at 20.27 Gy/h) and Dose rate, as obtained in [5]. The SONY models are CCDs while OV and AR are CMOS.

According to [5], where they analyzed the number of active pixels of CCDs and Complementary Metal-Oxide-Semiconductor (CMOS) based on the absorbed dose (figure 1.3), we have some insights on the suitability of both these components. Radiation damage of CCDs causes dark currents and shifts their i-v plots, just like the MOSFETs, which is one of the parameters that we can measure to find the Total Ionizing Dose (TID) the component has absorbed.

According to their research, where they compared dark images before and after the irradiation, CMOS has less background noise than CCDs, however they are less sensitive to the increase of TID, being more radiation resistant. The background noise results from only a part of the radiation's energy being transferred to the electron by the Compton effect.

Since CMOS exhibit a steeper peak-shaped slope, they're more suitable for particle classification, while CCDs have a low peak value so they're better for energy resolution.

Also, in [13] we can see that CCDs has a higher power consumption and a different data retrieval mechanism, and some other comparisons between both components and models.

Photodiodes present a better sensitivity when compared to other devices, due to their fast response, high ruggedness and small dimensions, and the low energy required to produce electron-hole pairs (EHP), however, their output current is very small. Alpha particles and low energy beta particles are blocked by the plastic encasing, while the gamma rays and high energy betas will pass through and create the EHP in the diode's depletion layer. If it's being applied a voltage, the charge carriers will be drawn away and result in a small current pulse.

There are mainly two different types, the PIN diode and the PN diode, where the former has an extra layer, with a lightly N-doped region called the intrinsic region, which results in a wider depletion layer, allowing a greater volume of semi-conductor that can interact with the radiation. A prototype can be seen in [14] and a GEANT4 simulation in [15].

The TID will also increase the dark current in a photodiode, however, according to [6], there are no significant effects for values below 500 Gy, since photodiodes are not very sensitive to ionizing effects due to the lack of an oxide layer to trap charged carriers and generate observable TID effects. As such, it is not expected to observe a significant effect for TID. In figure 1.4, we can verify the low sensitivity of these type of components compared to the previous components.

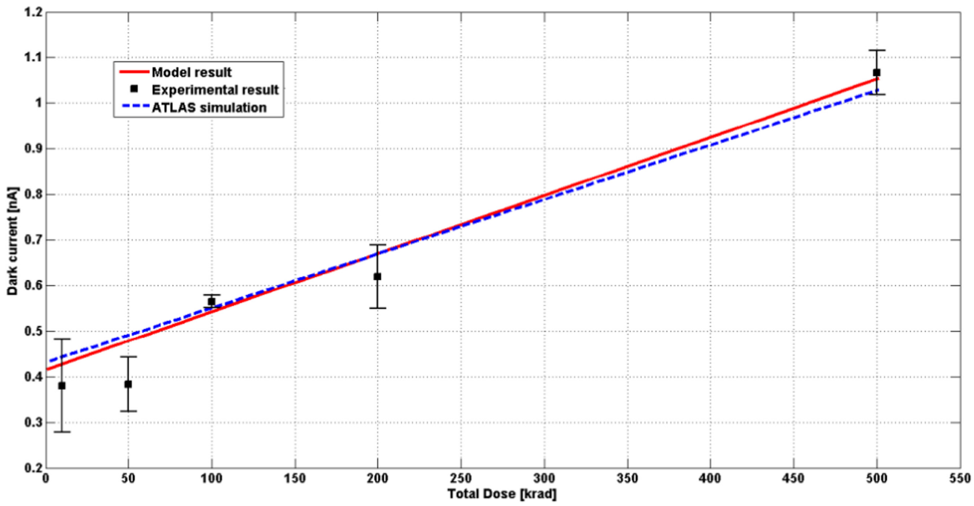

Figure 1.4: Dark current as a function of TID for a 20V voltage, fitted for their model, experimental results and an ATLAS simulation [6].

Certain types of RAM such as NVRAM and SRAM can be used for the same effect as explained and tested in [16].

Another alternative could be the use of Operational Amplifiers (OP-AMPs) ([7, 17]), since radiation can also affect some of their parameters as seen in figure 1.5, such as frequency responses, slew rate, closed loop gain, offset input voltage and current and others.

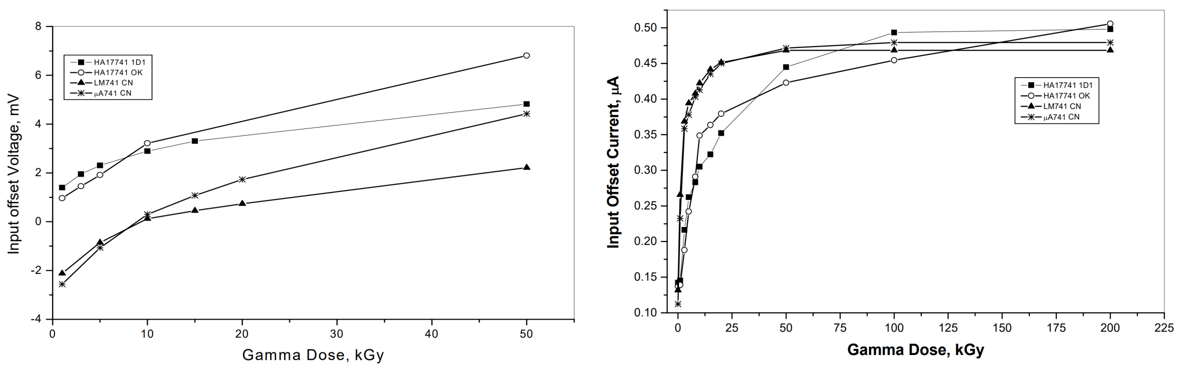

Figure 1.5: Input Offset voltage and current dependency with the dose as seen in [7].

1.3 Objectives

Most of the current equipment for space radiation monitoring is very costly, making it a big loss when they fail since it's very expensive to send a replacement.

Therefore, there's a need for low-cost radiation detectors that can still have precise measures, can be mass produced and sent to space as cheaply as possible.

As previously mentioned, COTS technology can be a solution for this problem. They're defined as non-developmental items sold in the commercial marketplace, tailored for specific uses and made available to the general public. Such products are designed to be readily available and user friendly. A COTS product is generally any product available off-the-shelf and not requiring custom development.

This work seeks to develop a cheap test system (or at least a proof of concept) for monitoring of space radiation, that can measure the TID during flight, and developed using COTS technology, in order to be able to fly in a Cube Sat (which implies a size of a 10 cm sized cube and lighter than 1.33 kg). The test system will integrate several different components in order to have some redundancy, and possibly to inter-calibrate itself. This test system will be irradiated and tested under a Cobalt-60 radiation source in order to characterize its effects. By having these characterization curves, it'll be possible to estimate the radiation dose a component has absorbed while in a space mission, by measuring these effects on the components.

The components used shall be an N and P type MOSFET, a photodiode, a CCD and an OP-AMP. Unlike other works, the MOSFET will measure the dependency of the saturation current with the dose rather than the threshold voltage, for the photodiode, the saturation currents will be checked for any permanent radiation damage rather than small pulse measuring during irradiation, for the CCD it shall be measured the dark current and average pixel voltage instead of individual pixel analysis, and for the OP-AMP it shall be measured the input offset for both voltage and current in a voltage follower circuit rather than a frequency response.

Chapter 2

Space Radiation Environment

Since the main objective of this thesis is measuring space radiation, it is important to first know what types of radiation are expected to find in space, their origin and characteristics.

Radiation is the emission or transmission of energy in the form of particles or waves traveling through space, or a material medium. For an isotropic source, its power follows an inverse-square law according to its distance.

2.1 Basic Concepts

Table 2.1 provides a brief overview of relevant physical concepts and definitions.

Concept	Equation	Unit	Description
Fluence (ϕ)	$\phi \equiv \frac{N}{A}$	m^{-2}	Fluence is defined as the number of particles (N) that cross over an area (A).
Fluence Rate ($\dot{\phi}$)	$\dot{\phi} = \frac{d\phi}{dt}$	m^{-2} s^{-1}	The therm "Flux", more correctly known as Fluence Rate, is the number of particles (N) that cross over an area (A) in a certain time interval (t).
Linear Energy Transfer (L_Δ)	$L_\Delta = \frac{dE_\Delta}{dL}$	keV/μm N (SI)	The Linear Energy Transfer (LET) is defined as the mean energy lost by the charged particles due to electronic interactions while traversing a distance (L), excluding the secondary electrons with kinetic energies larger than a certain value Δ.
Absorbed Dose (D)	$D = \frac{d\bar{E}}{dm}$	J kg^{-1} Gy (SI)	The absorbed dose is a measure of the amount of energy a body has absorbed. It's defined as the mean energy, $d\bar{E}$, imparted by an ionizing radiation to a body of mass dm.

Table 2.1: Brief overview of relevant physical concepts.

2.1.1 Types of Radiation

Radioactive sources produce ionizing radiation. This ionizing radiation is composed by electrons and positrons, both from beta$^-$ and beta$^+$ decay and internal conversion processes, alpha particles (helium-4 nuclei), gammas (high energy photons) and X-rays. The two former have a high LET, stopping quickly when traveling through a material, while the two latter can travel longer distances before being absorbed.

Non-Ionizing vs Ionizing

Radiation can be divided into two types, according to their interaction with matter. They can be classified into ionizing or non-ionizing based on having sufficient energy to ionize an atom or not, respectively.

Ionizing radiation refers to charged and uncharged particles that can produce ionization in a medium or initiate a reaction that results in ionization or the production of ionizing radiation.

2.2 Galactic Cosmic Radiation (GCR)

Galactic Cosmic Radiation (GCR) are extra-terrestrial particles that originate within our galaxy but outside our solar system. They're composed of highly energetic and penetrating ions believed to be accelerated by supernova in our galaxy. While mostly consisting of protons (85$\%$ to 90$\%$) with energies extending up to 10^{21} eV, there is also a component of heavier nuclei, predominantly Helium (9$\%$ to 14$\%$), all the way up to Iron ($<$1$\%$).

This radiation is an isotropic and continuous source that is inversely correlated to the solar activity, as seen in figure 2.1. This is due to the fact that at a solar activity maximum, the Sun's magnetic field is more intense, creating a GCR shielding effect, where the lower energy particles cannot penetrate our solar system easily, as seen in the spectrum of the GCR as a function of minimum and maximum solar activity in figure 2.2.

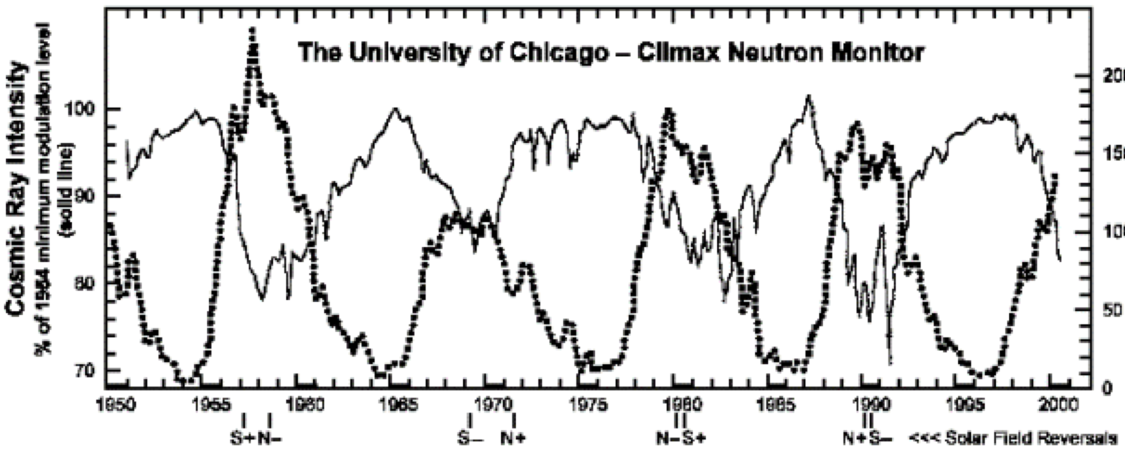

Figure 2.1: Inverse correlation between solar activity and GCR fluence [8].

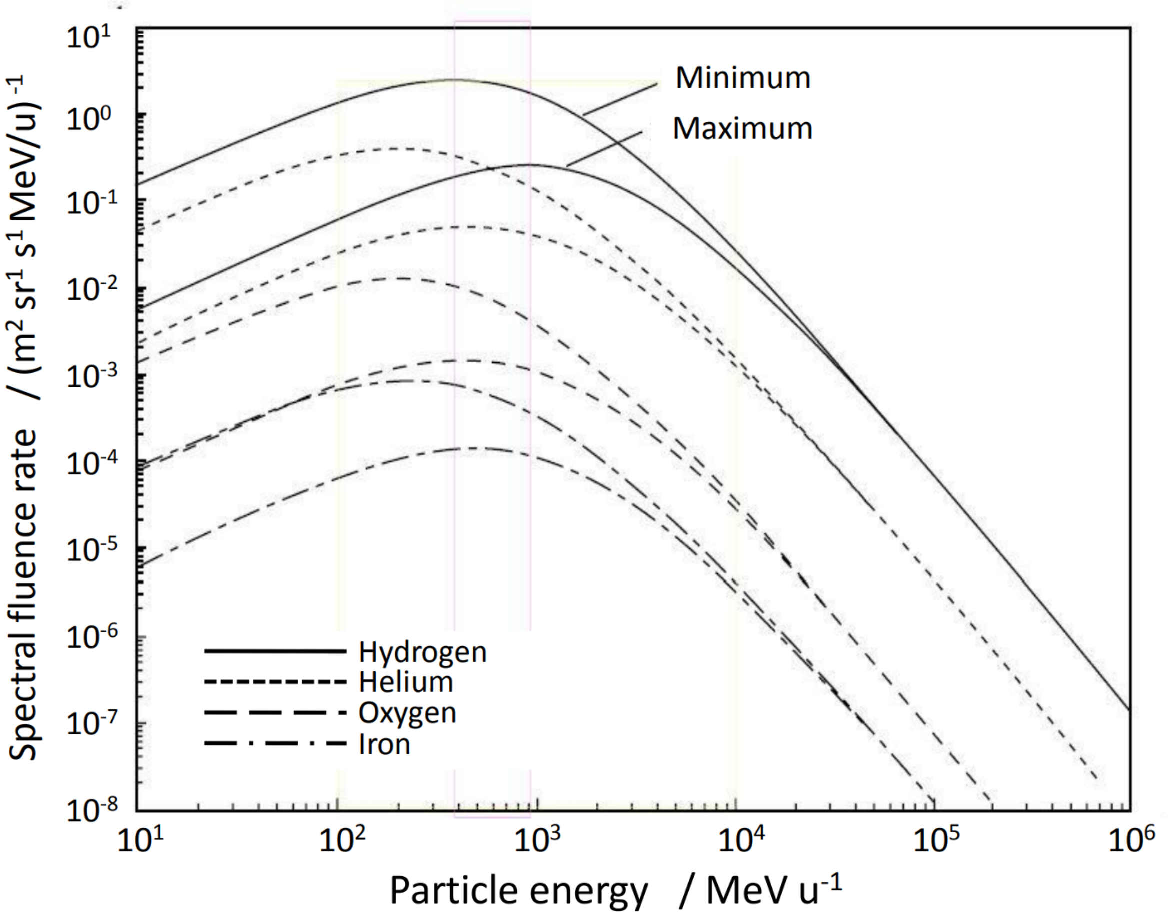

Figure 2.2: Energy distribution of fluence rate versus particle energy for a solar minimum and maximum at 1 AU [9].

2.3 Solar Energetic Particle Events (SEP)

The Sun is constantly emitting radiation, the solar wind, which is mostly comprised of protons and electrons. These particles have low energy (100 to 3500 eV for the protons). This solar wind originates the heliosphere, composed of plasma and its magnetic field. This magnetic field fluctuates with an average eleven year period between maximum and minimum of solar activity as seen in figure 2.3 .

Occasionally, energetic particles are ejected by a solar eruption, with a large fluence rate. This is known as a Solar Energetic Particle Event (SEP). These events are caused by coronal mass ejections and solar flares. These phenomena accelerate charged particles from the solar corona up to a few Gev with very high fluxes, while emitting γ, X and radio waves in a large bandwidth frequency, with high energies. Examples of events for each of these two types can be seen in figure 2.4.

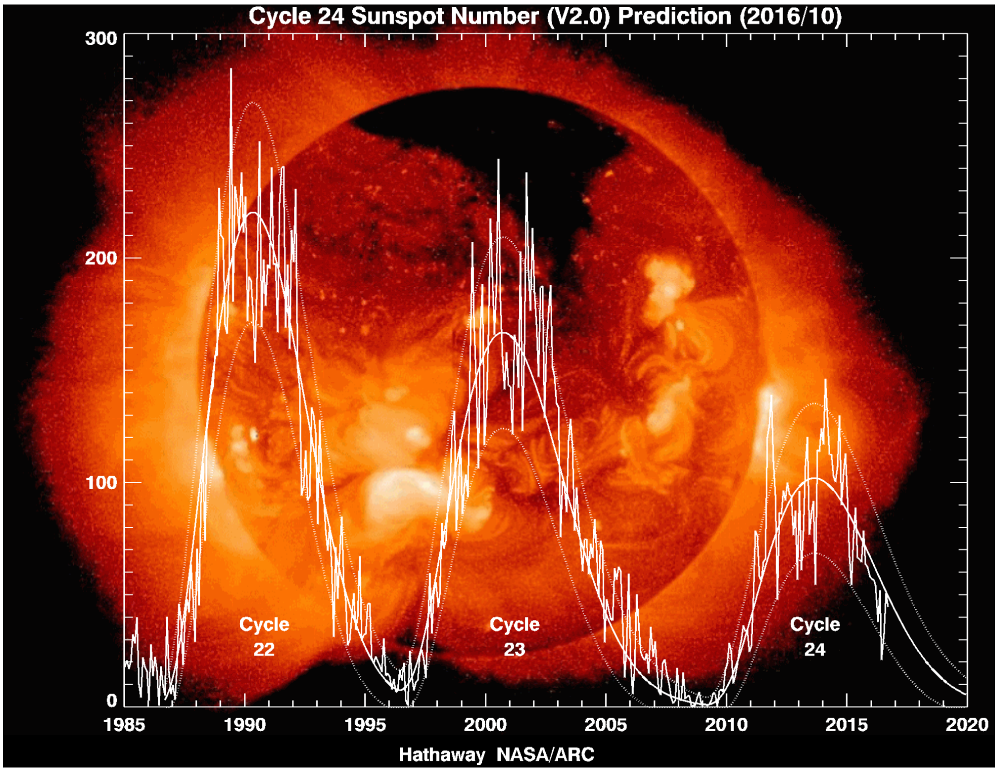

Figure 2.3: Solar activity cycles - Image from NASA

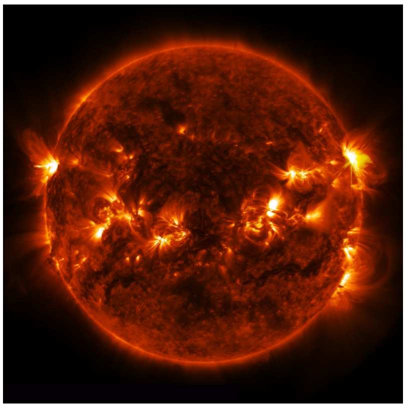

(a) Solar Flare

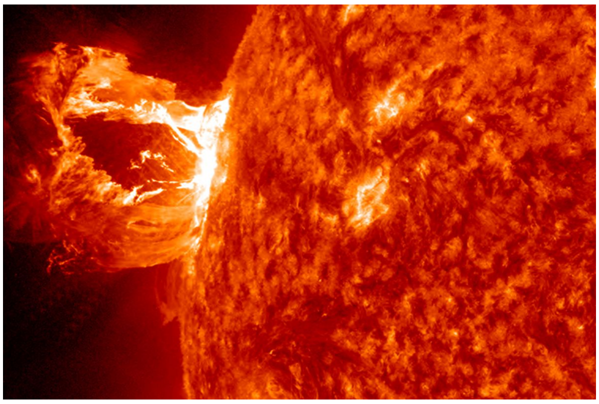

(b) Coronal Mass Ejection

Figure 2.4: Solar Flare and Coronal Mass Ejection - Images from NASA.

The SEP can be simplified into two types, impulsive or gradual. Impulsive events have a shorter duration (less than a day), and display a higher proton content. They are much more frequent than the gradual events, however, due to their limited fluences, they don't constitute a serious radiation hazard. Gradual events, on the other hand, have a longer duration, higher fluxes and are often associated with coronal mass ejections.

While often unpredictable, it is known that SEPs are more likely to occur during a period with higher solar activity, the solar maximum.

These events represent a very high source of danger due to their high unpredictability and very high fluence rates and charged particle energies. However, these particles are deflected by our planet's magnetic field, therefore for low earth orbits (2000 km), where the ISS is located, there are no notable effects.

The average proton flux around the Earth during a solar minimum can be seen in figure 2.5 as a function of proton energy and orbital position.

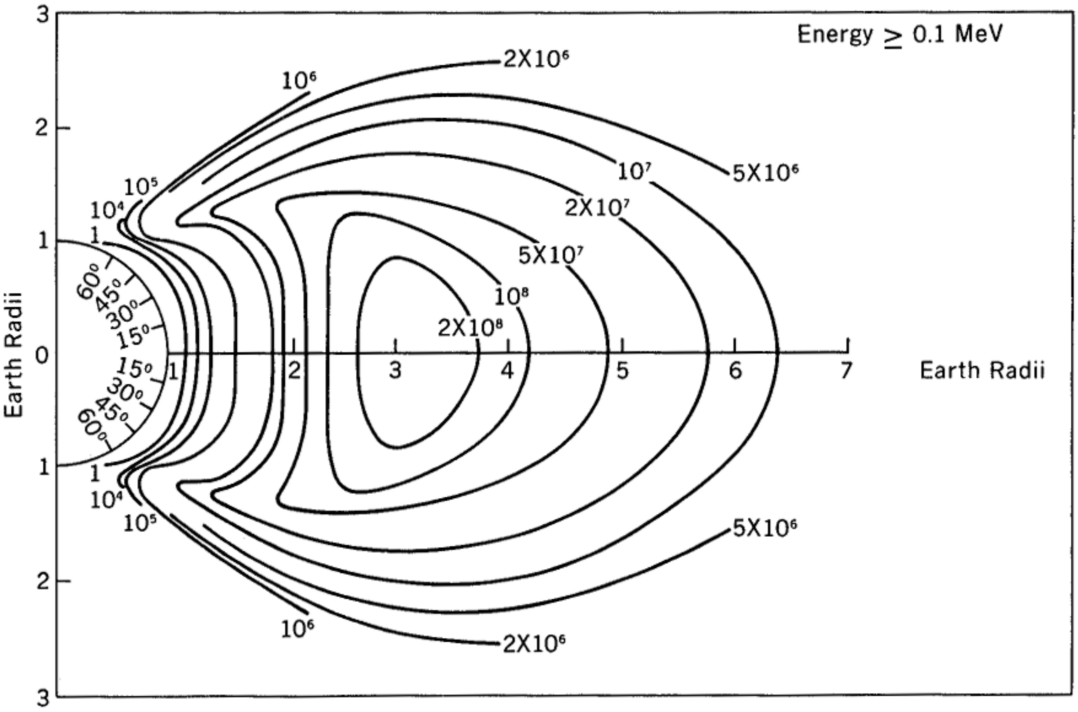

Figure 2.5: Omnidirectional proton flux (protons/cm^{2}s) with energy above 0.1 MeV, during a solar minimum - Image from US National Space Data Center

2.4 Van Allen Radiation Belts (VAB)

For low Earth orbits, where most of manned missions have occurred, the major source of radiation comes from the Van Allen Radiation Belts (VAB).

The VAB, seen in figure 2.6, consists of energetic charged particles held in a torus orbit around the Earth by its magnetosphere. The outer belt is formed by electrons and extends from 15000 km to 25000 km, while the inner belt is composed of both electrons and protons, extending from 1000 km to 6000 km. Most of the particles on the outer belt come from the solar wind and GCR (thus the solar activity has a major influence on the amount of radiation trapped in our magnetosphere), while the particles on the inner belt are mainly comprised from the decay of neutrons resulting from the cosmic ray interactions with our atmosphere.

In the heart of these radiation belts, the radiation dose rate becomes very large and affects electrical components.

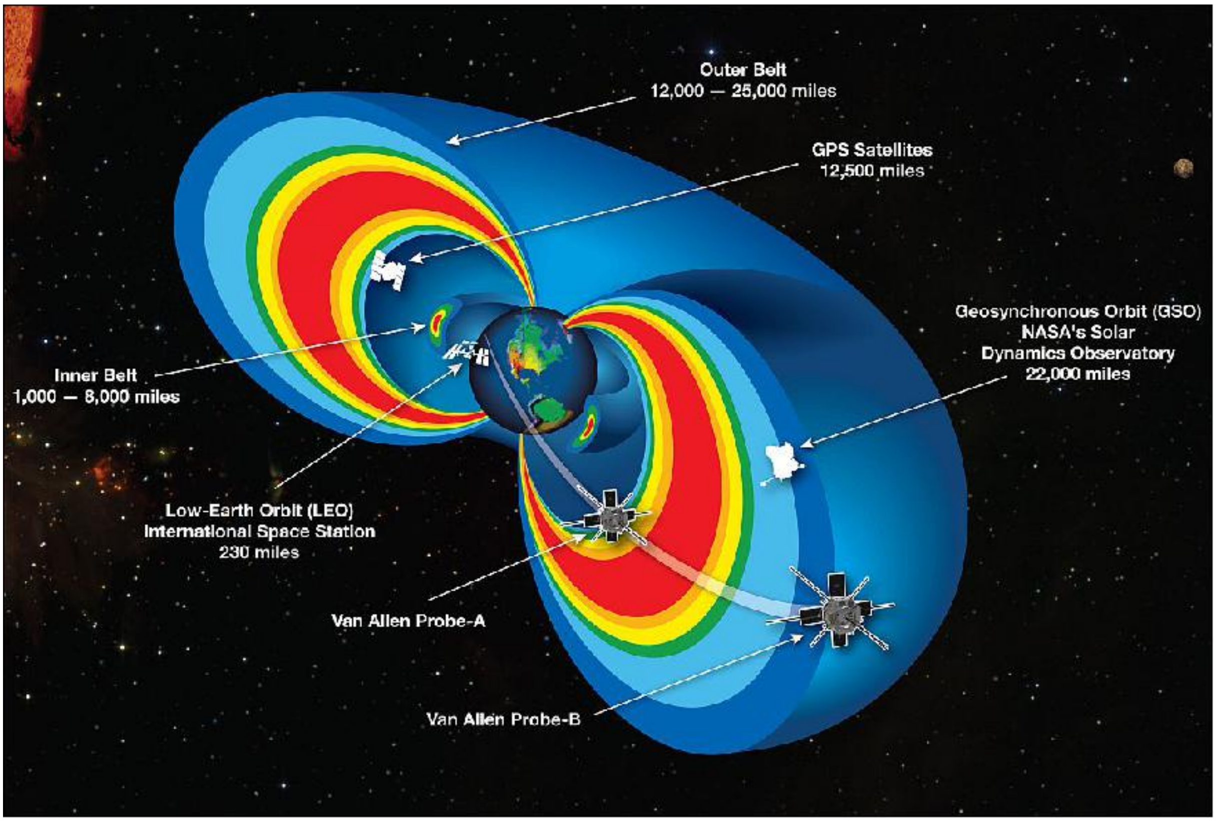

Figure 2.6: A cross section image model of the radiation belts - Image from NASA

2.5 Typical Radiation Doses

Table 2.2 indicates the most common dose rates or values for different shielding scenarios at 1 AU, outside the Earth's magnetic field and typical radiation dose rates for the VAB), while the table from figure 2.7 indicates the typical doses for different types of space missions for longer periods of time and for different shielding thickness.

Source	Component	Unshielded	Spacesuit	Spacecraft
GCR	Positive Ions	2×10^{-5} Sv/hr	2×10^{-5} Sv/hr	2×10^{-5} Sv/hr
Solar Wind	Positive Ions	10^{-7} Sv/hr	0	0
Medium Flare	Positive Ions	1 Sv	0.5 Sv	3×10^{-3} Sv
Maximum Flare	Positive Ions	10^{3} Sv	0.5×10^{2} Sv	3.5 Sv
VAB	Positive Ions Electrons	0.6 Sv/hr 10^{3} Sv/hr	0.3 Sv/hr 0.1 Sv/hr	3×10^{-3} Sv/hr 10^{-2} Sv/hr

Table 2.2: Typical Radiation dose rates and dose values at 1 AU from different sources and typical radiation doses found in the VAB [1].

Where Sv (sievert) is an SI unit for ionizing radiation dose that measures the effects of ionizing radiation on the human body. Applying a factor (1 for gamma rays) an equivalent dose for Gamma rays can be calculated. The order of the maximum radiation dose rate of 100 kRad/h for the external VAB

Shielding [mm Al]	Total ionizing dose [rad]			
	POLAR 7y	ISS 10y	MEO 10y	GEO 15y
0.05	6.11E+06	1.37E+06	4.37E+08	5.01E+08
4	1.14E+04	1.85E+03	7.05E+05	8.38E+04
20	2.65E+03	3.18E+02	5.83E+03	3.34E+03

Figure 2.7: Total ionizing dose levels in Aluminum solid sphere geometries for the reference scenarios, and for shielding values of 4 and 20 mm [10]. The ISS is in the Low Earth Orbit (LEO) while the POLAR is in an irregular elliptic orbit.

and a 100 kRad dose for an average maximum flare are then obtained, which is also of the same order as the average of the TID for a day in Medium Earth Orbit (MEO) or Geostationary Earth Orbit (GEO).

Due to their high energy, the dose rates due to GCR are independent of the shielding provided by the spacecraft or by the spacesuit.

For the geostationary orbits, where the communication satellites are often placed, at around 35 000 km, they're outside the external VAB (figure 2.8), but it also means that they're exposed to the GCR and solar winds and flares. This means that for these satellites, they can be exposed to radiation doses of the order of 10^6 kRad over a period of 15 years.

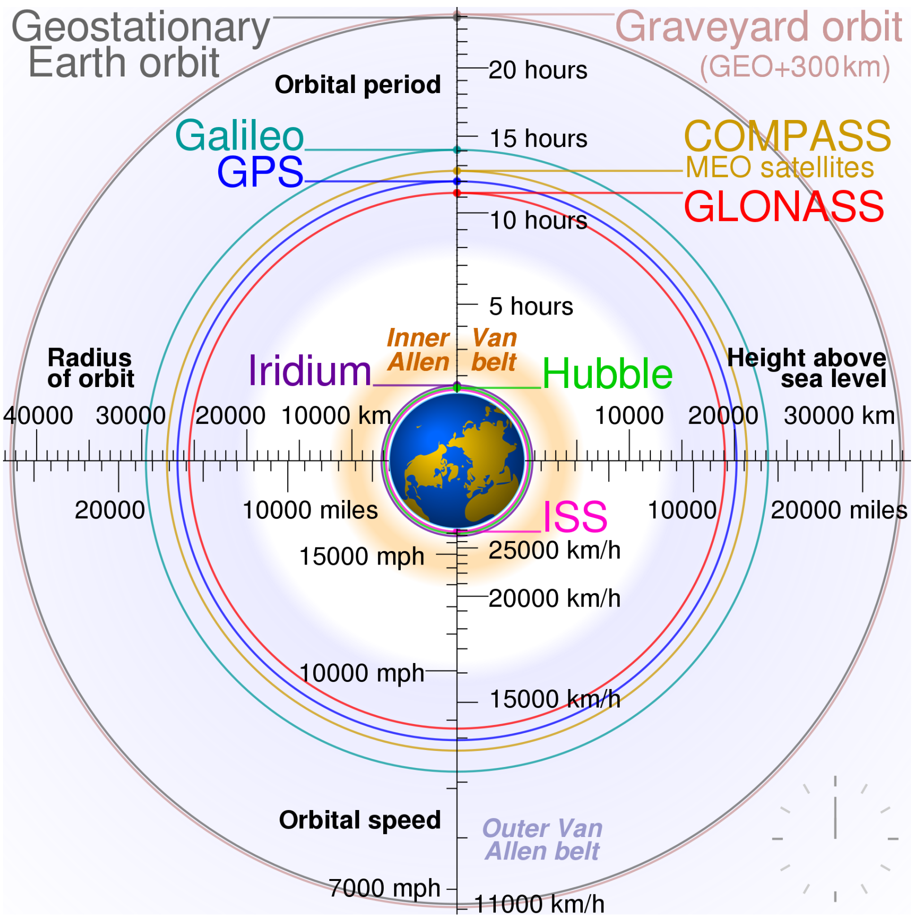

Figure 2.8: Comparison of medium earth orbit satellites with geostationary and graveyard orbits - Image from Wikipedia.

In figure 2.9 we can see a summary of the fluence rate of space radiation in function of its energy.

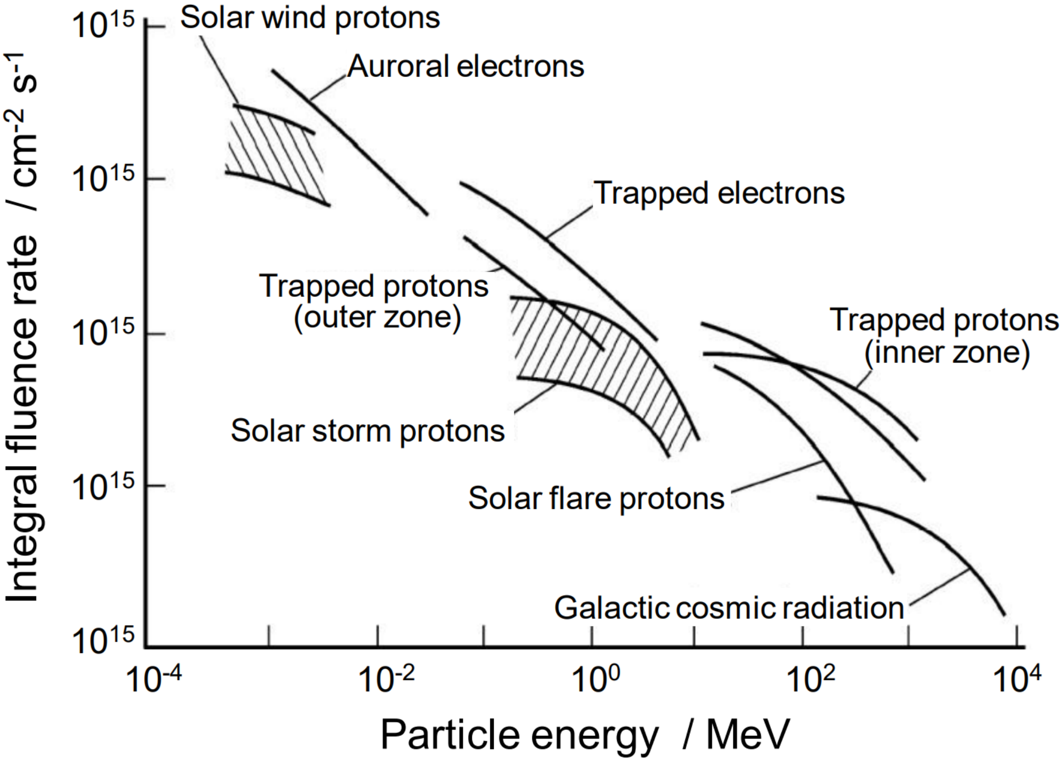

Figure 2.9: Overview of particle fluence rate of space radiation and its energy [9].

Chapter 3

Radiation Effects on Electrical Components

The degradation of EEE, specially semiconductors, due to radiation is a known issue that must be considered since the early stages of any space mission.

The two main classes of damage addressed are the TID and Displacement Damage. In the former, the ionization (production of an electron-hole pair due to radiation) produces trapped charges in the structures or creation of photocurrents, changing the dynamics of the device, while in the latter, the components of the materials are shifted due to scattering (removing an atom from its regular lattice position), producing defects in the material by creating additional carrier traps.

The activated processes and those involved are summarized, for photons and neutrons in table 3.1, for different energies. Charged particles (for example electrons and protons) can interact with target atoms in several ways. They can collide elastically with a nucleus, or experience an inelastic collision with the shell electrons. Electrons can also generate Bremsstrahlung while ions can be captured by a nuclei and trigger a nuclear reaction.

These effects can modify electrical parameters, deteriorate characteristics and leading to the functional failure of those components. Ionizing particles can produce photocurrents in active regions, provoking either a Single Event Effects (SEE) - a change of state caused by an ionizing particle striking a sensitive node, or a measurable current (important for the analysis of the photodiode and CCD's response with the total dose).

Radiation Type	Energy Range	Main Type of Interaction	Primary Effect
Photons	Low	Photoelectric	Ionizing Phenomena
	Medium	Compton	
	High	Pair Production	
Neutrons	Low	Capture and Nuclear Reaction	Displacement Damage
	High	Elastic Scattering	

Table 3.1: Photon and Neutron radiation effects on electrical devices [2, 3].

Although the above effects can be triggered by different particles and can coexist, one of those effects usually predominates for a given material in a given energy range. For this work, neutron, alphas and betas' effects will be disregarded.

3.1 Gamma Radiation interaction with matter

When a high energy particle interacts with matter, part of its energy is consumed in the ionizing process while the other is used in the displacement damage. We can then define the stopping power, S, of a particle as a rate of the energy lost along a path in a material, as the sum of the NIEL (non ionizing energy loss) with the IEL (ionizing energy loss).

Photons can interact in three ways with matter, photoelectric effect, Compton scattering and pair production. Each effect dominates over the others (due to a much higher cross section) at certain energies and atomic number of the absorber material as seen in figures 3.1 and 3.2.

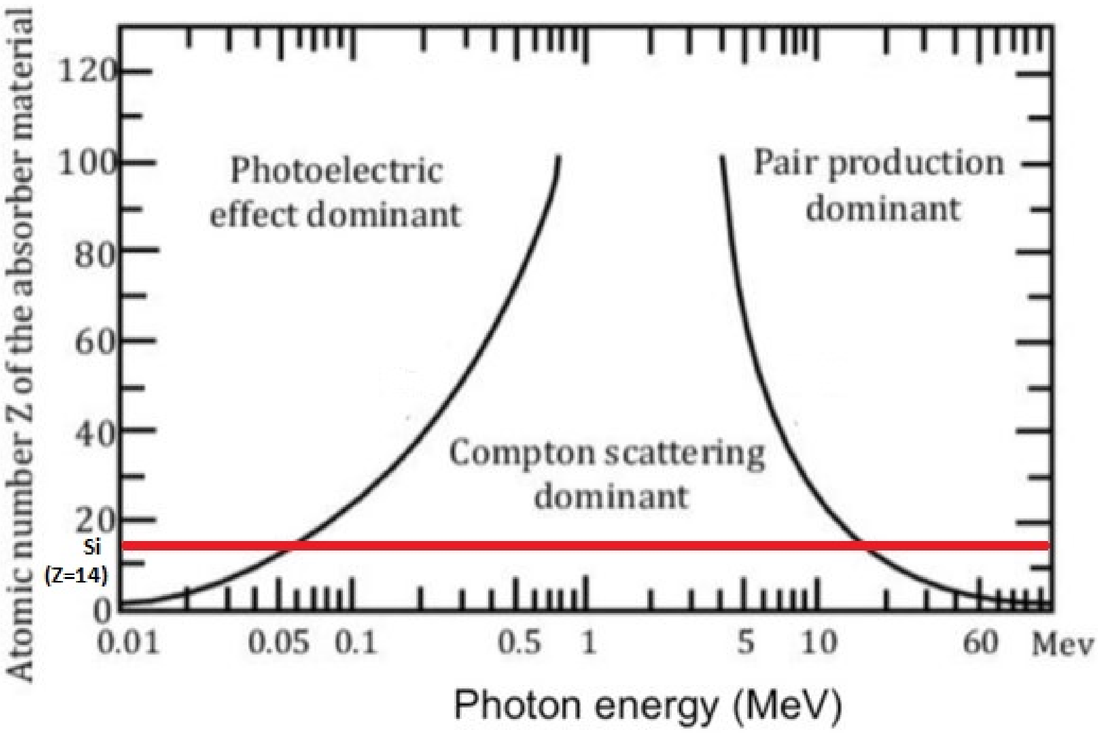

Figure 3.1: Interaction of photons with matter. Silicon's atomic number is 14, where we can see that for that number and for energies around 1 MeV, we have a dominant Compton scattering effect. (Cherry et al., 2012)

At intermediate energies of around 1 MeV, the Compton scattering effect dominates, therefore for this work, this will be the predominant effect.

In this effect, the incoming photon will transfer some of its energy to the electron, resulting in the electron only receiving part of the energy of the photon. The relationship between the angle of the electron scattering, ϕ_e, the energy of the photon, E_γ, and the energy of the electron, E_e, is given in equation 3.1 [18].

$$\frac{E_e\left(E_\gamma + m_e c^2\right)}{E_\gamma\sqrt{E_e\left(2m_e c^2 + E_e\right)}} = \cos\phi_e \tag{3.1}$$

Where m_e is the mass of the electron, c is the speed of light and $m_e c^2$ is approximately 511 keV.

The scattered electron will interact in the material until it deposits its energy or escapes the material. Part of this energy will be used to ionize the material. The total energy deposited by ionization is known as TID.

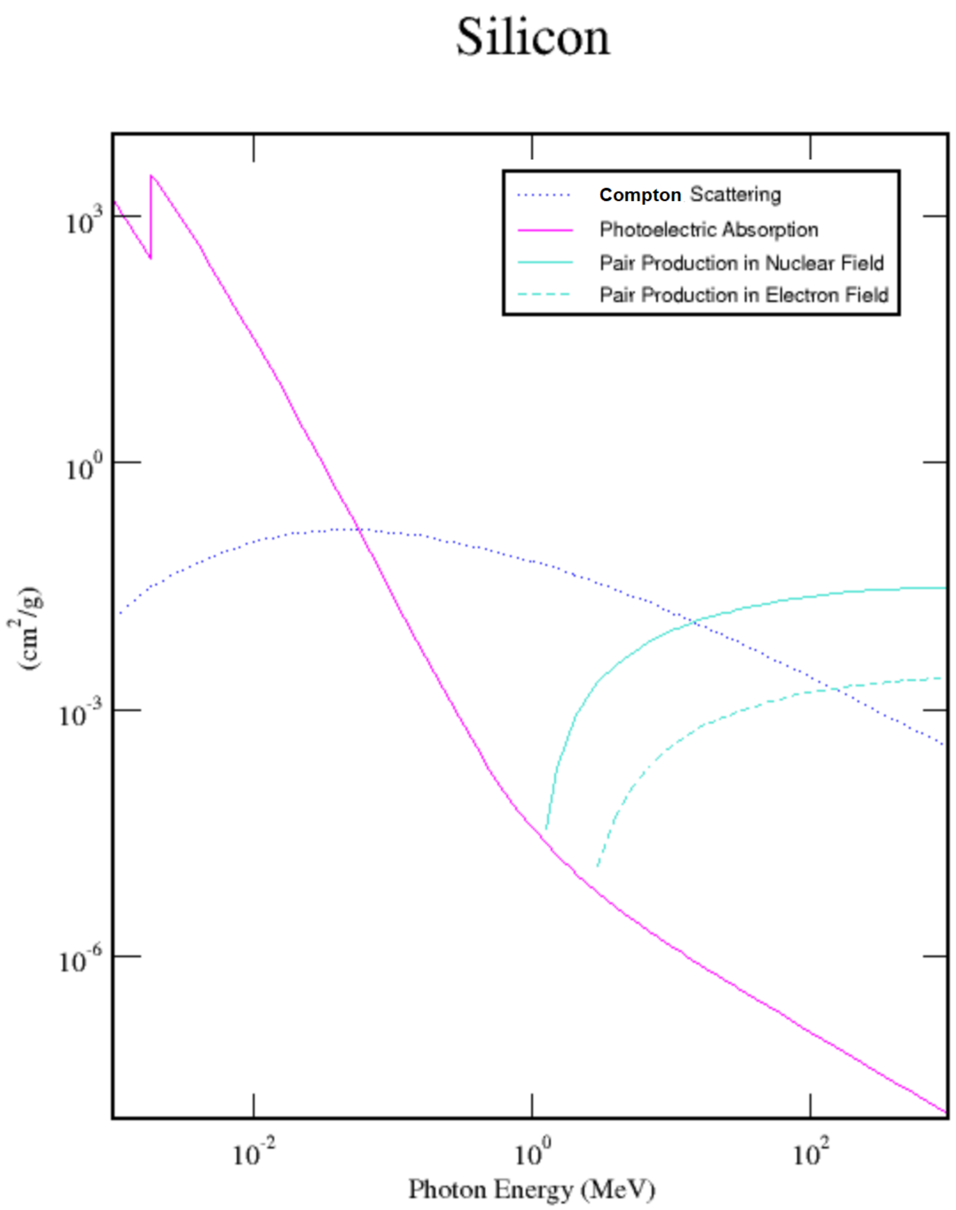

Figure 3.2: Gamma Rays' cross section in Silicon. At 1 MeV we have a dominant Compton scattering effect - Image from XCOM: Photon Cross Sections Database

3.2 TID Effects in Semiconductor Devices

Semiconductor materials are crystalline structures comprised of elements in the 14th group of the periodic table. Semiconductor based detectors present a faster response and smaller dimension than other types of dosimeters.

Firstly - EHP are produced in the intrinsic area and depletion region due to the ionization of electrons, from the valence band of a material to the conduction band. The number of EHP is proportional to the deposited energy of the incident radiation. Secondly, some of the generated EHP recombine rapidly after their generation (order of the picoseconds). The electrons and holes that did not recombine, will be transported in direction of the oxide/semiconductor interface in the presence of an electric field, which can then be measured.

As seen in table 3.2, it requires only 3.6 eV energy to produce an EHP, being very low compared to 35 eV in gas ionization chambers and 1000 eV to generate a photoelectron in a photomultiplier. As such, there's a higher energy resolution. Since the electrons travel fast, there's also a good time resolution.

Material	E_{ion} [eV]	g_0 [ehp · Gy^{-1} · cm^{-3}]
Si	3.6	4×10^{15}
SiO_2	18	8.2×10^{14}

Table 3.2: The ionization energy and ionization-induced generation rate for silicon and silica [2].

To improve their electrical conductivity, their bandgap width can be shortened by addition of impurities known as doping. These impurities can be defined as donors, when they have more valence electrons than the semiconductor material, or acceptors, should they have less. Donors populate the conduction band with electrons, which pushes the Fermi level away from the valence band (n-type), while acceptors contribute with holes, which puts the Fermi level closer to the valence band (p-type). This can be better seen in figure 3.3.

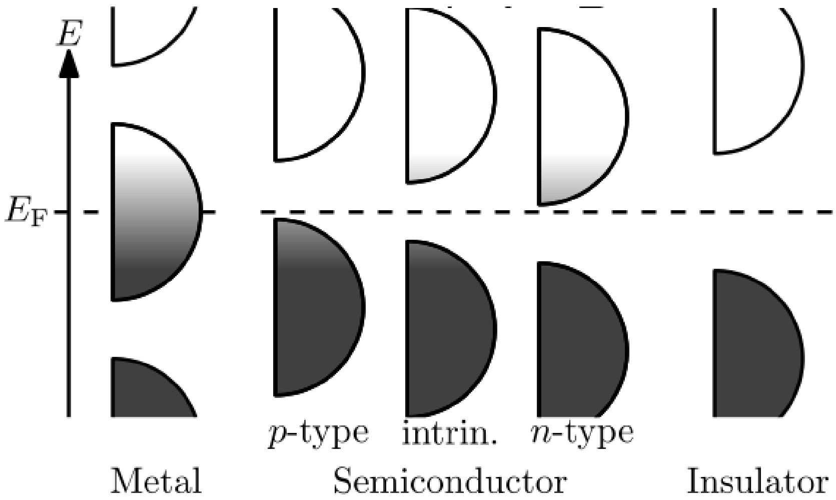

Figure 3.3: Band structure diagrams for several materials - Image from Wikipedia.

Most of the COTS in this work will be semiconductors used as a detector of this type (MOSFET, Photodiode and CCD).

3.2.1 TID Mechanisms in MOS Devices

TID effects represent the damage associated with the accumulated dose of ionizing radiation by a material, so it can be seen as a long-term effect of radiation. It is considered as the main mechanism of cumulative radiation damage in charge-based technologies.

It has more impact on materials like oxide insulators (like SiO_2, which has dielectric properties and is used in MOS technologies), since they have very low concentration of free charges (due to the large gap between the valence and conduction bands) compared to conductors and semi-conductors, making insulators' electrical properties more susceptible to modifications when facing ionizing radiation.

During the transport of the non-recombined holes and electrons, protons are released due to interactions between the holes and hydrogen contained in oxide defects. Some of the holes will be trapped in long-term trapping sites near interface and oxide bulk, leading to the formation of positively trap charges.

These radiation-induced effects cause shifts in the threshold voltages, increase the noise and degradation of devices, due to the buildup of localized potentials. Other parameters affected are the decrease of transconductance, increase of leakage currents and reduction of drain-source breakdown voltage.

However, these effects are temperature dependant, thus it is necessary for temperature stabilisation or an appropriate correction to assure precise measurements.

The threshold voltage shifts depend mainly on the gate SiO_2 thickness. The position of the built-up charges depend on the gate voltage, therefore the smaller the distance between the gate terminal and the charge sheet, the lesser the additional electric field is observed and less the threshold voltage is shifted. Since the distance is greater for the PMOS, because of the negative bias, it is more radiation resistant than the NMOS as we can see in Figure 3.5.

From TID assessment it is possible to infer the amounts of ionizing doses that a device may withstand.

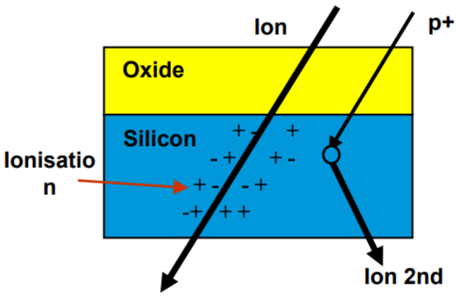

(a) SEP effect on an electronic circuit.

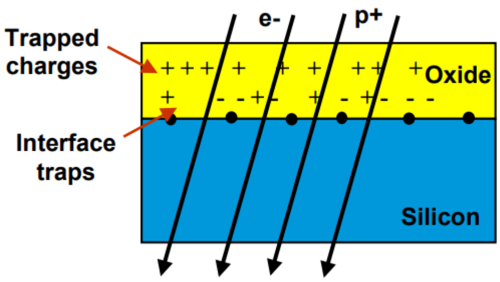

(b) Radiation Effects on Electrical Components.

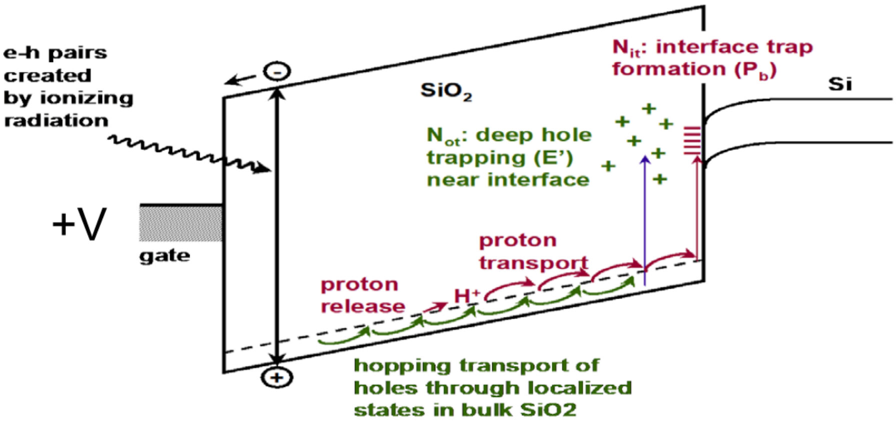

(c) More detailed TID effect on a MOSFET component.

Figure 3.4: TID effect on an electronic circuit - Image from ESA.

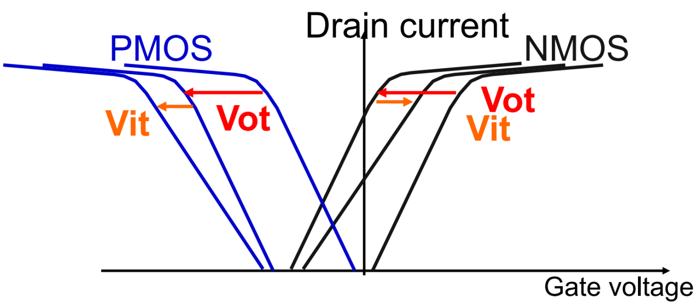

Figure 3.5: Simplified threshold-voltage shifts in MOS transistors: contribution of oxide traps (ot) and interface traps (it) - Image from ESA.

3.2.2 TID Effects on OP-AMPs

An OP-AMP is composed of several different internal components. While some are semiconductors such as internal MOSFETs and diodes, others are not, for example resistors and capacitors.

An ideal OP-AMP is balanced, in other words, its output voltage equals 0 when inverting input voltage equals the non-inverting input voltage. However, real OP-AMPs exhibit an imbalance caused by a mismatch of the input transistors, which results in different bias currents and voltages in the input terminals.

Whenever the OP-AMP is exposed to gamma rays, a disturbance occurs in the input transistors that leads to an increase of their input characteristics. As a result it is expect to see an increase of the difference between the input voltages and current over time, as previously mentioned.

3.2.3 TID Mechanisms in Bipolar Devices

One usual internal component of the OP-AMP are bipolar devices.

Oxide traps form in the same manner as the MOS devices. However, for this component, no voltage is applied to the oxide. Interface traps formed can exchange carriers with the base and increase the base current due to re-combinations. Consequently, the base current increases with no changes in the collector current leading to a gain decrease. The interface traps can also create an inversion layer in the p-doped region which affects both gain and leakage current [19].

Chapter 4

Methods

4.1 EEE Components

The objective of this work is to use COTS EEE components to measure the radiation doses. It is then fundamental to understand the response of the EEE component candidates to radiation. Seven component candidates were irradiated and their response was studied.

The samples were irradiated in a support board, which doubles as an interface board for the measurement of the parameters. A second board carries the reference samples, which were not irradiated.

It was used the software Altium Designer to design the schematics (which can be seen in figures A.1, A.2 and A.3 in the appendix) and PCB of the circuit, which were subsequently sent to EuroCircuits for manufacturing and then manually welded in LIP.

For each type of components, the relevant parameters will be measured and obtained with a Keithley Source Measure Unit (SMU), using a LUA script for automated measurements, with the focus on the understanding differences between the electric parameters before and after Co-60 irradiation. Its measuring accuracy can be seen in figure A.4 in the appendix, for different ranges of current and voltage.

In the following sections the relevant parameters to be measured for each component type are identified. The components will be irradiated and measured at room temperature T_{amb}= 22$\pm$1°C. The list of final components can be seen in table 4.1.

Component Type		Component		N. of units
		Reference	Manufacturer	
A	P-Channel MOSFET	TP2104	Supertex Inc.	4
B	N-Channel MOSFET	2N7000	Supertex Inc.	4
C	Dual Operational Amplifier	LM358	Texas Instruments	5
D	Low-Power Operational Amplifier	MCP6002	Microchip	5
E	Silicon PIN Photodiode	SFH229	Osram	5
F	Silicon PIN Photodiode	OP950	Electronics	5
G	CCD Linear Image Sensor	TCD1304DG	Toshiba	1

Table 4.1: List of components to be tested.

4.1.1 MOSFETs

The detection of radiation for this component is based on the reading of certain parameters such as drain-source current and gate voltage, from which will be plotted an IV curve, which will be compared to the reference results. For the MOSFETs, the circuit will be much simpler, where it's only needed confirm it is in operation mode. The temperatures effects are reduced for a saturated drain-source current, thus the measures will be more focused on the saturation shifts.

A sensitivity of the order of (mV/Gy) is expected, as seen in [20].

It was also chosen two MOSFET, a P-channel (TP2104N3-G) and an N-channel (2N7000-G), where the selection criteria was: through hole mounting style to facilitate the mounting of the MOSFET, and the below 1€ price per unit. It was given preference to the cheapest ones available while trying to choose both a P and an N type.

For the P-channel, the drain-source voltage has to be negative, up to -10V, and the gate-source voltage should be bigger than -3V to guarantee that the saturation current does not pass 0.4A. For the N-channel, the drain-source voltage has to be positive, less than 10V, and the gate-source voltage should be up to 3V, also to guarantee that the saturation current does not pass 0.4A. This is done to minimize the risk of damaging components due to high currents.

Component A

Component A is a P-Channel MOSFET manufactured by Supertex Inc. with the reference TP2104. Our measuring parameter (table 4.2), the drain current, shall be measured by setting the gate-source voltage to a fixed value (-2V, -3V and -4V) and sweeping the drain-source voltage from 0V to -5V in 0.1 increments for the -2V to -5V interval and in 0.05 increments for the 0V to -2V for a better definition of the steep slope. 3 units are to be irradiated while 1 is to be used as a reference.

Characteristics	Symbols	Test Conditions	Limits		
			Min.	Max.	Unit
Drain Current	I_{DS}	V_{DS} = [0, -5] V V_{GS} = {-2, -3, -4} V	-0.4	0	A

Table 4.2: Electrical parameters to be measured for component A.

Component B

Component B is an N-Channel MOSFET manufactured by Supertex Inc. with the reference 2N7000. Our measuring parameter (table 4.3), the drain current, shall be measured similarly to the previous one. By setting the gate-source voltage to a fixed value (2V, 3V and 4V) and sweeping the drain-source voltage from 0V to 5V in 0.1 increments for the 1.5V to 5V interval and in 0.05 increments for the 0V to 1.5V for a better definition of the steep slope. 3 units are to be irradiated while 1 is to be used as a reference.

Characteristics	Symbols	Test Conditions	Limits		
			Min.	Max.	Unit
Drain Current	I_{DS}	V_{DS} = [0, 5] V V_{GS} = {2, 3, 4} V	0	0.4	A

Table 4.3: Electrical parameters to be measured for component B.

4.1.2 OP-AMPs

The offset input current and voltages will be our measuring parameters. For the OP-AMPs it's necessary a voltage follower circuit that can measure the input voltage and the input current. The follower circuit is used to minimize the current draw to it and also to have another reference since on normal operations the gain is 1.

It was chosen two OP-AMPs, LM358PE4 and MCP6002, with the selection criteria: 2-channels, less than 0.50€ per unit and through hole mounting style.

Component C

Component C is a Dual Operational Amplifier manufactured by Texas Instruments with reference LM358. Our measuring parameters (table 4.4), the offset input current and voltage, shall be measured by connecting the positive (CC) and negative power supplies (DD) pins to a +5V and -5V power supply respectively, and connecting both the non-inverting (A) and inverting (B) inputs to a 5V power supply, and connecting the inverting input to the output, while measuring both the current and voltage's evolution with time at the inputs for a period of around 1 min. 4 units are to be irradiated while 1 is to be used as a reference.

Characteristics	Symbols	Test Conditions
Offset Input Current	I	V_A = V_B = 5V V_{CC} = 5V, V_{DD} = -5V
Offset Input Voltage	V	V_A = V_B = 5V V_{CC} = 5V, V_{DD} = -5V

Table 4.4: Electrical parameters to be measured for component C.

The LM OP-AMP is internally composed of 1 power-MOSFET, 2 diodes, 7 resistors, 51 transistors and 2 capacitors.

Component D

Component D is a Low-Power Operational Amplifier manufactured by Microchip with reference MCP6002. Our measuring parameters (table 4.5), the offset input current and voltage, shall be measured exactly the same as the previous component - by connecting the positive (CC) and negative power supplies (DD) pins to a +5V and -5V power supply respectively, and connecting both the non-inverting (A) and inverting (B) inputs to a 5V power supply, and connecting the inverting input to the output, while measuring both the current and voltage's evolution with time at the inputs for a period of around 1 min. 4 units are to be irradiated while 1 is to be used as a reference.

Characteristics	Symbols	Test Conditions
Offset Input Current	I	V_A = V_B = 5V V_{CC} = 5V, V_{DD} = -5V
Offset Input Voltage	V	V_A = V_B = 5V V_{CC} = 5V, V_{DD} = -5V

Table 4.5: Electrical parameters to be measured for component D.

4.1.3 Photodiode

The detection of radiation for this component is based on the reading of the output current, from which will be plotted an IV curve and analysed the saturation currents, which will be compared to the reference results. The "saturation current" for the reverse voltage is known as leakage current. It is expected to observe a shift of those saturation currents.

This component will have to be inserted in a circuit that allows the detection of really low currents, either by amplifying the current, which however also amplifies the noise, or with a very sensitive ammeter that can detect really low currents.

It was chosen two silicon PIN diodes, SFH229 and OP950, where the selection criteria was: nanoAmpere or below dark currents and price per unit below 1€. Afterwards, the remaining options' dark currents were compared, giving preference to the lowest, while trying not to repeat components from the same series.

Component E

Component E is a Silicon PIN Photodiode manufactured by Osram with reference SFH229. Our measuring parameter (table 4.6), the output current, shall be measured by sweeping the voltage of the pins A and B from -2V to 2V, in 0.05 increments, for both a natural lighting and dark environments. 4 units are to be irradiated while 1 is to be used as a reference.

Characteristics	Symbols	Test Conditions
Output Current	I_O	V_{AB} = [-2,2] V

Table 4.6: Electrical parameters to be measured for the unbiased component E.

Component F

Component F is a Silicon PIN Photodiode manufactured by Electronics with reference OP950. Our measuring parameter (table 4.7), the output current, shall be measured by sweeping the voltage of the pins A and B from -2V to 2V, in 0.01 increments in the -1.7V to 1.7V for better definition of the transition region and in 0.05 increments for the rest, for both a natural lighting and dark environments. 4 units are to be irradiated while 1 is to be used as a reference.

Characteristics	Symbols	Test Conditions
Output Current	I_O	V_{AB} = [-2,2] V

Table 4.7: Electrical parameters to be measured for the unbiased component F.

4.1.4 CCD

For the CCD, the measuring parameter will be the output signal (voltage and current output).

This component will have to be connected to a pulse generator in order to be able to generate the master clock, the integration gate and the shift gate.

After an electron is captured in the depletion region, an electric field is used to separate the electron from the hole. After a certain time (collection time), the total number of electrons is measured, which will be used to determine the brightness of that specific pixel. While there's is no electric field present the holes will recombine with the electrons during the time between each image collection.

It was chosen one CCD, TCD1304DG, with the selection criteria: through hole mounting style, and then the one with the lowest cost (which was still fairly expensive at around 20€).

Component G

Component G is a CCD Linear Image Sensor manufactured by Toshiba with reference TCD1304DG. Our measuring parameters (table 4.8), output current and voltage, shall be measured by supplying 5V to the digital and analog power supply pins (DD and AD respectively), grounding the ground pin (SS), connecting the Shift Gate (SH), Integration Clear Gate (ICG) and Master Clock (ϕM) to a pulse generator to their respective pulses as seen in the pulse characteristics table (4.9), while measuring both current and voltage's evolution with time for around 20 seconds, for three different conditions: dark, environment light and dark after light exposure ("dark 2"). Since there's only 1 unit available, there's no reference sample.

Characteristics	Symbols	Test Conditions
Output Current	I_O	V_{AD} = V_{DD} = 5 V , V_{SS} = 0 V
Output Voltage	V_O	SH (0.8MHz pulse), ICG (0.4MHz pulse), ϕM (0.8MHz clock)

Table 4.8: Electrical parameters to be measured for component G.

SH (Shift Gate)	0.8MHz Burst, Delay 100ns, High 1.5V, Low 0V, Width 1μs
ICG (Integration Clear Gate)	0.4MHz Burst, Delay 0ns, Ampl. 1.5 V_{pp}, Offset -750mV, Width 2.1μs
ϕM (Master Clock)	0.8Mhz

Table 4.9: Pulse Generator's pulse characteristics

The minimum recommended frequency at which this CCD works is 0.8 MHz. Since our measuring equipment does not have a MHz sample rate (3.333 kHz maximum) it is not possible to measure the pixels individually but rather to average the pixels over time.

Therefore, it will be measured the output current and the average pixel output voltage over time.

4.1.5 Final Board

Adding all the above components into the board and creating the tracks in a 2 layered board we get the 3D final model and the post-manufacturing board in figure 4.1. The total expenses of the components were below 35€.

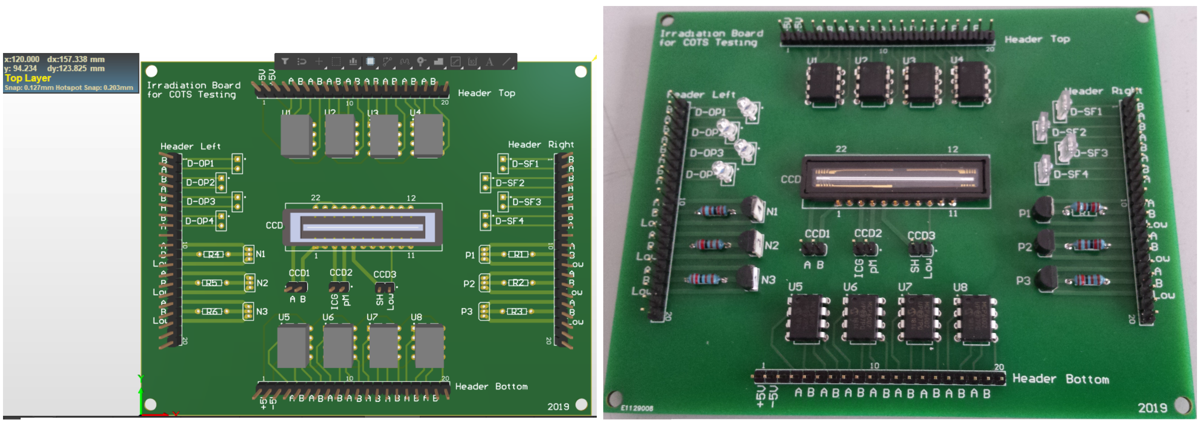

Figure 4.1: 3D and final board, after manufacturing and welding the components, with 12cm x 9.4cm.

4.2 Radiation Tests

All components were to be irradiated without a bias condition and its measuring parameters to be measured prior to the irradiation, in between radiation steps and after the end of the irradiations.

Due to time constraints of the irradiation site it's not possible to measure all the interesting electrical parameters, so only the main parameters referred in last section will be focused upon for each component.

4.2.1 Test Plan

Radiation Test Facility

The Co-60 tests were performed in a Portuguese facility, IRIS ("Instalação de Radiação Ionizante") located in CTN-IST (Campus Tecnológico e Nuclear – Instituto Superior Técnico) with appropriate quality control and accurate standard dosimetry, using an ionisation chamber with a 5% or better precision, respecting the ECSS-22900. It was used the PRECISA-22 irradiation machine, which can be seen in figure 4.2.

The Cobalt sources, contained in cylinders and deployed by the irradiation machine, were positioned sideways and considered to be isotropic point-like sources. Due to their position, there is a dependency with the distance to the source. In order to minimize this effect, and to achieve a better uniformity, the sample support should rotate inside during the irradiation.

Pre-Irradiation Tests

A pre-irradiation test phase was foreseen in the present plan. The aim of this phase was to prepare the readout system and to acquire the reference data for the components for later comparison with the data to be acquired during the irradiation.

Co60 Irradiation

The components were irradiated using a Cobalt-60 radioactive source up to a Level of Interest dose of 100 kRad, with an approximate 90 kRad/hour dose rate, which is around the 100 kRad/hour dose rates of the VAB for an unshielded target.

Figure 4.2: Irradiation Machine PRECISA-22, front view and inside view.

The Co-60 is a preferred source for TID qualification of EEE components for space use, due to being empirically demonstrated that for the same dose, they're affected in a more pronounced manner when compared to other radiation sources [21]. It is the component qualification standard for radiation environment in terrestrial orbits. Thus, it is considered as a worst-case TID test condition for components exposed to space radiation environment.

The samples were irradiated in the carrier board. There were two types of carrier boards, one for irradiation and one for reference. The irradiation board contained all samples but one of a component type to be irradiated in a specific condition, while the reference board contained one sample of each component (except for the CCD), to compare with the irradiated board and to verify any external factors' influence (temperature for example).

The carrier board allowed two modes of operation: Measurement and irradiation. In the irradiation mode the sample board, which had no bias and was completely independent, was inserted inside the machine. In the measurement mode the carrier boards are coupled to the measuring system so that the measurements could be done accordingly.

The reference board was measured, for each step, during the irradiation of the main board to find if any variations or fluctuations of the parameters were dependant on external factors.

Specification of number of exposures, doses and dose rates, and duration of each exposure

In table 4.10 we can see the foreseen irradiation test sequence.

Irradiation Step	0	1	2	3	4	5
Total Dose (kRad)	0	5	10	25	50	100
Exposure Time Total	0	3m20s	6m40s	16m40s	33m20s	66m40s
Exposure Time Partial	0	3m20s	3m20s	10m00s	16m40s	33m20s

Table 4.10: Planned Irradiation Test Sequence

The total doses for each step were chosen this way to try to find a correlation between the measured parameters and the lower doses, while still trying to verify if or when the component stops reacting for higher doses, and trying to reach the 100 kRad target dose, keeping in mind the limited time available at the irradiation facility.

4.3 Dosimetry

Dosimetry tests were made before the irradiation of the components, where it was used a 12 cm diameter and 1 cm high cylinder as a test board.

Using an ionization chamber FC65-P, and it was measured the dose rate on both planes of the cylinder (base and top) from the center to the edge while rotating.

It was also studied the shadow effects with a test board. A 5% effect on a component 2 cm higher than a nearby component was found. Since in the real board the components are approximately the same height, this effect was disregarded.

The average dose rates are seen in table 4.11, where the statistical measurement error was 2.2%.

Cylinder Radius (cm)	0.0	1.0	2.0	3.0	4.0	5.0
Dose Rate (kRad/h)	88.62	89.76	91.44	94.02	96.90	100.8

Table 4.11: Average dose rate in the top plane of the cylinder.

We can then verify that the effective dose rate is dependent on the radial position of the sample by plotting the dose measured in each radius to an inverse square function $D = a \cdot (x + c)^{-2} + b$ (figure 4.3), where we get the following results in table 4.12.

a	b	c	χ^2/dof
(1.7 $\pm$ 0.5) $\cdot 10^3$	(7.978 $\pm$ 0.127) $\cdot 10^1$	(-1.4 $\pm$ 0.1) $\cdot 10^1$	0.03061

Table 4.12: Fitting parameters for an inverse square function, using the least-squares method.

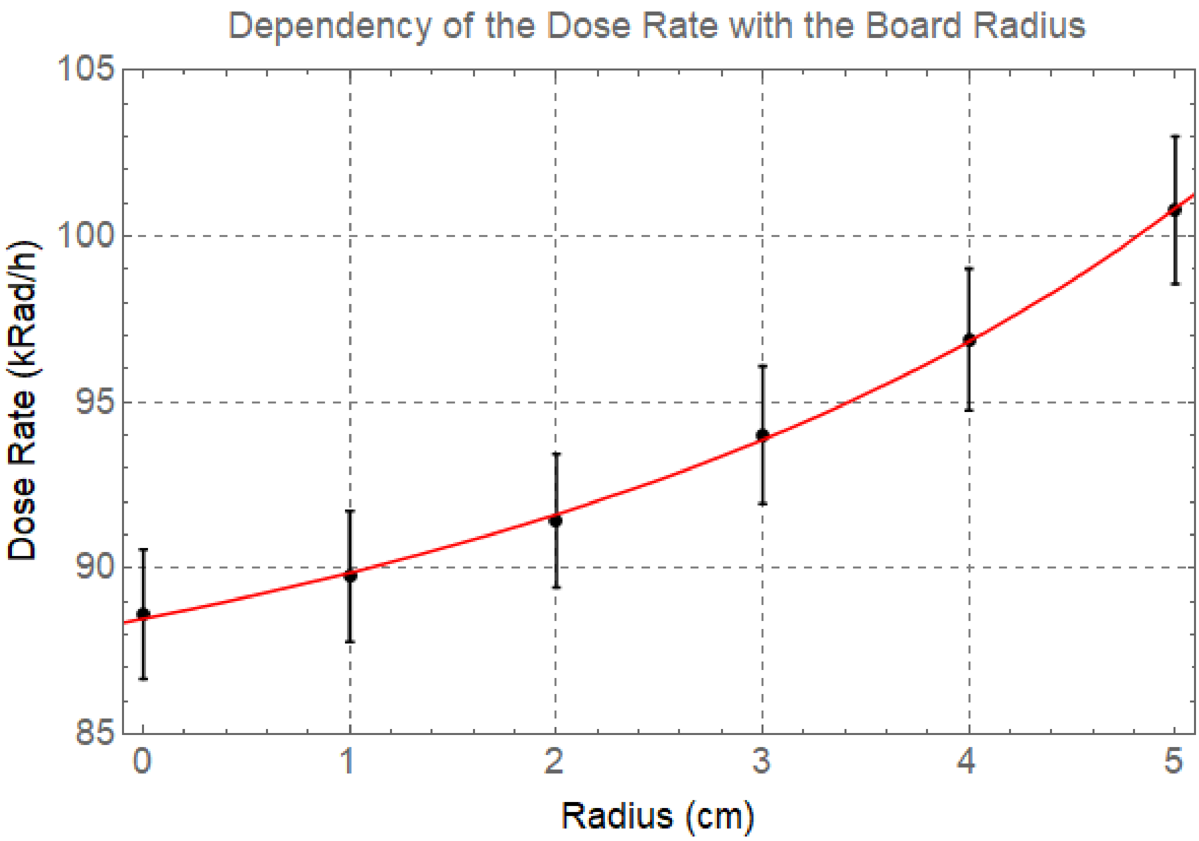

Figure 4.3: Fitting the dose dependency with the radius for a function of the type $D = a \cdot (x + c)^{-2} + b$. The parameters for the fit are seen in table 4.12. As a reminder, the board had 12 cm of length and 9.4 cm of width.

The resulting χ^2 is very likely due to the overestimation of the errors, since by observing the figure it is visible that the resulting fit is adjusted to the data points.

Also, it is to be noted that the Co-60 source was not in the same plane as the board but slightly above.

In this work, the target doses represent minimum values to be achieved. As such, it was taken as reference the lowest dose rate (at the center) to calculate the exposure time. Consequently, the total dose at the periphery was higher than the desired one.

The irradiation test sequence can be seen in table 4.13.

Measuring the components' average distance to the center, we can assign a radius to the correspondent component. The CCD is at 0 cm, the OP-AMPs are at 3 cm and the photodiodes and MOSFETs are at the 4 cm radius. In table 4.14 it's summarized the irradiation test sequence used.

Partial Dose (kRad)	Exposure Time Partial	Cylinder Radius (cm) 0	1	2	3	4	5
	3m27s	5.09	5.16	5.25	5.40	5.57	5.79
	3m27s	5.09	5.16	5.25	5.40	5.57	5.79
	10m21s	15.28	15.48	15.76	16.21	16.70	17.38
	17m14s	25.47	25.79	26.27	27.01	27.84	28.97
	34m29s	50.95	51.59	52.54	54.02	55.68	57.94
Total	68m58s	101.89	103.18	105.07	108.05	111.36	115.89

Table 4.13: Irradiation Test Sequence

Total Dose (kRad)	Exposure Time Total	Component CCD	OP-AMP	MOSFET/Photodiode
	3m27s	5.09	5.40	5.57
	6m54s	10.18	10.80	11.14
	17m15s	25.46	27.01	27.84
	34m29s	50.93	54.02	55.78
	68m58s	101.89	108.05	111.36

Table 4.14: Irradiation Test Sequence for each type of component.

Chapter 5

Results

In this work, the degradation with radiation of seven different types of COTS was studied. In this section, the evolution of the measured parameters with the level of irradiation is presented.

5.1 P-Channel MOSFET (TP2104)

For each sample of the P-Channel MOSFET, the drain current was measured while sweeping the drain-source voltage, V_{DS}, in order to establish the saturation drain current, I_D, obtained by a weighted average of the data points of the interval -4V to -5V. These measurements were made for each irradiation step, for different source-gate voltage, V_{GS}, conditions. The I-V curves can be found in the appendix (A). For each irradiation step the result was obtained through a weighted average of the results of the different irradiated samples. These results from the 6 irradiation steps were aggregated, after checking its consistency, with the reference sample plotted for comparison.

In figure 5.1 it is shown the evolution of the saturation current with the irradiation level for V_{GS} equal to 2, 3 and 4 Volts, respectively.

The reference presents no notable fluctuations. From the appendix I-V curves from the reference, there seems to exist a correlation between a higher V_{GS} and a higher fluctuation due to external parameters.

The data presents an evolution more pronounced for lower dose levels and a higher saturation effect at higher dose levels.

This evolution was modeled using an exponential of the type $I_D = -k\, e^{m \cdot x} + o$, fitted to the data using the least-squares method. The obtained results can be seen in table 5.1.

From those results, it can be concluded that this component can be used as a dosimeter.

While it has the better χ^2, there is a faster saturation with the dose for the 2V V_{GS}, which limits its use to lower doses. While the other two do not present the same problem, it is necessary to increase the gate-source voltage in order to be able to measure a saturation current for a higher dose, which in turn, increases the susceptibility to external factors and the measurement errors.

V_{GS}	k	m	o	χ^2/dof
2V	(3.02 $\pm$ 0.03) $\cdot 10^{-2}$	(-8.689 $\pm$ 0.193) $\cdot 10^{-2}$	(1.71 $\pm$ 1.68) $\cdot 10^{-4}$	1.10
3V	(1.22 $\pm$ 0.03) $\cdot 10^{-1}$	(-2.719 $\pm$ 0.195) $\cdot 10^{-2}$	(-1.84 $\pm$ 0.18) $\cdot 10^{-2}$	3.23
4V	(1.59 $\pm$ 0.02) $\cdot 10^{-1}$	(-2.197 $\pm$ 0.084) $\cdot 10^{-2}$	(-1.23 $\pm$ 0.02) $\cdot 10^{-1}$	0.291

Table 5.1: Fitting parameters for $I_D = -k\, e^{m \cdot x} + o$, using the least-squares method.

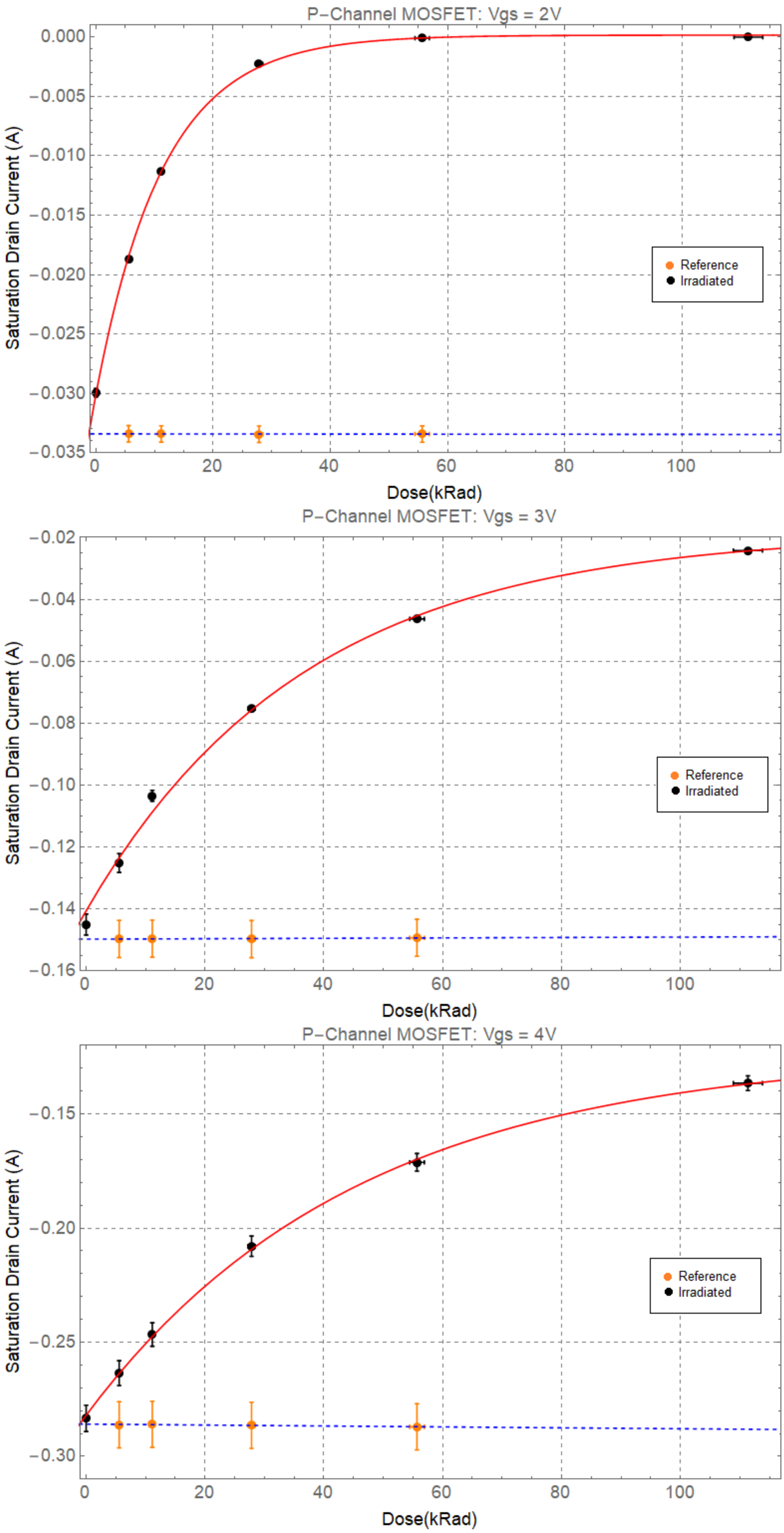

Figure 5.1: P-Channel MOSFET's saturation current vs dose and reference values.

5.2 N-Channel MOSFET (2N7000)

For each sample of the N-Channel MOSFET, the drain current was measured while sweeping the drain-source voltage, V_{DS}, in order to establish the saturation drain current, I_D. For the 2V V_{GS}, it obtained by a weighted average of the data points of the interval 3V to 4V. For the other voltages, it was not possible to obtain a saturation current for all steps due to the 0.4A equipment limit, therefore a point at V_{DS} = 2V was selected for the V_{GS} = 3V and a point at V_{DS} = 1.8V was selected for the V_{GS} = 4V.

These measurements were made for each irradiation step, for different source-gate voltage, V_{GS}, conditions. The I-V curves can be found in the appendix (A). For each irradiation step the result was obtained through a weighted average of the results of the different irradiated samples. These results from the 6 irradiation steps were aggregated, after checking its consistency, with the reference sample plotted for comparison.

In figure 5.3 it is shown the evolution of the saturation current with the irradiation level for V_{GS} equal to 2 and 3 Volts, respectively.

The reference presents no notable fluctuations. As before, there also seems to exist a correlation between a higher gate-source voltage and a higher fluctuation due to external parameters.

The results from the 4V V_{GS} can then be discarded due to the fact that as seen in figure 5.2, the I-V curves for the 6 steps all saturate at the equipment limit of 0.4A and their values at the 1.8V V_{DS} do not seem to present any meaningful correlation.

The data presents an evolution more pronounced for lower dose levels and a higher ”saturation” effect at higher dose levels due to the 0.4A current limit.

This evolution was modeled using an exponential of the type $I_D = -k\, e^{m \cdot x} + o$, fitted to the data using the least-squares method. The obtained results can be seen in table 5.2. The results for the 4V V_{GS} can be seen in the appendix in figure A.9 and table A.1.

From those results, it can be concluded that this component can be used as a dosimeter for low V_{GS}. For higher voltages, it could be possible to use as a dosimeter by adding a resistor in order to decrease the currents to lower values that do not damage the components and to be able to observe the saturation currents.

There is a faster saturation with the dose for the V_{GS} higher than 2V, which limits its use to lower doses for higher V_{GS}. Contrary to the previous P-Channel, by decreasing the V_{GS}, we can measure with higher accuracy, decreasing the susceptibility to external factors and avoiding component damage.

V_{GS}	k	m	o	χ^2/dof
2V	$(4.22 \pm 0.82) \cdot 10^{-1}$	$(-7.971 \pm 1.931) \cdot 10^{-3}$	$(4.40 \pm 0.82) \cdot 10^{-1}$	5.22
3V	$(1.79 \pm 0.05) \cdot 10^{-1}$	$(-3.595 \pm 0.271) \cdot 10^{-2}$	$(3.76 \pm 0.05) \cdot 10^{-1}$	1.03

Table 5.2: Fitting parameters for $I_D = -k\, e^{m \cdot x} + o$, using the least-squares method.

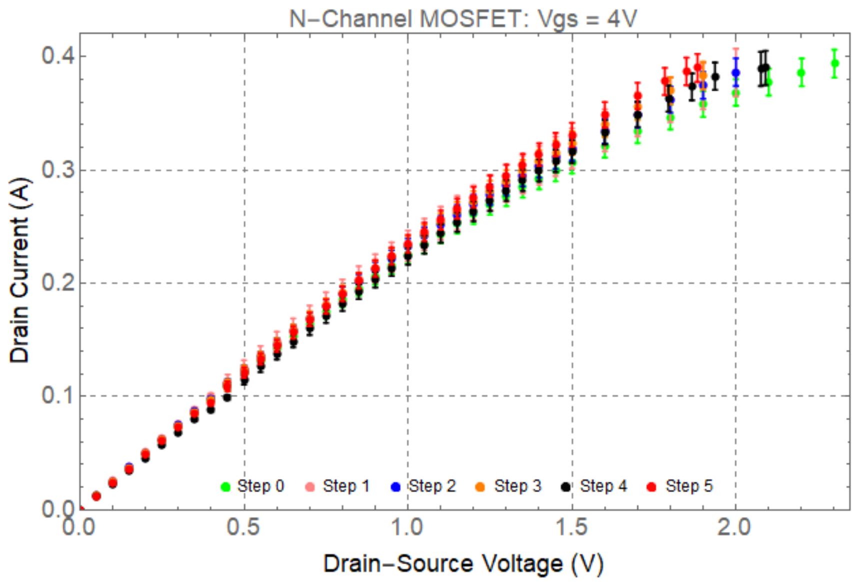

Figure 5.2: N-Channel MOSFET for Vgs equal 4V for the 5 irradiation steps.

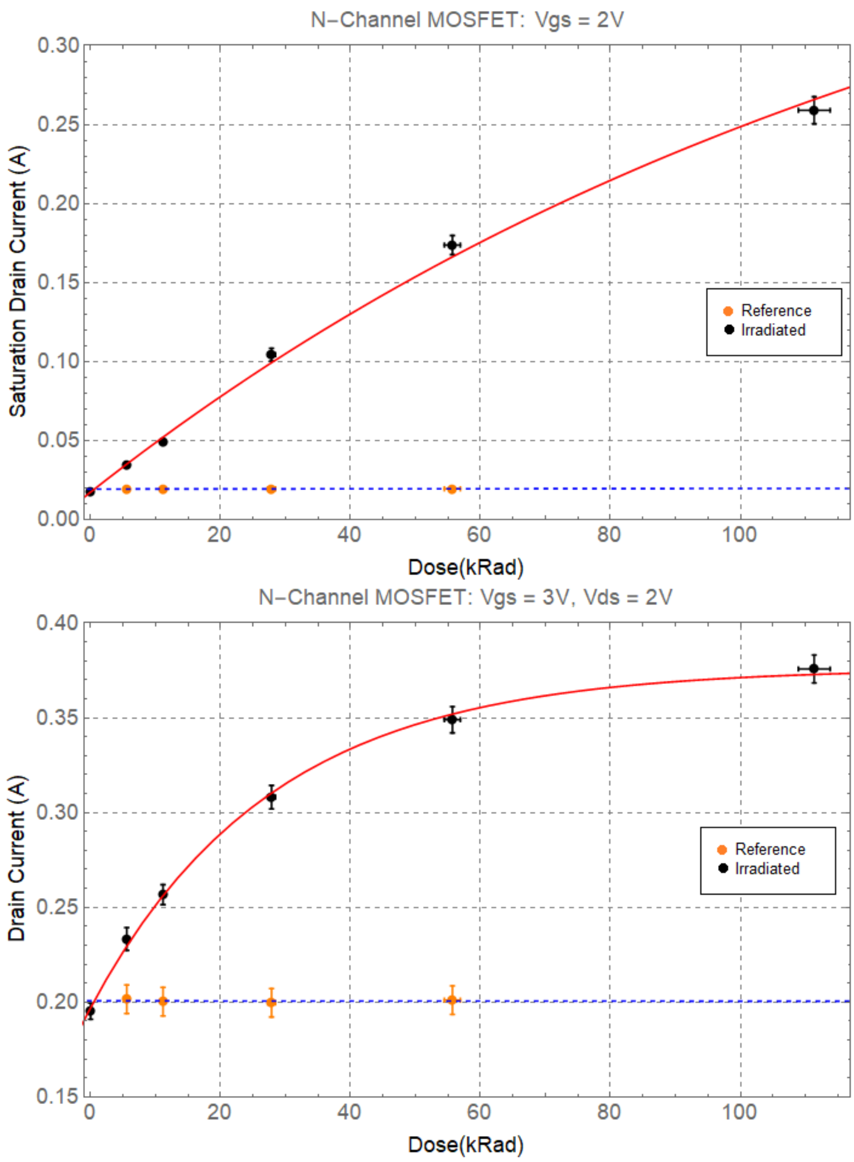

Figure 5.3: N-Channel MOSFET's saturation current vs dose and reference values.

5.3 Dual Operational Amplifier (LM358)

For each sample of the LM358, it was measured the voltage and current of the inputs of the component, for around one minute, in order to obtain the offset between both inputs for each electrical characteristic.

These measurements were made for each irradiation step. The parameters' variation with time can be found in the appendix (A). For each irradiation step the result was obtained through a weighted average of the results of the different irradiated samples, averaged over time. These results from the 6 irradiation steps were aggregated, after checking its consistency, with the reference sample plotted for comparison.

In figures 5.4 and 5.5 it is shown the evolution of the offset input current and voltage, respectively, with the irradiation level.

Observing the previous figures, we can verify the importance of the reference sample, since it is very similar to the measured results. We can then conclude that this variation of offset input current and voltage is not dependant on the dose but rather on the external factors, and that they're merely fluctuations.

From those results, it can be concluded that this component cannot be used as a dosimeter under this conditions for these electrical characteristics and setup.

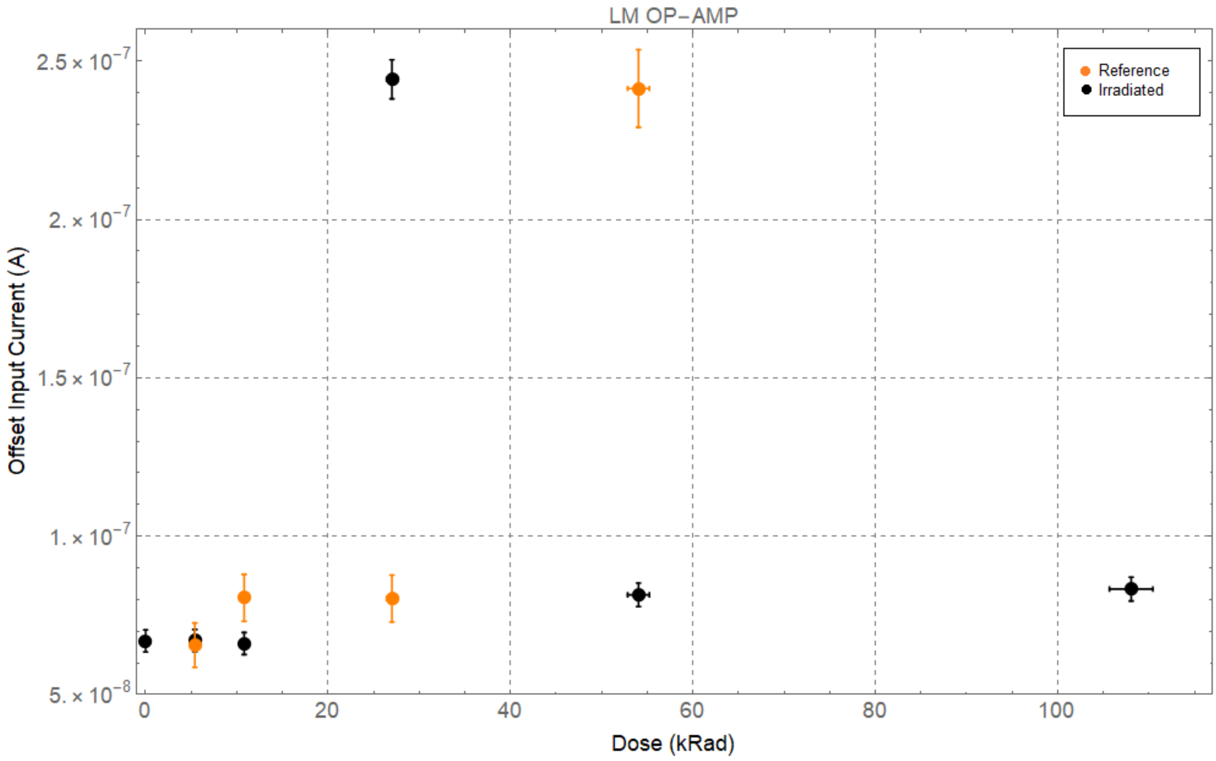

Figure 5.4: LM OP-AMP average offset input current vs dose plot and reference values.

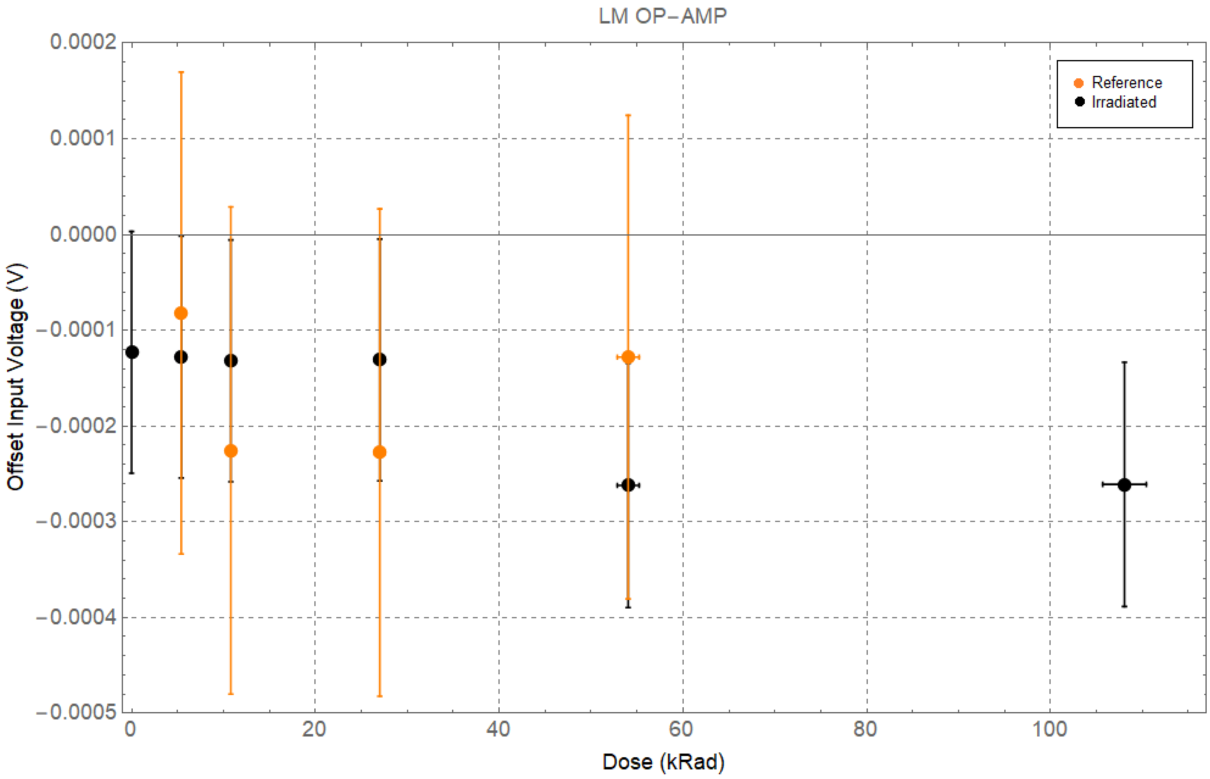

Figure 5.5: LM OP-AMP average offset input voltage vs dose plot and reference values.

5.4 Low-Power Operational Amplifier (MCP6002)

For each sample of the MCP6002, it was measured the voltage and current of the inputs of the component, for around one minute, in order to obtain the offset between both inputs for each electrical characteristic.

These measurements were made for each irradiation step. The parameters' variation with time can be found in the appendix (A). For each irradiation step the result was obtained through a weighted average of the results of the different irradiated samples, averaged over time. These results from the 6 irradiation steps were aggregated, after checking its consistency, with the reference sample plotted for comparison.

In figure 5.6 it is shown the evolution of the offset input current and voltage, respectively, with the irradiation level.

Just like the previous component, by observing the previous figures, the results of the reference sample are similar to the measured results, being of the same order of the fluctuations. We can then conclude that this variation of offset input current and voltage is not dependant on the dose but rather on the external factors, and that they're merely fluctuations.

From those results, it can be concluded that this component also cannot be used as a dosimeter under this conditions for these electrical characteristics and setup.

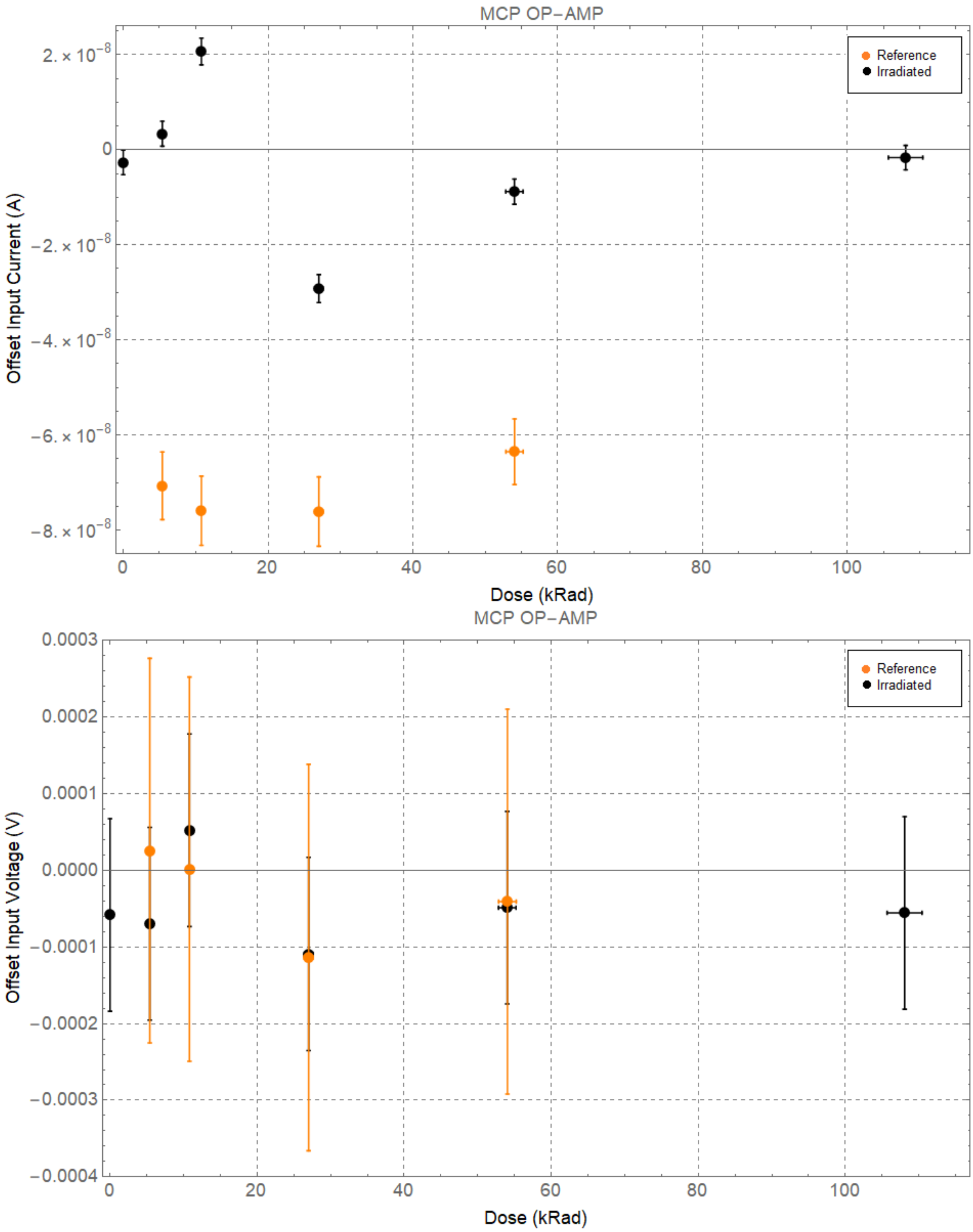

Figure 5.6: MCP OP-AMP average offset input current and voltage vs dose plot and respective reference values.

5.5 Silicon PIN Photodiode (SFH229)

For each sample of the SFH229 Photodiode, the current was measured while sweeping the voltage in order to establish the saturation currents. These measurements were made for each irradiation step, for different light conditions ("Light" in the presence of artificial room light and "Dark" where the component was covered). The I-V curves can be found in the appendix (A). For each irradiation step the result was obtained through a weighted average of the results of the different irradiated samples. These results from the 6 irradiation steps were aggregated, after checking its consistency, with the reference sample plotted for comparison.

This component presents no notable results except for the left saturation current (leakage current) for the light case (figure 5.7), which was obtained by a weighted average of the data points of the interval -1.5V to -2V. However, by comparing it with the reference, the apparent variation is of the same order as the fluctuations (except for the last step). While it can be seen a similar effect in the left saturation current for the dark case, it is of the order of the dark current (10^{-11} to 10^{-10} A).

Thus, the SF photodiode's saturation currents seem to be independent of the dose. As discussed previously in section 1.2, we can confirm that for 60 kRad there doesn't seem to be any significant effect on the saturation current.

From those results, it can be concluded that this component cannot be used as a dosimeter, at least for these doses. For its utility as a high dose dosimeter more tests with a higher dose should be performed.

While the irradiation machine did not allow it, it could be interesting to evaluate the measures with the component biased in order to collect the semiconductor generated charge during the irradiation.

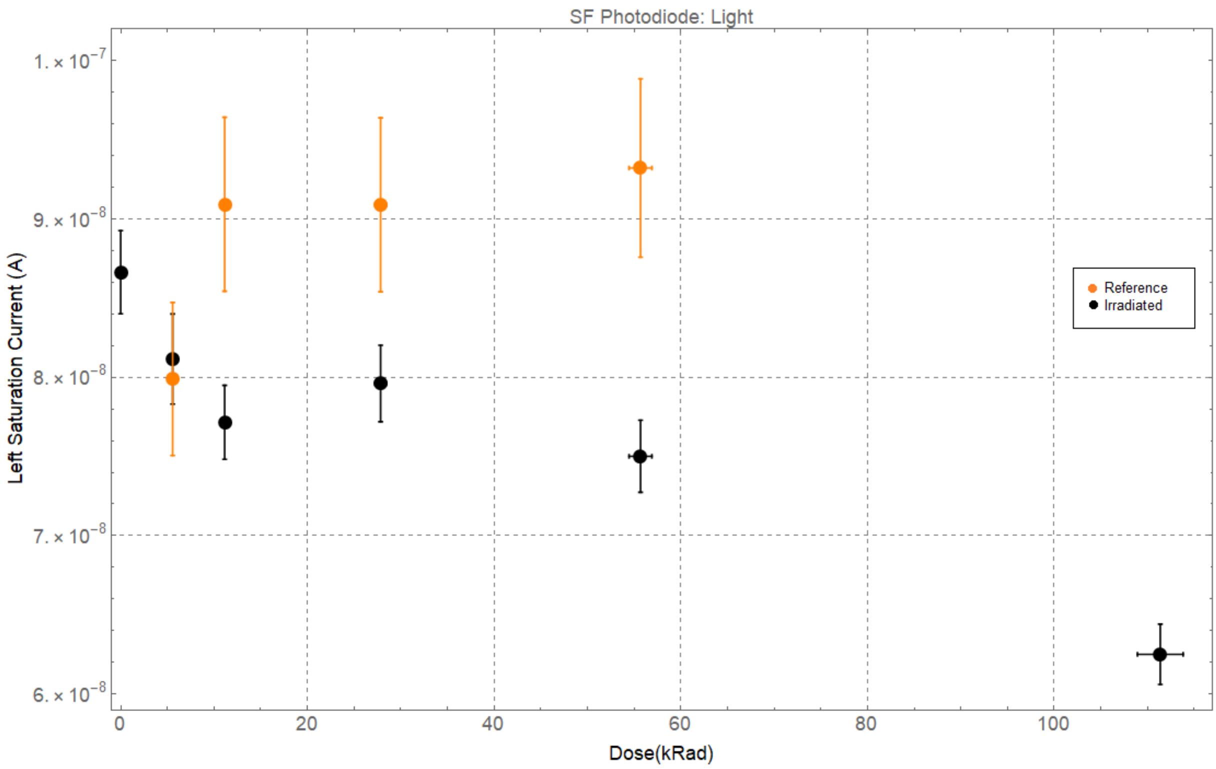

Figure 5.7: Left saturation current for the SF photodiode, in the presence of light, dose plot and respective reference values.

5.6 Silicon PIN Photodiode (OP950)

For each sample of the OP950 Photodiode, the current was measured while sweeping the voltage in order to establish the saturation currents. These measurements were made for each irradiation step, for different light conditions ("Light" in the presence of artificial room light and "Dark" where the component was covered). The I-V curves can be found in the appendix (A). For each irradiation step the result was obtained through a weighted average of the results of the different irradiated samples. These results from the 6 irradiation steps were aggregated, after checking its consistency, with the reference sample plotted for comparison. Due to a software error it was not possible to obtain the Step 2 reference data.

This component presents no notable results except for the right saturation current (leakage current) for the light case (figure 5.8), which was obtained by a weighted average of the data points of the interval 1.5V to 2V. However, just like the previous one, by comparing it with the reference, the apparent variation is of the same order as the fluctuations. As before, while it can be seen a similar effect in the right saturation current for the dark case, it is lower than the order of the dark current (typically 10^{-9} A).

Thus, the OP photodiode's saturation currents seem to be independent of the dose.

From those results, it can be concluded that this component cannot be used as a dosimeter, at least for these doses. For its utility as a high dose dosimeter more tests with a higher dose should be performed.

It could also be interesting to evaluate the measures with the component biased in order to collect the semiconductor generated charge during the irradiation.

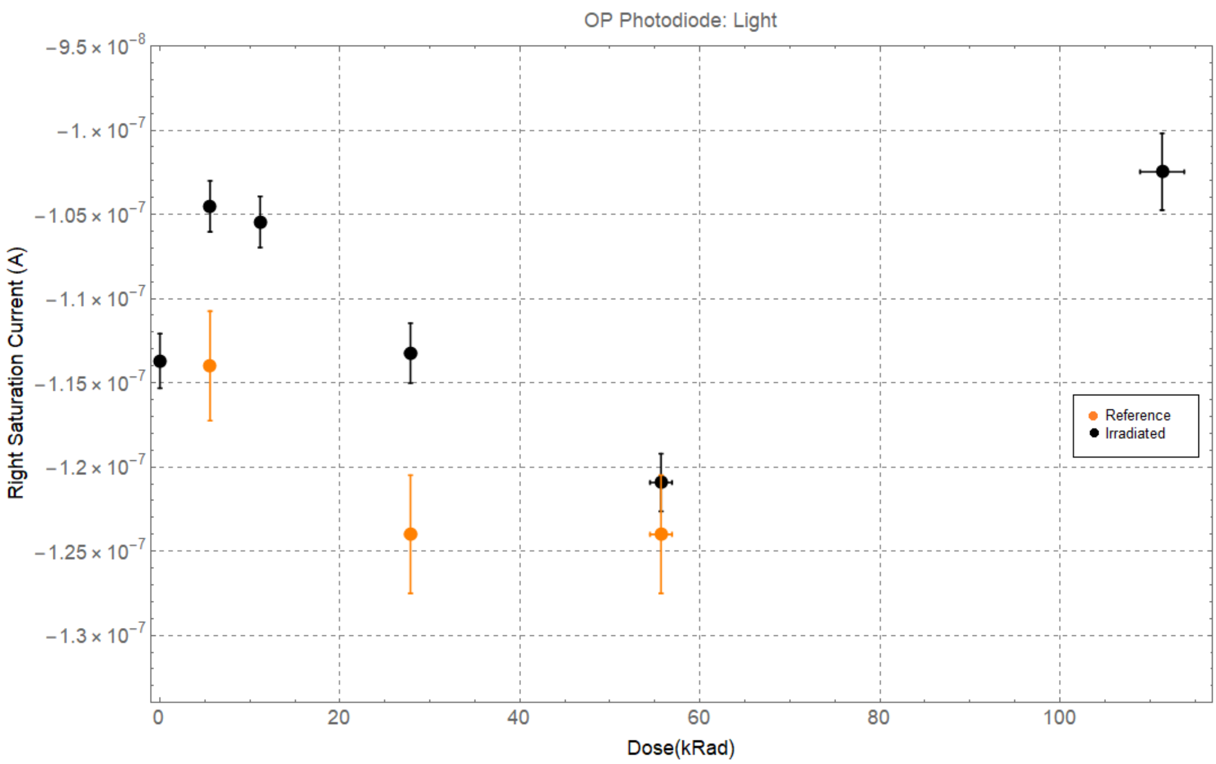

Figure 5.8: Right saturation current for the OP photodiode, in the presence of light, dose plot and respective reference values.

5.7 CCD Linear Image Sensor (TCD1304DG)

The aim was to irradiate the CCD and measure the output current and voltage in different light conditions: ”Light” in the presence of artificial light, ”Dark 1” where the component was covered, and ”Dark 2” where after the component was exposed to light, it was covered again in order to check if the accumulated charge was being collected or if there was a problem with the experimental setup.

With only one sample it was not possible to have a reference sample, but several measurements were made prior to the irradiation to check for fluctuations.

A linear relationship in the dose plots can be observed, and thus by fitting the average output current with the dose by using the least squares method, the following results are obtained in table 5.3 and figure 5.9. It is noticeable how similar the fits are, which implies that the output current (dark current) does not depend on the light conditions.

As expected, due to the low sampling rate of the measuring equipment, it was not possible to measure neither individual pixels nor their average value as seen in the voltage plots.

From those results, it can be concluded that this component can be used as a dosimeter.

Light Condition	m	b	χ^2/dof
Dark 1	(-1.50 $\pm$ 0.04) $\cdot$ 10^{-5}	(3.03 $\pm$ 0.02) $\cdot$ 10^{-3}	1.55
Dark 2	(-1.47 $\pm$ 0.04) $\cdot$ 10^{-5}	(3.00 $\pm$ 0.02) $\cdot$ 10^{-3}	1.13
Light	(-1.47 $\pm$ 0.04) $\cdot$ 10^{-5}	(3.00 $\pm$ 0.02) $\cdot$ 10^{-3}	1.34

Table 5.3: Fitting parameters for $V = m \cdot x + b$, using the least-squares method.

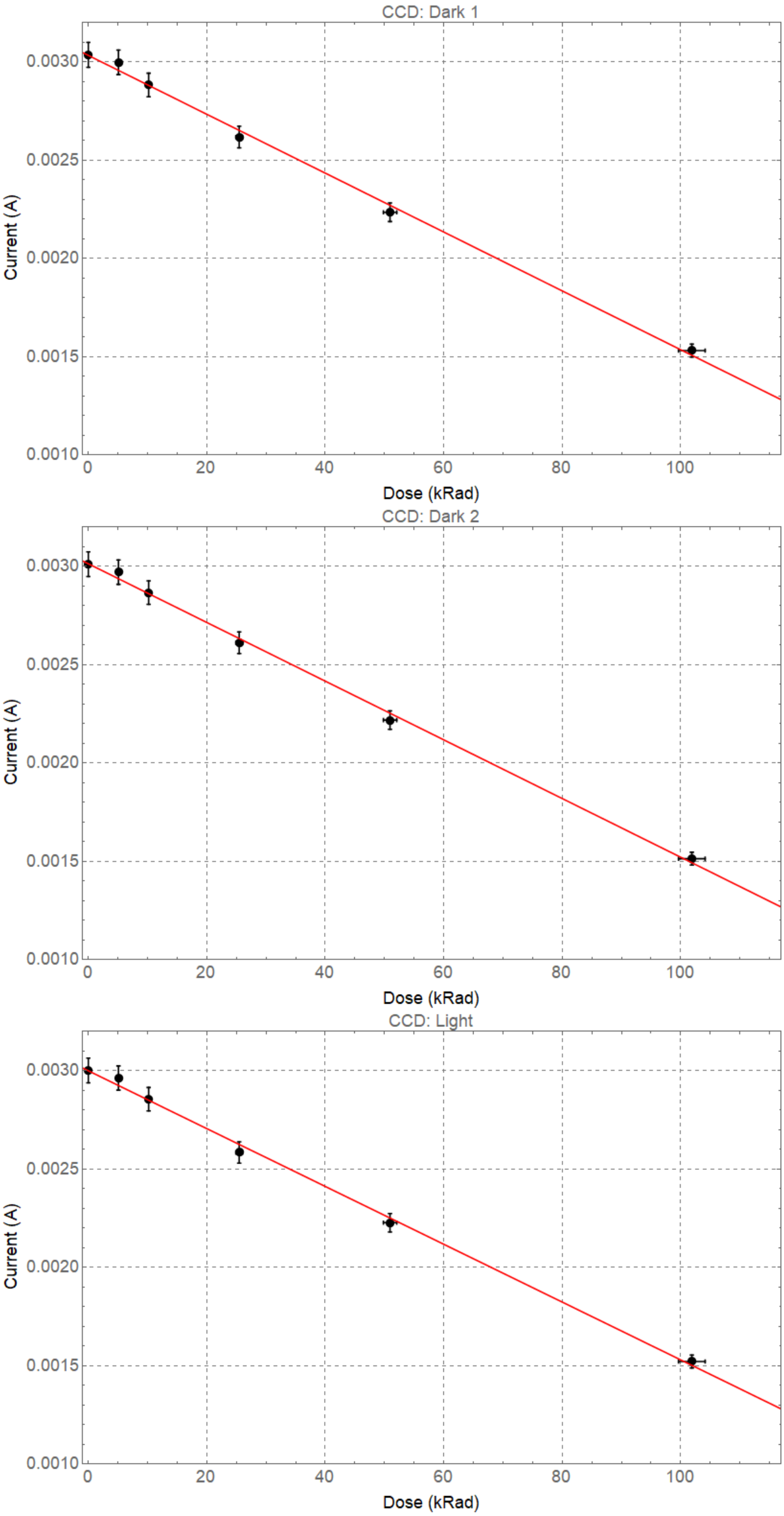

Figure 5.9: CCD dose plot for the average output voltage in the dark, in the dark after light exposure, and in the light.

5.8 Final Results

From table 5.4 and the plots from figure 5.10 we can observe the sensitivity of the three components that can be used as a dosimeter for different dose intervals.

The P MOSFET, for low doses, with VGS at 2V, can be used as a good dosimeter, as we can see its high sensitivity for the 0 to 20 kRad interval. However, for higher doses, the sensitivity decreases due to component saturation.

The N MOSFET with V_{GS} at 2V, can be used as a very good dosimeter for an increased effective range, higher than the previous MOSFET, with a good sensitivity over the tested dose range.

The CCD's dark current appears to be a good parameter for this device's use as a dosimeter since it appears to have a good linear dependency with the dose regardless of the light conditions, even though it has a lower sensitivity and needs to be measured with a higher precision instrument.

Sensitivity (mA/kRad)	[0, 20] kRad	[20, 40] kRad	[40, 60] kRad	[60, 120] kRad
MOSFET P	[0.46 , 2.6]	[0.09 , 0.46]	[0.02 , 0.09]	[0 , 0.02]
MOSFET N	[2.9 , 3.4]	[2.4 , 2.9]	[2.1 , 2.4]	[1.3 , 2.1]
CCD	0.015	0.015	0.015	0.015

Table 5.4: Component sensitivity for certain dose intervals.

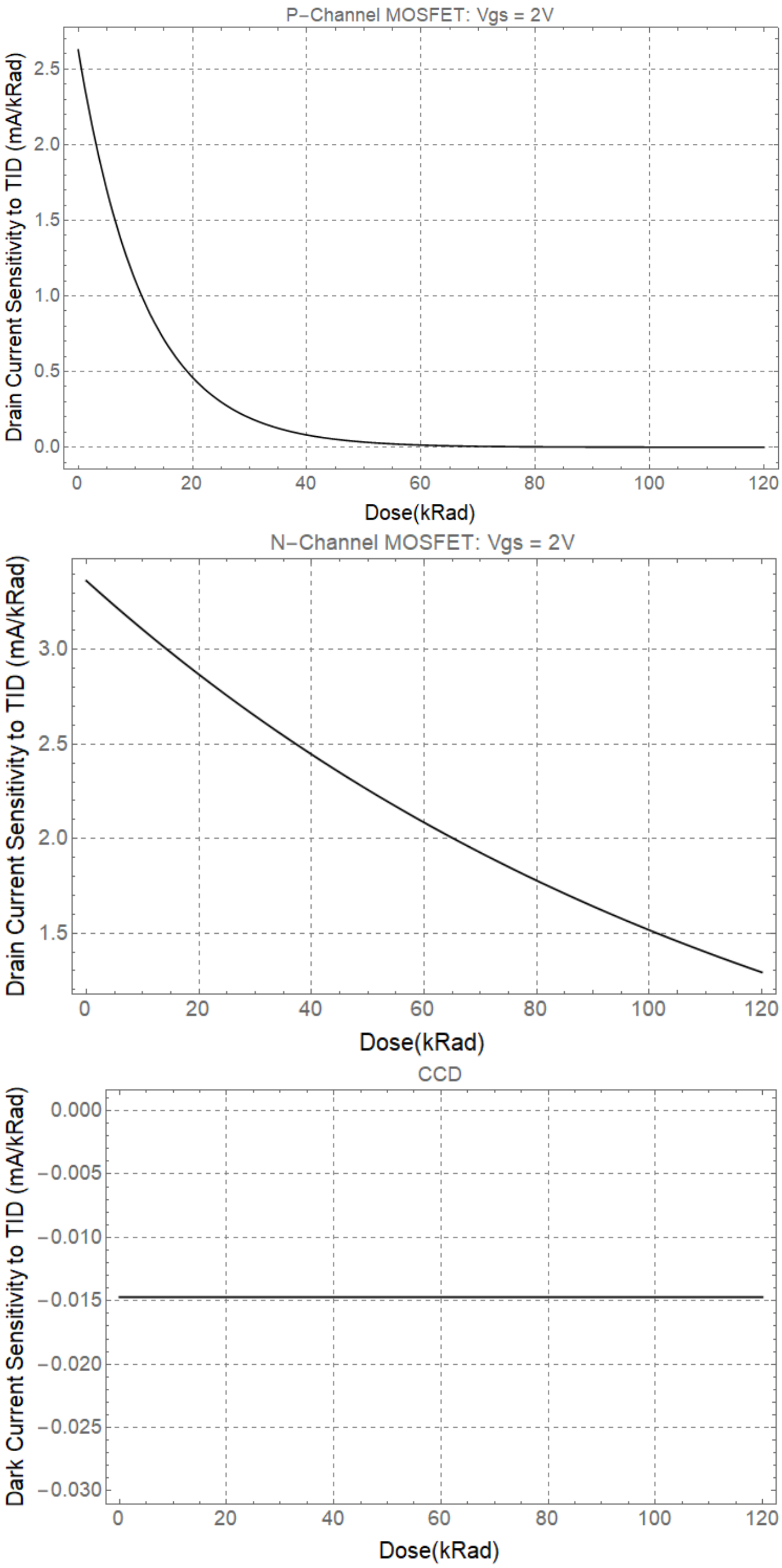

Figure 5.10: Current sensitivity to TID for the three different components as a function of the dose.

Chapter 6

Conclusion

In this work it was verified that ionizing damage affects differently different electronic components, with the most affected being the MOSFET.

It was analyzed the effects that the TID had on those component's oxide insulators, and verified a higher effect on components with an oxide layer rather than in those without as seen in the MOSFETs versus the photodiodes, where the later didn't have an oxide layer to trap charged carriers and generate observable TID effects for these doses.

For the P-Channel MOSFETs, TP2104, a notable increase of the saturation current was observed. For low doses, with V_{GS} at 2V, this component can be used as a good dosimeter, however, for higher doses, we'd have to increase the V_{GS}, which also increases the measurement error, having a trade-off between effective range and precision.

The N-Channel MOSFET 2N7000 revealed a considerable decrease of the saturation current. With V_{GS} at 2V, it can be used as a very good dosimeter for an increased effective range, higher than the previous MOSFET. By varying the V_{GS} it could be used as a fuse for very high doses, where the MOSFET would break down or burn, since a higher dose results in a very high current.

The OP-AMPs seem to be radiation-hard, since there is no notable dependency of their offset current and voltage with the dose. This could be related to their internal composition, since they're composed of several transistors (both P and N) which may cancel out each other.

The CCD's dark current appears to be a good parameter for this device's use as a dosimeter since it appears to have a good linear dependency with the dose regardless of the light conditions.

It is to be noted that it was disregarded other types of interaction or other particles (for example, displacement damage and high energy neutrons, respectively).

For the future, tests should be performed with photodiodes biased during the irradiation or at higher doses; other parameters for the OP-AMPs should be analyzed, such as the frequency response; additionally, a measuring system for the CCD with a high enough sampling rate for individual pixel analysis should be used; and finally, the effects of different dose rates on the same components should also be studied.

In conclusion, it was verified that we can use cheap COTS components such as MOSFETs, to measure TID up to at least a 100 kRad, the typical dose for the maximum flare, making it possible to ensure a quality space research at a much lower price.

Bibliography

[1] "A guide to space radiation," http://www.sws.bom.gov.au/Category/Educational/Space%20Weather/Space%20Weather%20Effects/guide-to-space-radiation.pdf, cited in June 2019.

[2] G. Barbottin and A. Vapaille, "Instabilities in silicon devices, new insulators, devices and radiation effects," *Elsevier*, 1999.

[3] A. Jorio, A. Zounoubi, Z. Elachheb, C. Carlone, and S. M. Khann, "Displacement damages created by γ particles radiation in n type gaas," *M. J. of Condensed Matter*, 1999.

[4] R. Sujatha, A. R. Khan, M. Ravindra, and R. Damle, "Study of the effect of gamma radiation on mosfet for space applications," *Indian Journal of Pure and Applied Physics*, 2018.

[5] X. Shoulong, Z. Shuliang, and H. Youjun, "γ -ray detection using commercial off-the-shelf cmos and ccd image sensors," *IEEE Sensors Journal*, vol. 17, no. 20, pp. 6599–6604, Oct 2017.

[6] H. Jafari, S. A. H. Feghhi, and S. Boorboor, "Evaluation of gamma dose effect on PIN photodiode using analytical model," *Radiation Physics and Chemistry*, vol. 144, pp. 379–385, Mar. 2018.

[7] H. A. Ashry, F.A.S.Soliman, A. Swidan, S.M.El-Ghanam, and W. A. A. Rahman, "Gamma radiation effects on the electrical parameters of some operational amplifiers," 2007.

[8] R. Silberberg, C. H. Tsao, and J. H. Adams-Jr., "Radiation doses and let distributions of cosmic rays," *Radiation Search*, 1984.

[9] G. D. et al., "Assessment of radiation exposure of astronauts in space." *The International Commission on Radiological Protection Technical report*, 2013.

[10] G. Santin, P. Truscott, R. Gaillard, and R. G. Alía, "Radiation environments: space, avionics, ground and below," p. 132, 2017.

[11] V. Ferlet-Cavrois, "Electronic radiation hardening radiation hardness assurance and technology demonstration activities," 2011.

[12] A. Holmes-Siedle and L. Adams, "Radfet: A review of the use of metal-oxide-silicon devices as integrating dosimeters," 1986.

[13] K. Khurshid, R. Mahmood, and Q. Islam, "A survey of camera modules for cubesats - design of imaging payload of icube-1," 2013.

[14] B. Kainka, "Measure gamma rays with a photodiode," 2016.

[15] M. Khazhmuradov, N. Kochnev, and D. Fedorchenko, "Pin photodiodes for gamma radiation measurements," 2012.

[16] D. Makowski, “The impact of radiation on electronic devices with the special consideration of neutron and gamma radiation monitoring,” *PhD Thesis, Lodz, Tech. U.*, 2006.

[17] L. H. Claro and J. A. dos Santos, “Effects of gamma radiation on commercial operational amplifiers,” *International Nuclear Atlantic Conference*, 2009.

[18] J. J. Cogliati, K. W. Derr, and J. Wharton, “Using CMOS Sensores in a Cellphone for Gamma Detection and Classification,” 2014.

[19] C. Poivey, “Section I: Total Ionizing and Non-Ionizing Dose Radiation Hardness Assurance,” *IEEE Nuclear and Space Radiation Effects Conference Short Course Notebook*, July 2017.

[20] L. J. Asensio, M. A. Carvajal, J. A. López-Villanueva, M. Vilches, A. M. Lallena, and A. J. Palma, “Evaluation of a low-cost commercial mosfet as radiation dosimeter,” 2005.

[21] T. R. Oldham and F. B. McLean, “Total ionizing dose effects in MOS oxides and devices.” *IEEE Transactions on Nuclear Science*, vol. 50(3), p. 483–499, 2003.

[22] S. McKenna-Lawlor, P. Gonçalves, A. Keating, G. Reitz, and D. Matthia, “Overview of energetic particle hazards during prospective manned missions to Mars,” *Planetary and Space Science*, vol. 63, pp. 123–132, 2012.

[23] J. Sabino, “Radiation environment and effects in human spaceflight: A lunar mission,” *MA Thesis, Instituto Superior Técnico*, 2012.

[24] A. Casimiro, “Efeitos do ambiente de radiação espacial em missões tripuladas a marte,” *MA Thesis, Instituto Superior Técnico*, 2016.

[25] P. Alves, “Radiation hardness assessment of mr sensors for space applications,” *MA Thesis, Instituto Superior Técnico*, 2017.

[26] M. Pinto, “Development of a directionality detector and radiation hardness assurance for radem, the esa juice mission radiation monitor,” *PhD Thesis, Instituto Superior Técnico*, 2019.

Appendix A

Appendix chapter

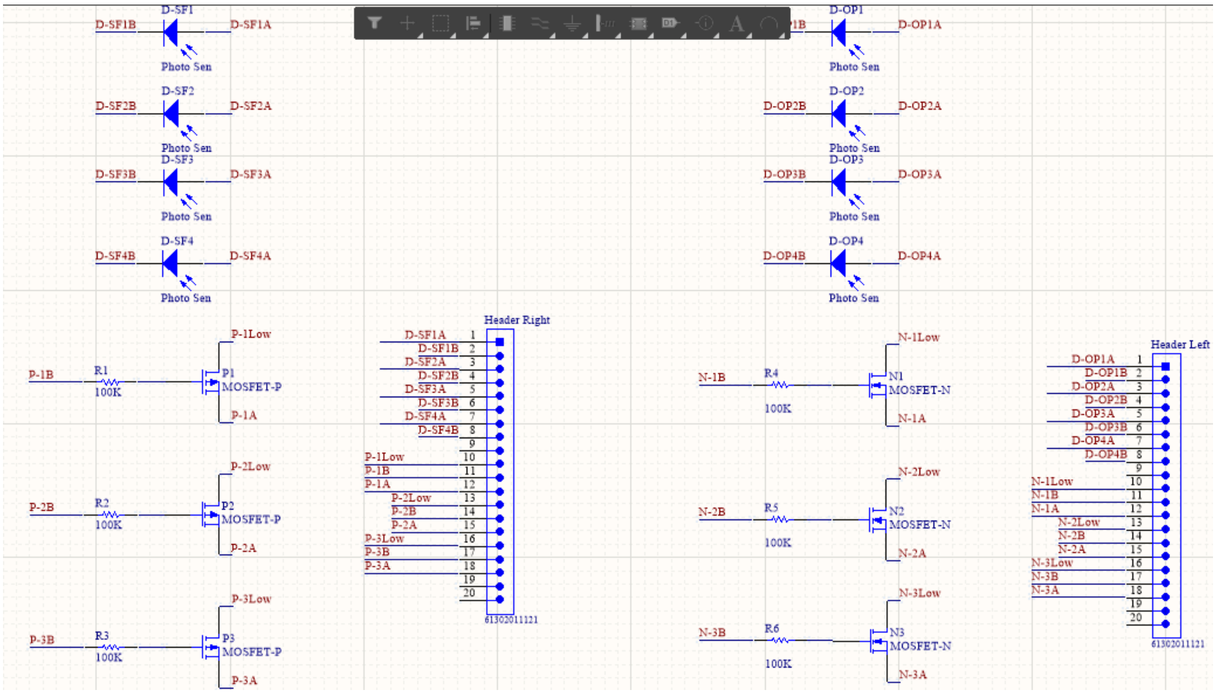

Figure A.1: Schematics of the MOSFET and Photodiode Circuits.

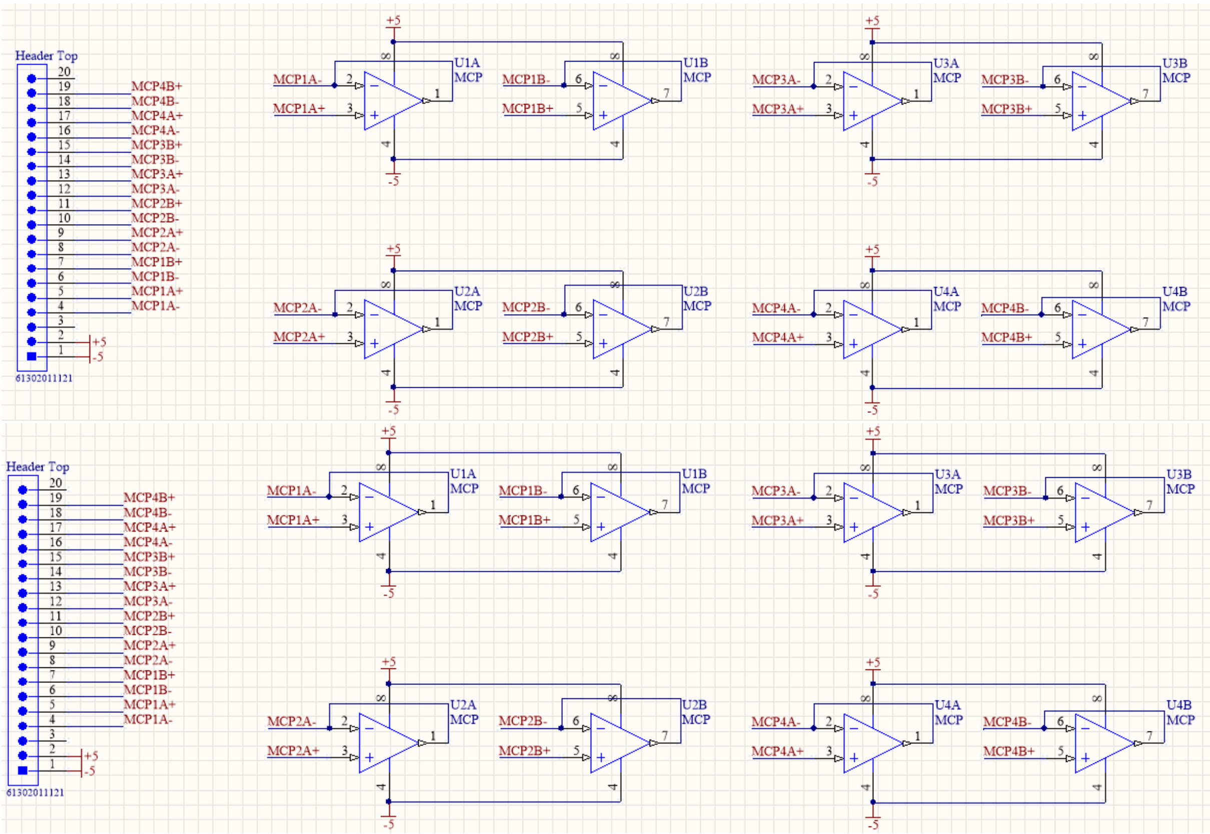

Figure A.2: Schematics of the OP-AMP Circuits.

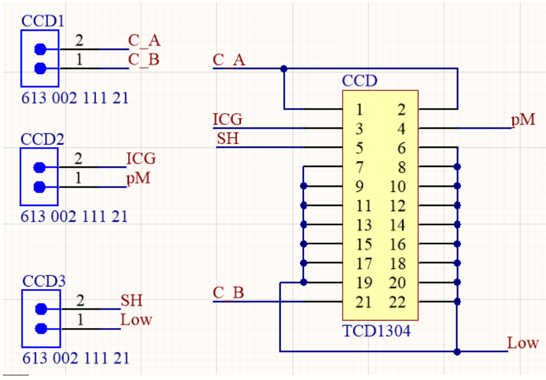

Figure A.3: Schematics of the CCD Circuit.

Models 2634B, 2635B and 2636B System SourceMeter® Instrument Specifications

VOLTAGE ACCURACY SPECIFICATIONS[2,3]

Range	Source: Programming resolution	Source: Accuracy ± (% reading + volts)	Source: Typical Noise (Peak to Peak) 0.1 Hz to 10 Hz	Measure: Display resolution	Measure: Accuracy[4] ± (% reading + volts)
200 mV	5 µV	0.02 % + 375 µV	20 µV	100 nV	0.015 % + 225 µV
2 V	50 µV	0.02 % + 600 µV	50 µV	1 µV	0.02 % + 350 µV
20 V	500 µV	0.02 % + 5 mV	300 µV	10 µV	0.015 % + 5 mV
200 V	5 mV	0.02 % + 50 mV	2 mV	100 µV	0.015 % + 50 mV

CURRENT ACCURACY SPECIFICATIONS[2]

Range	Source: Programming resolution	Source: Accuracy ± (% reading + amperes)	Source: Typical Noise (Peak to Peak) 0.1 Hz to 10 Hz	Measure: Display resolution	Measure: Accuracy[4] ± (% reading + amperes)
100 pA[5]	N/A	N/A	N/A	100 aA	0.15 % + 120 fA[6,7]
1 nA	20 fA	0.15 % + 2 pA	800 fA	1 fA	0.15 % + 240 fA[6,8]
10 nA	200 fA	0.15 % + 5 pA	2 pA	10 fA	0.15 % + 3 pA
100 nA	2 pA	0.06 % + 50 pA	5 pA	100 fA	0.06 % + 40 pA
1 µA	20 pA	0.03 % + 700 pA	25 pA	1 pA	0.025 % + 400 pA
10 µA	200 pA	0.03 % + 5 nA	60 pA	10 pA	0.025 % + 1.5 nA
100 µA	2 nA	0.03 % + 60 nA	3 nA	100 pA	0.02 % + 25 nA
1 mA	20 nA	0.03 % + 300 nA	6 nA	1 nA	0.02 % + 200 nA
10 mA	200 nA	0.03 % + 6 µA	200 nA	10 nA	0.02 % + 2.5 µA
100 mA	2 µA	0.03 % + 30 µA	600 nA	100 nA	0.02 % + 20 µA
1 A	20 µA	0.05 % + 1.8 mA	70 µA	1 µA	0.03 % + 1.5 mA
1.5 A	50 µA	0.06 % + 4 mA	150 µA	1 µA	0.05 % + 3.5 mA
10 A[9]	200 µA	0.5 % + 40 mA	N/A	10 µA	0.4 % + 25 mA

Figure A.4: Accuracy of the measuring equipment.

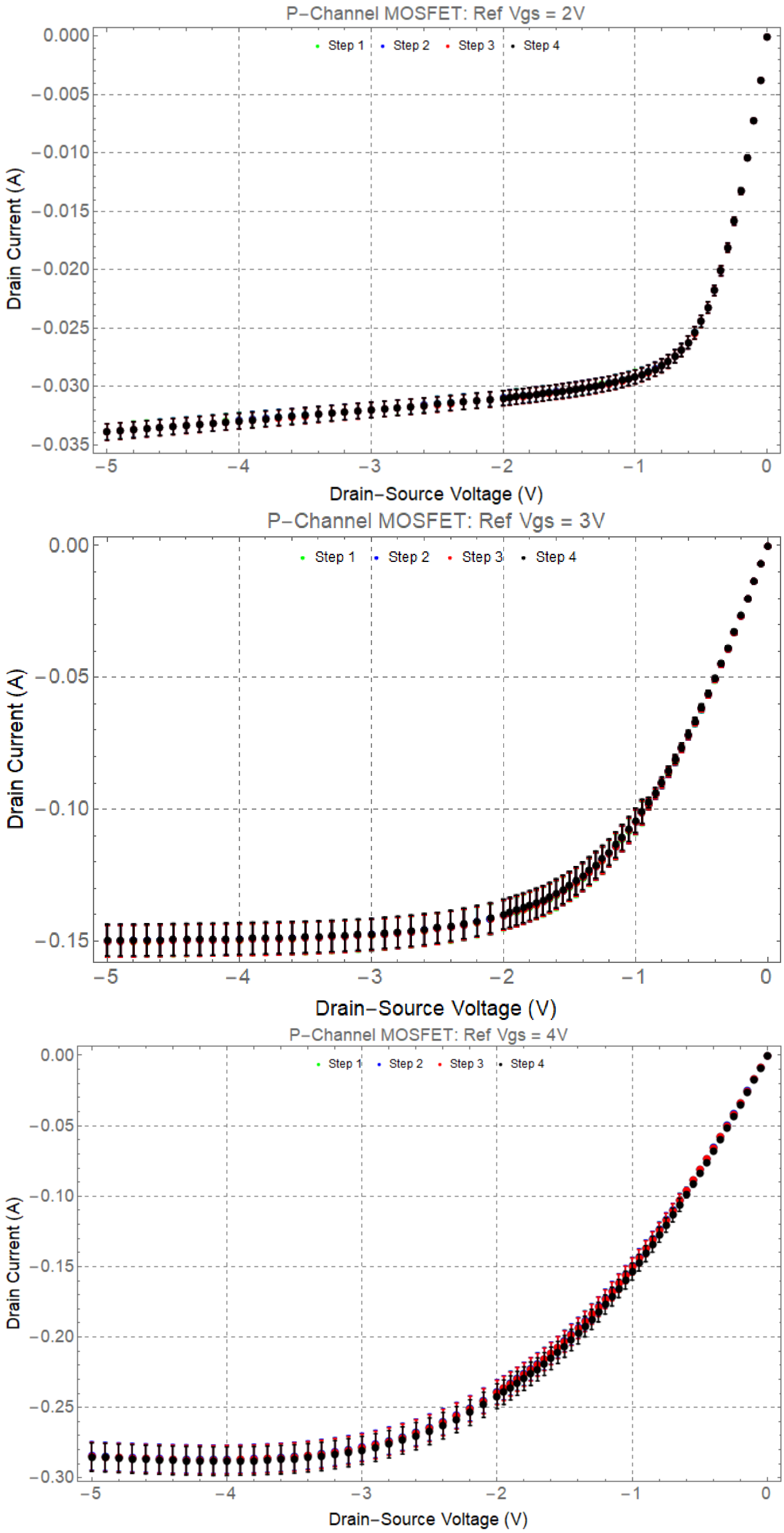

Figure A.5: Reference P-Channel MOSFET for Vgs equal to 2V, 3V and 4V, respectively.

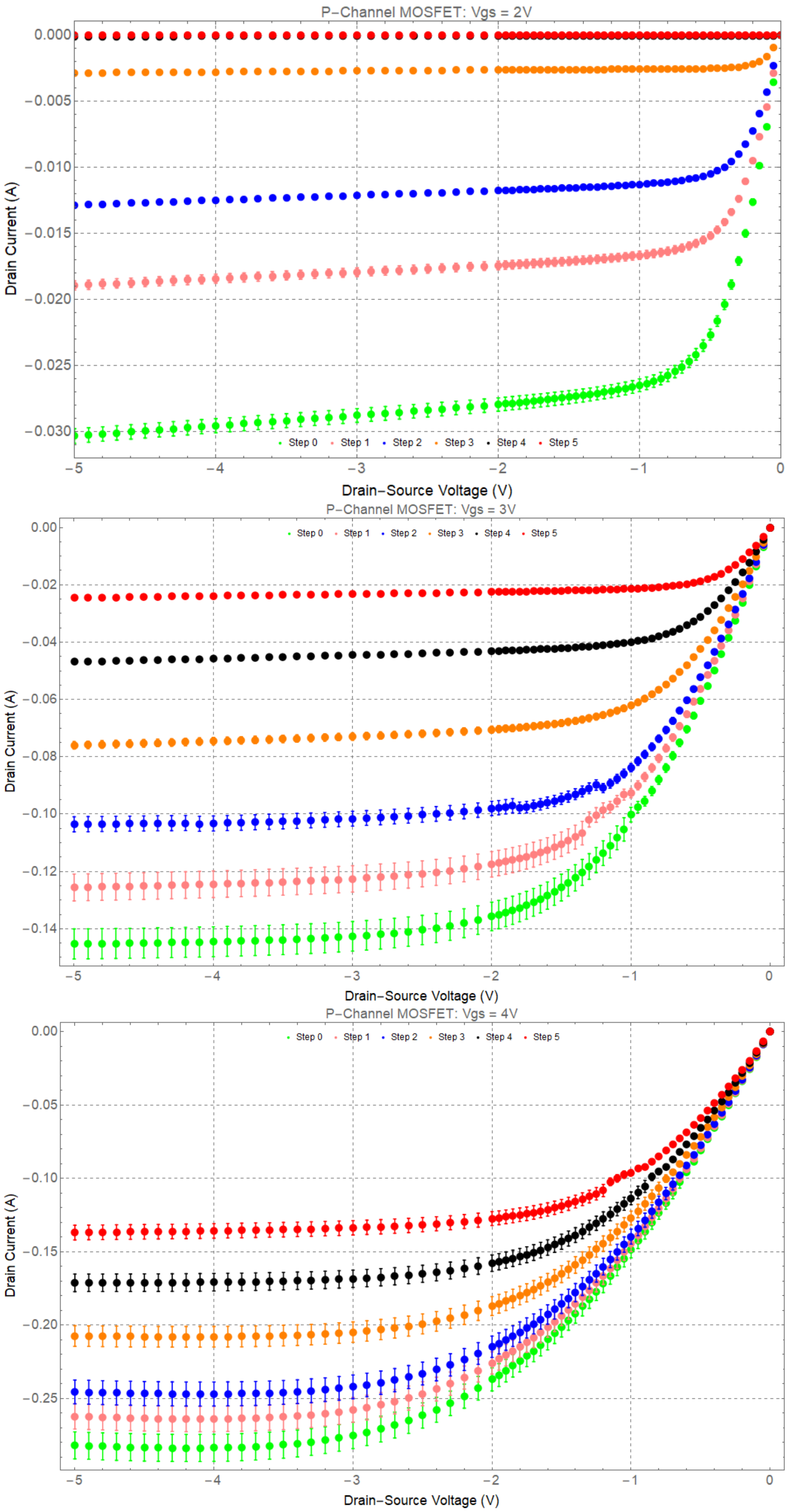

Figure A.6: P-Channel MOSFET for Vgs equal to 2V, 3V and 4V for the 5 irradiation steps.

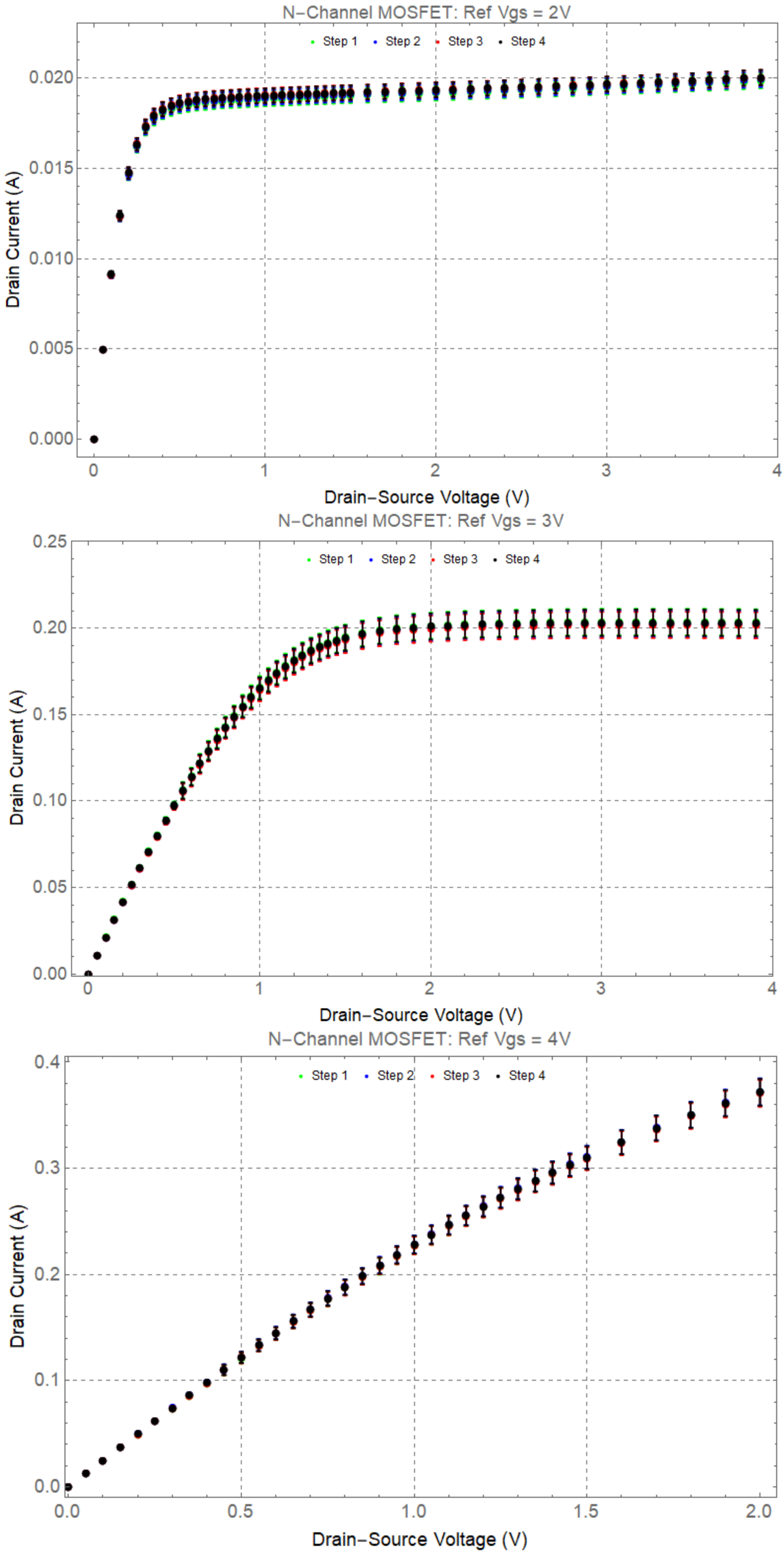

Figure A.7: Reference N-Channel MOSFET for Vgs equal to 2V, 3V and 4V.

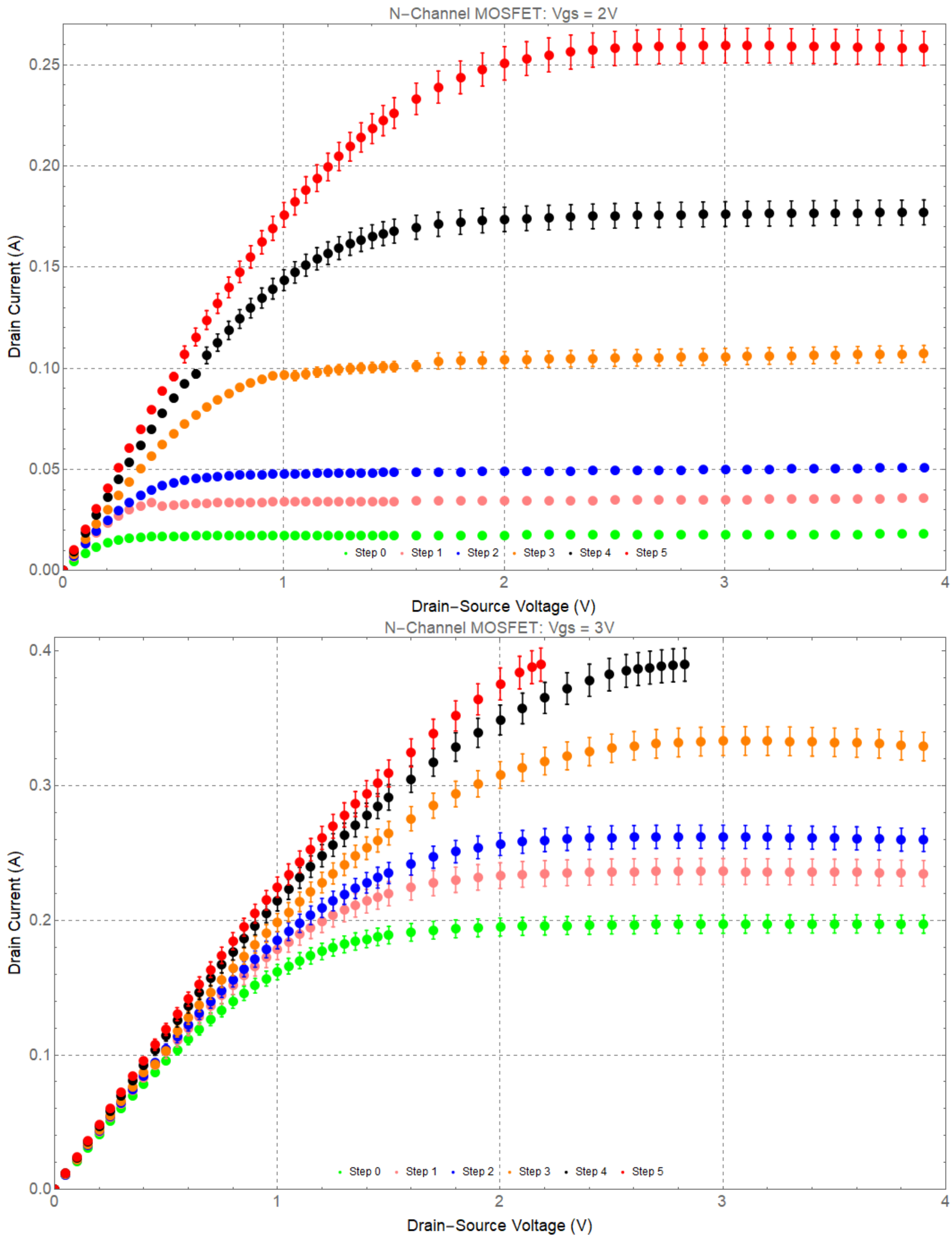

Figure A.8: N-Channel MOSFET for Vgs equal to 2V and 3V for the 5 irradiation steps.

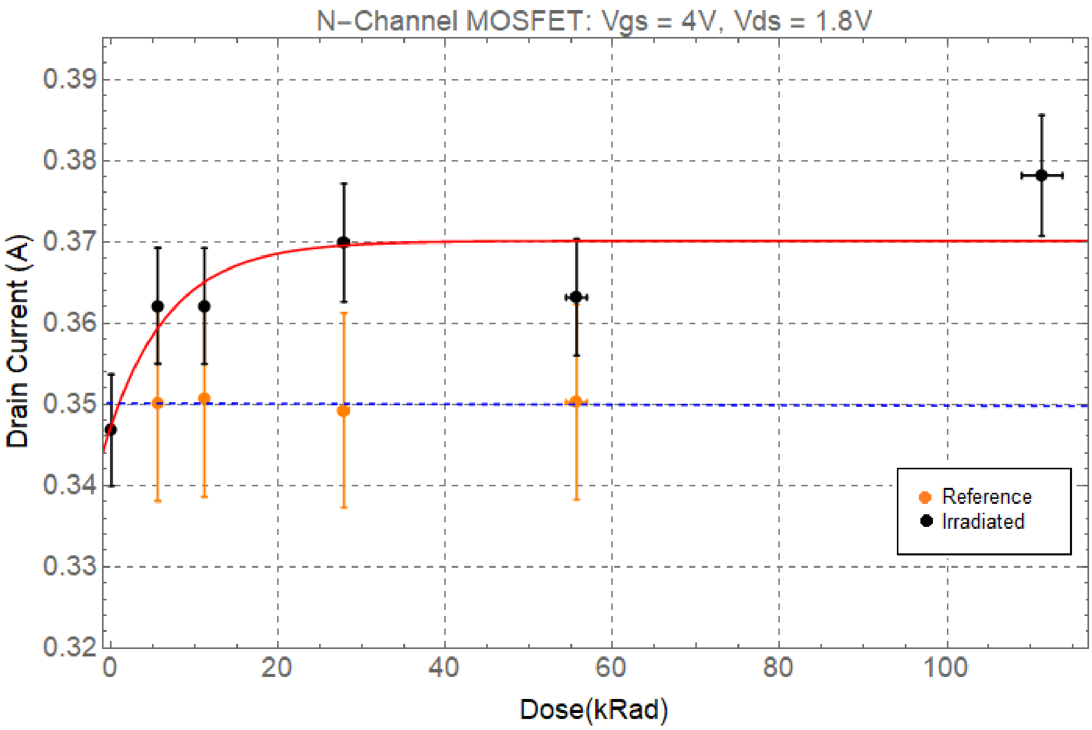

Figure A.9: N-Channel MOSFET's "saturation current" vs dose and reference values for the Vgs equal to 4V.

V_{GS}	k	m	o	χ^2/dof
4V	0.023 $\pm$ 0.0071	-0.135 $\pm$ 0.101	0.37 $\pm$ 0.0040	2.31

Table A.1: Fitting parameters for I_D = -k $e^{m \cdot x}$ + o, using the least-squares method.

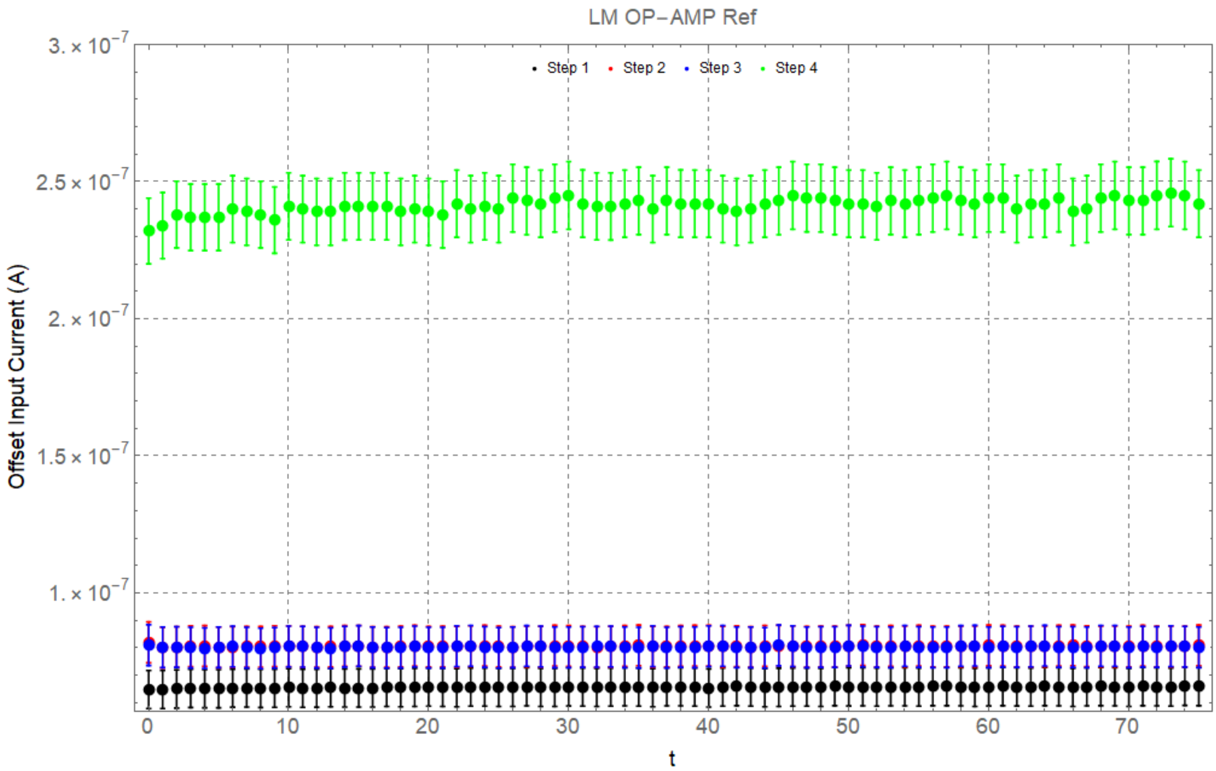

Figure A.10: Reference LM OP-AMP. t is an arbitrary time unit of the order of the second.

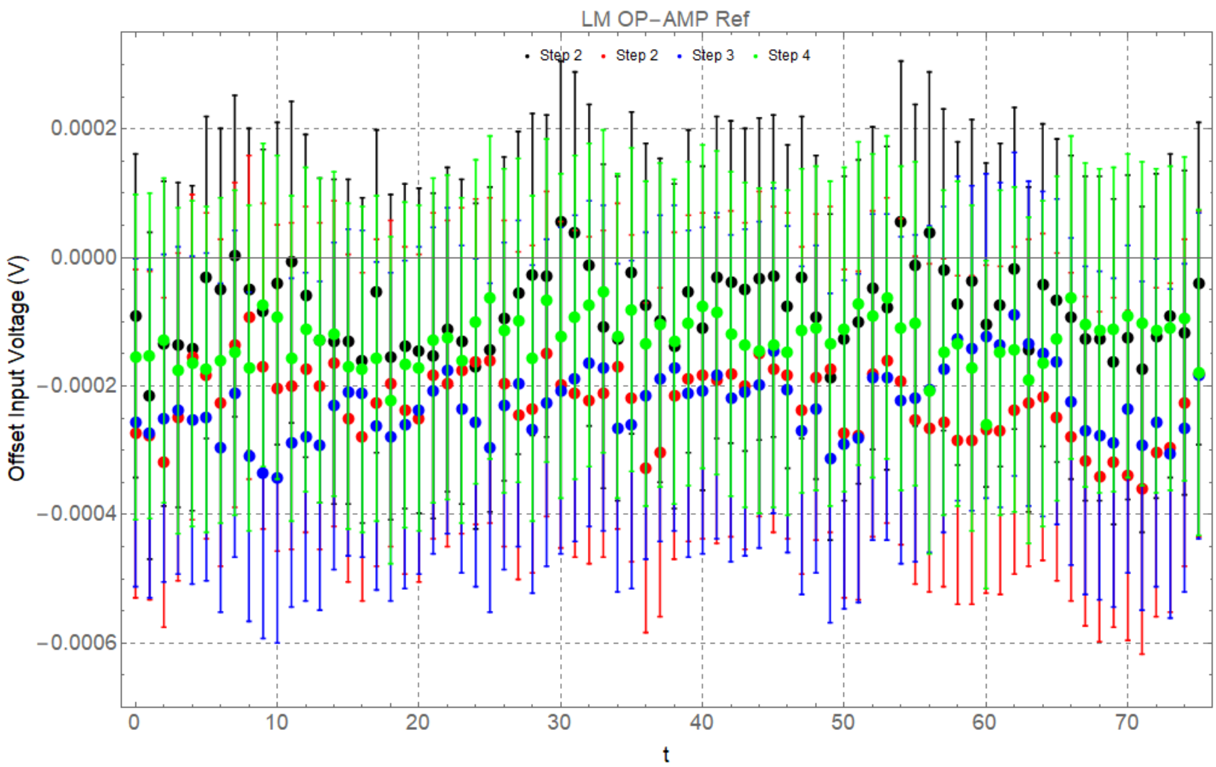

Figure A.11: Reference LM OP-AMP. t is an arbitrary time unit of the order of the second.

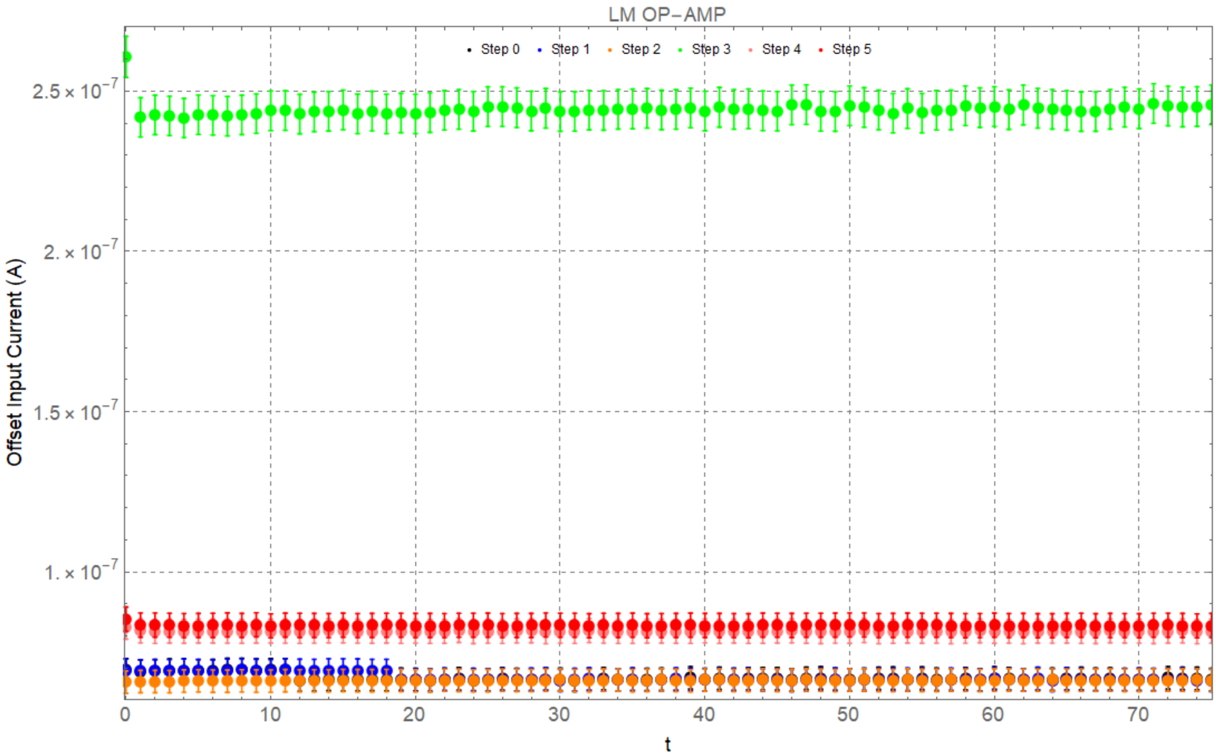

Figure A.12: LM OP-AMP offset input current plots for the 5 irradiation steps. t is an arbitrary time unit of the order of the second.

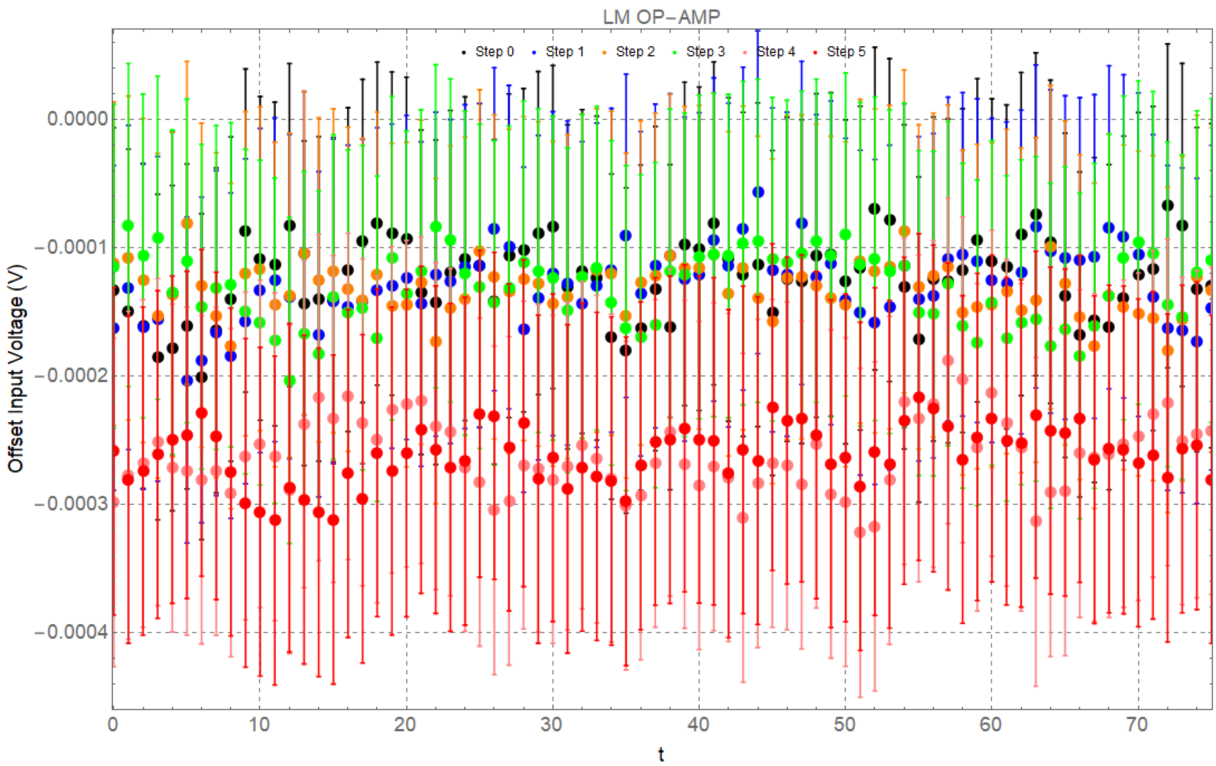

Figure A.13: LM OP-AMP offset input voltage plots for the 5 irradiation steps. t is an arbitrary time unit of the order of the second.

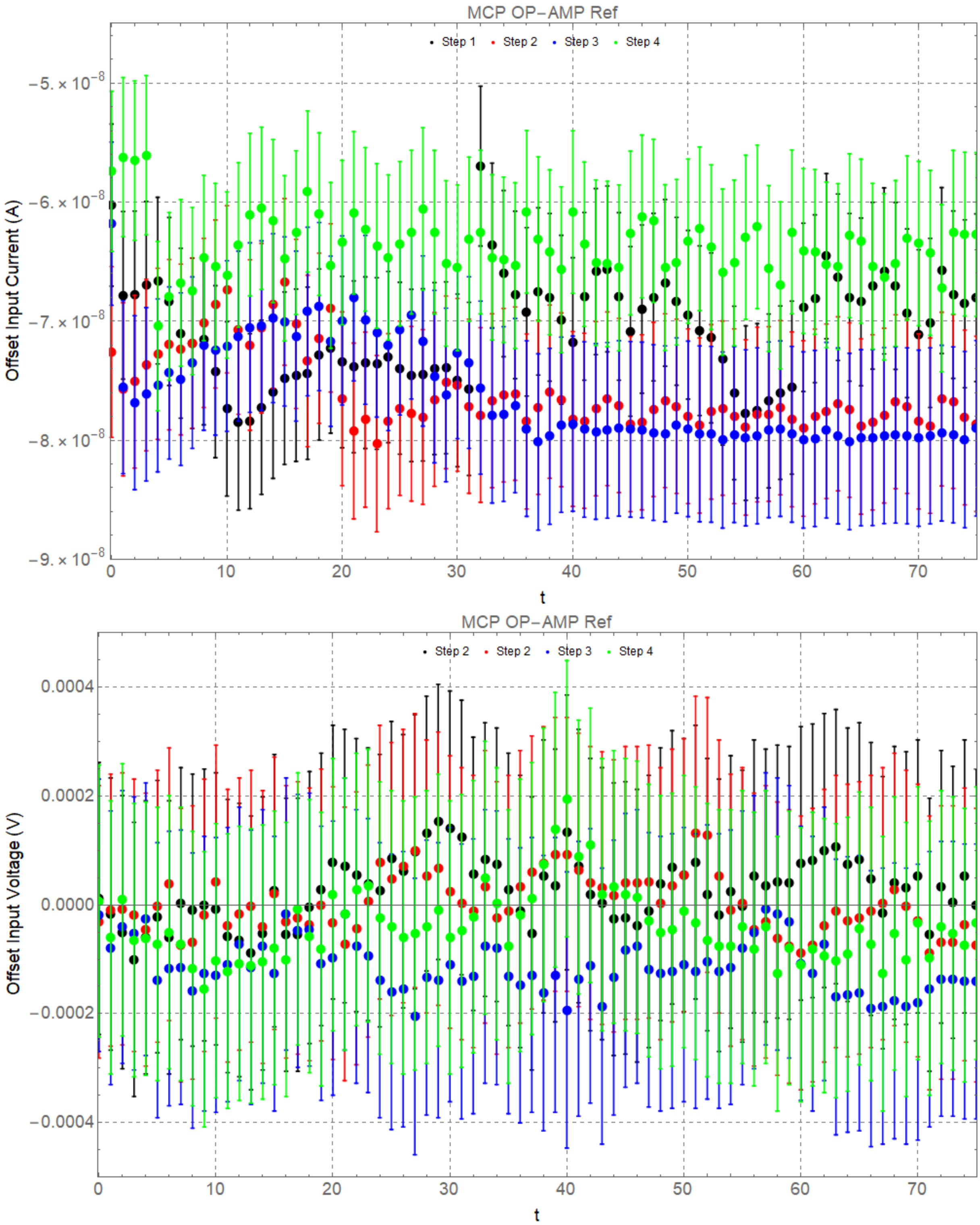

Figure A.14: Reference MCP OP-AMP. t is an arbitrary time unit of the order of the second.

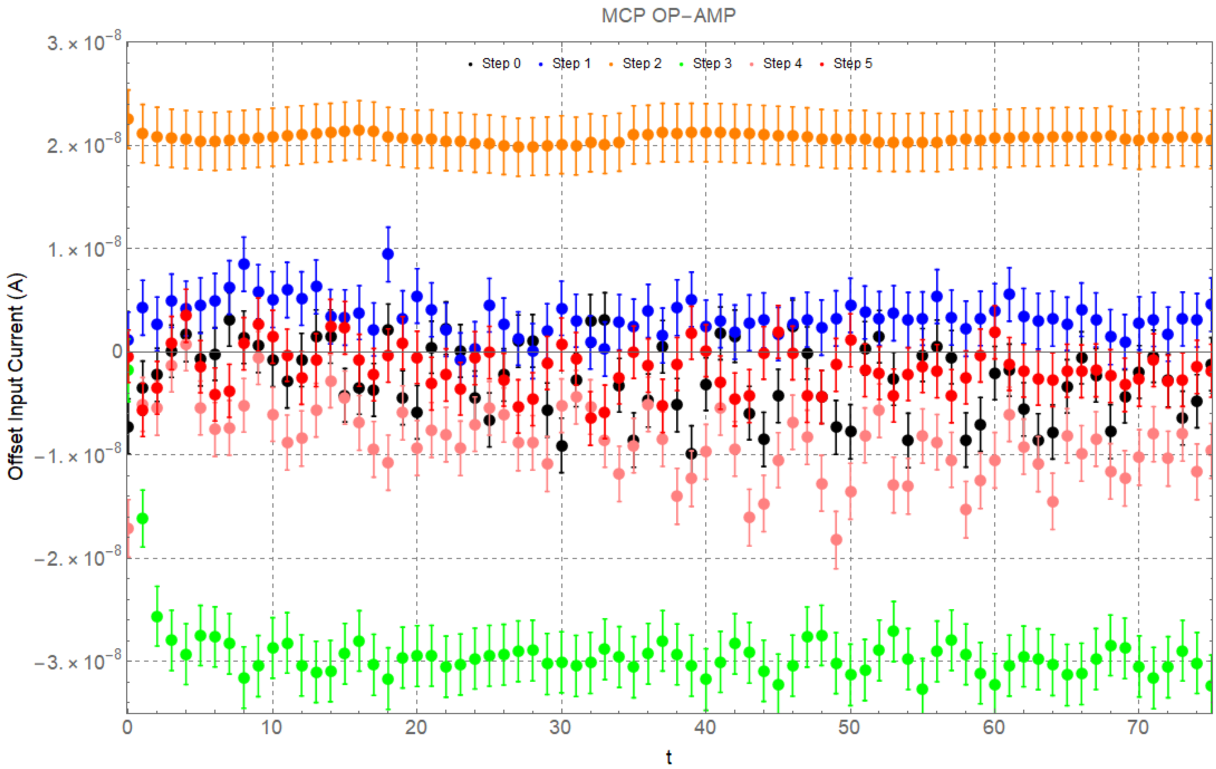

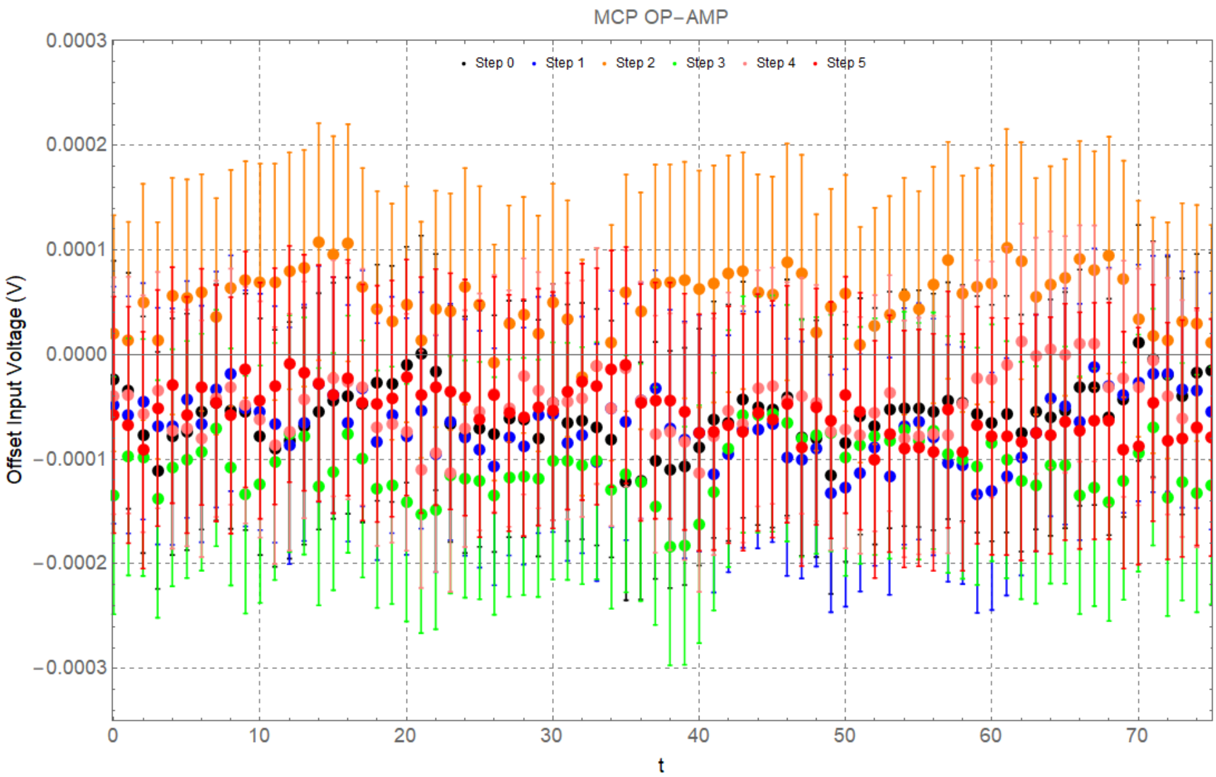

Figure A.15: MCP OP-AMP offset input current and voltage plots for the 5 irradiation steps. t is an arbitrary time unit of the order of the second.

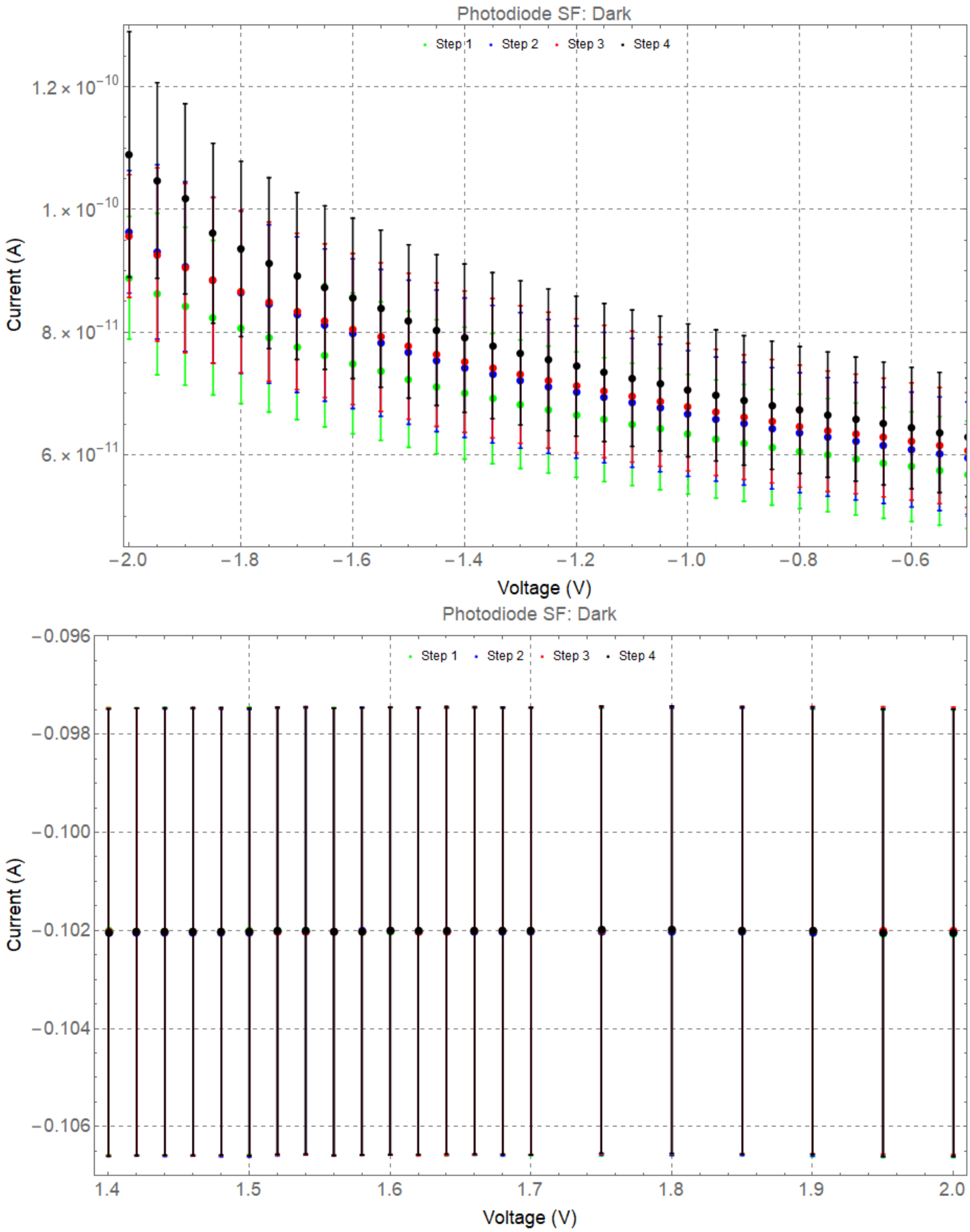

Figure A.16: Reference SF Photodiode's left and right saturation currents in the dark.

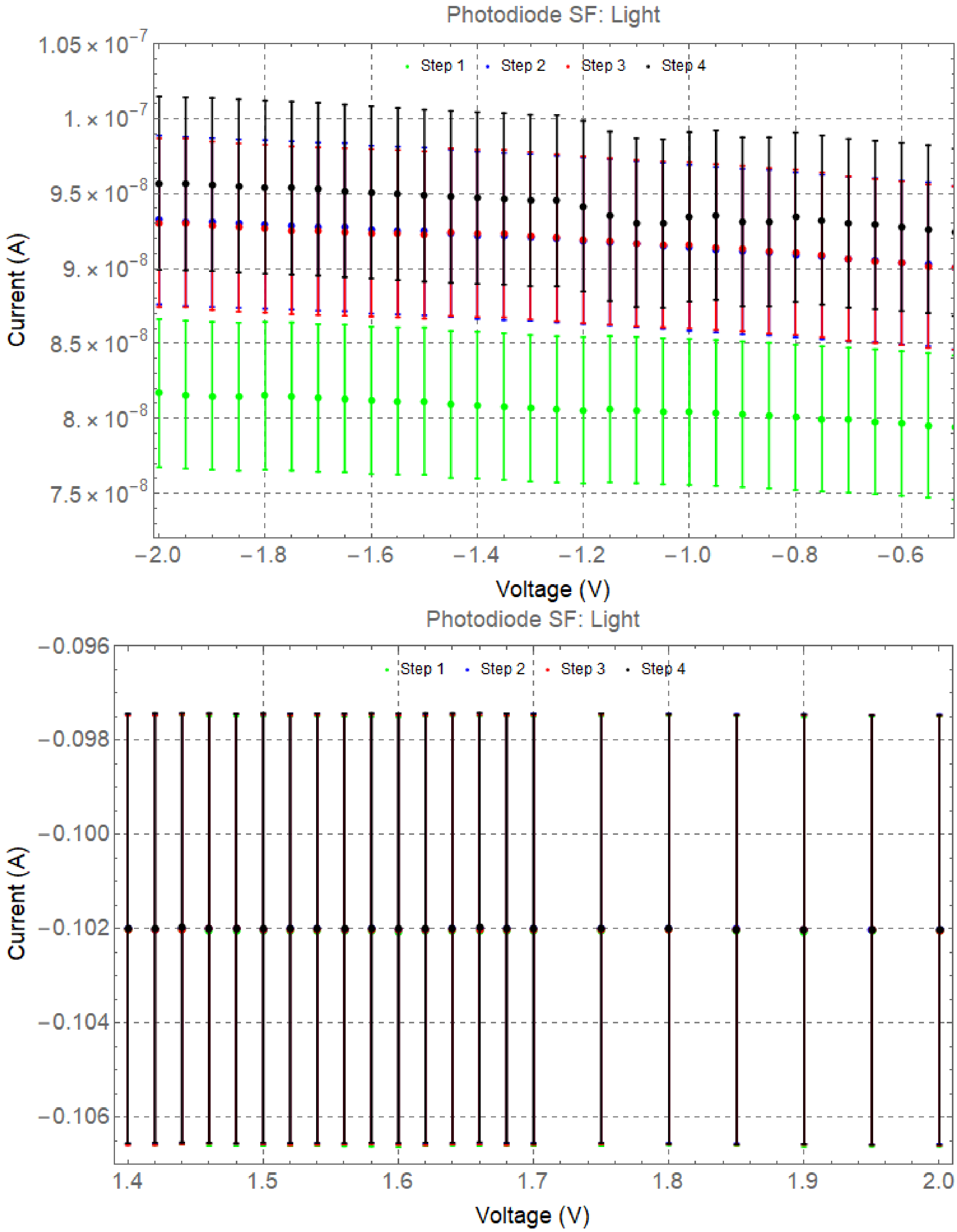

Figure A.17: Reference SF Photodiode's left and right saturation currents in the presence of light.

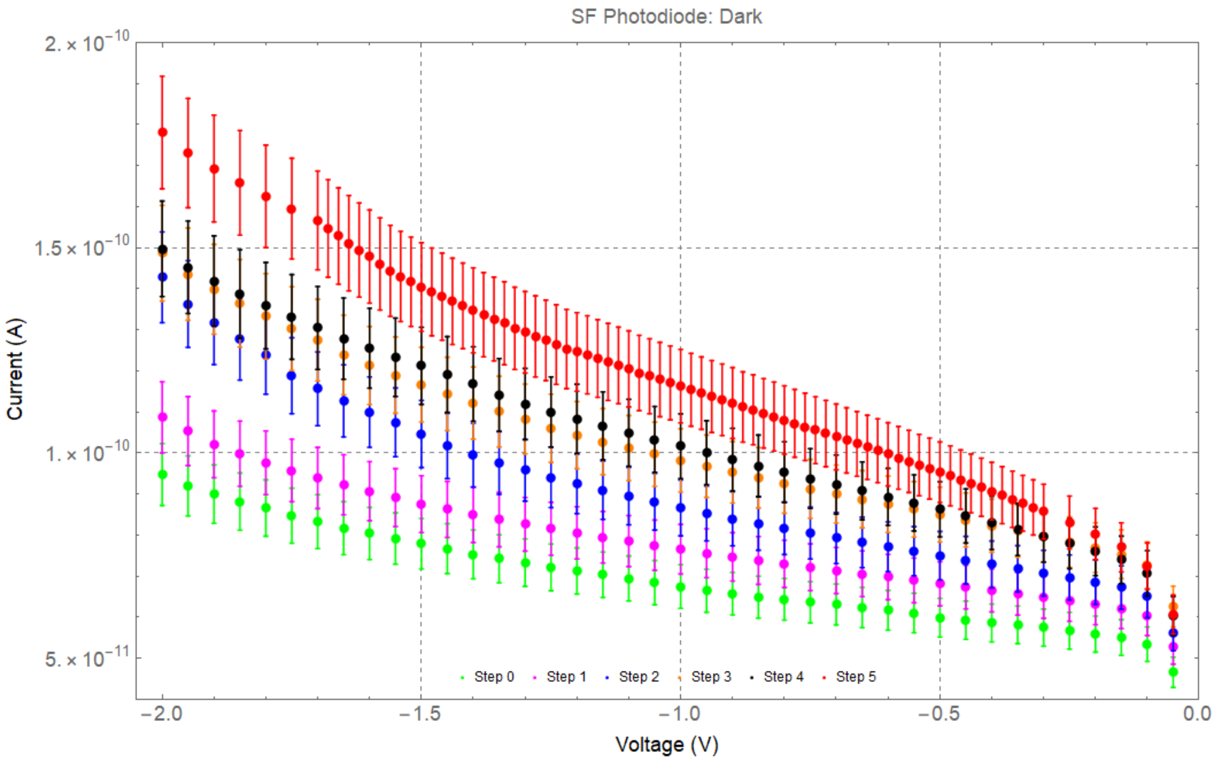

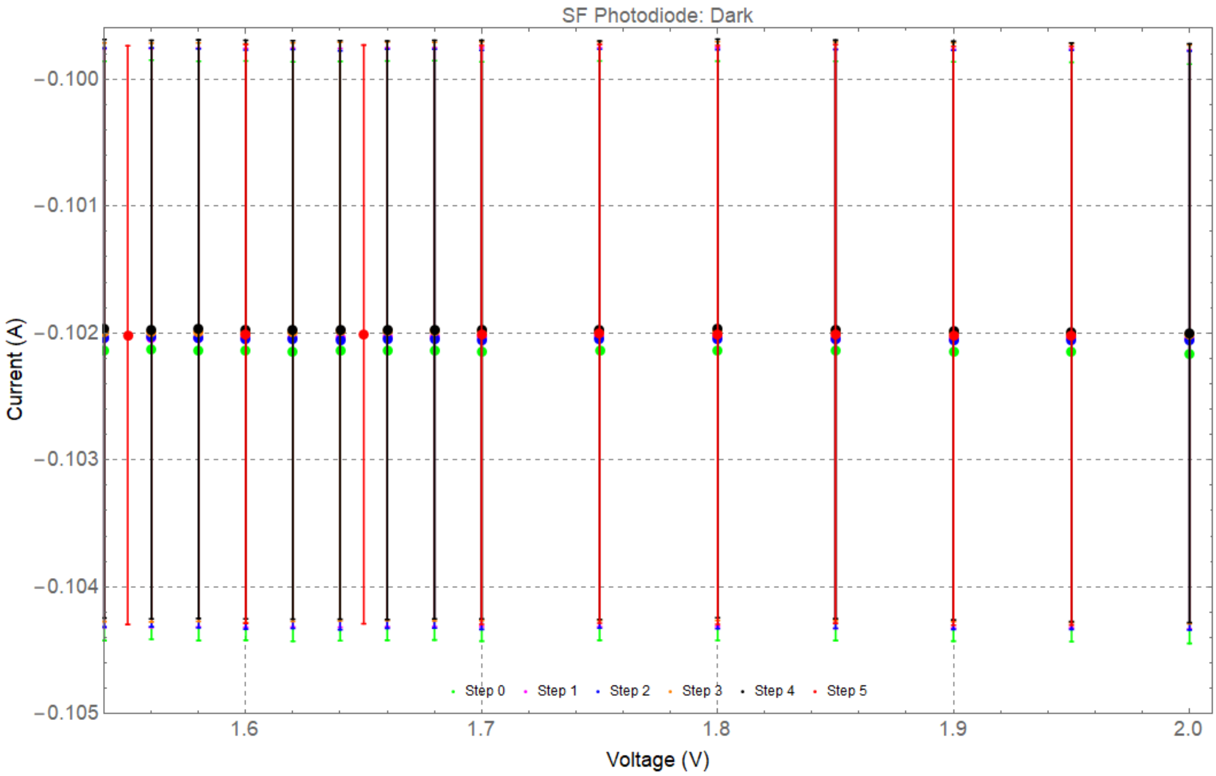

Figure A.18: SF photodiode's left and right saturation currents in the dark, for the 5 irradiation steps.

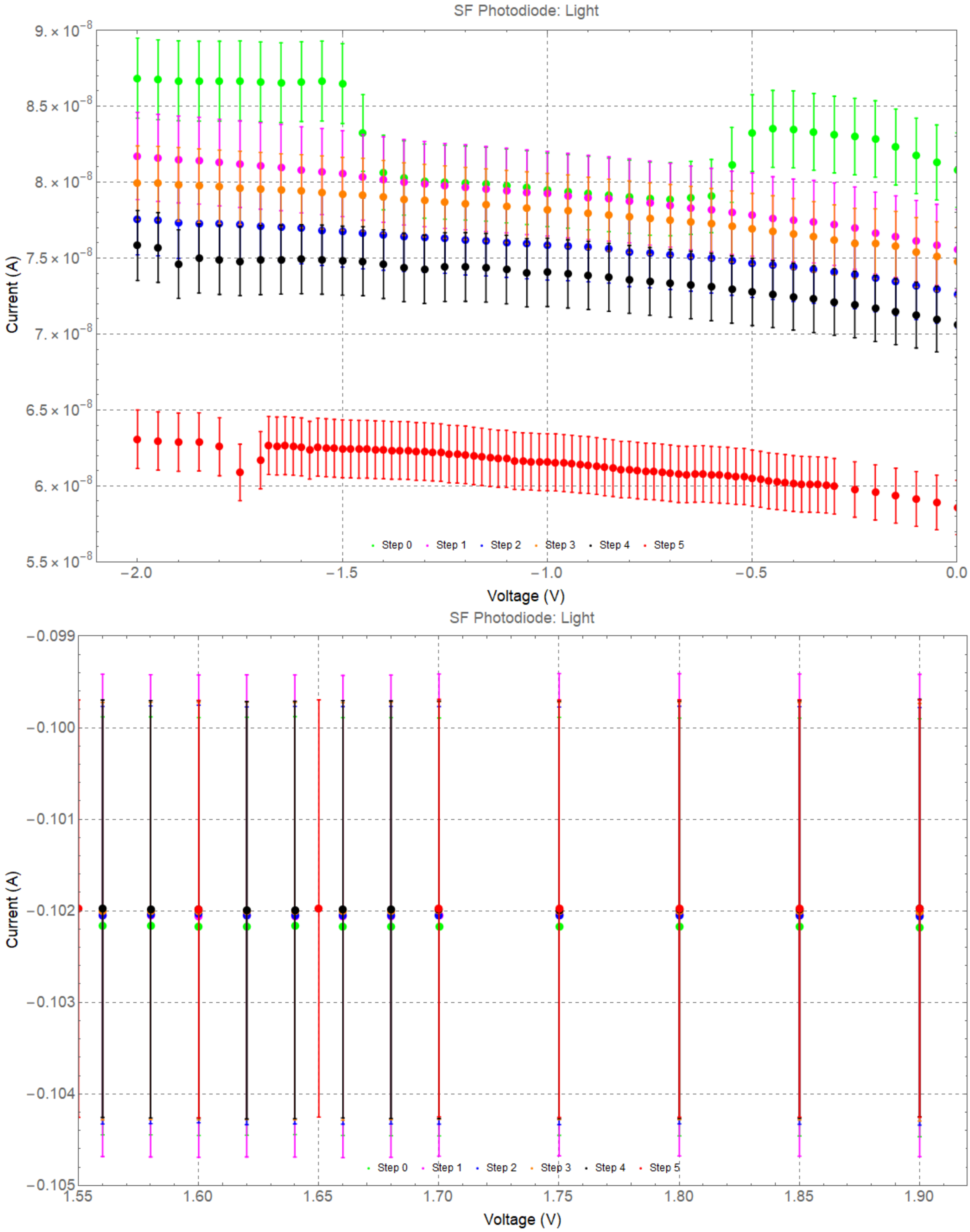

Figure A.19: SF photodiode's left and right saturation currents in the light, for the 5 irradiation steps.

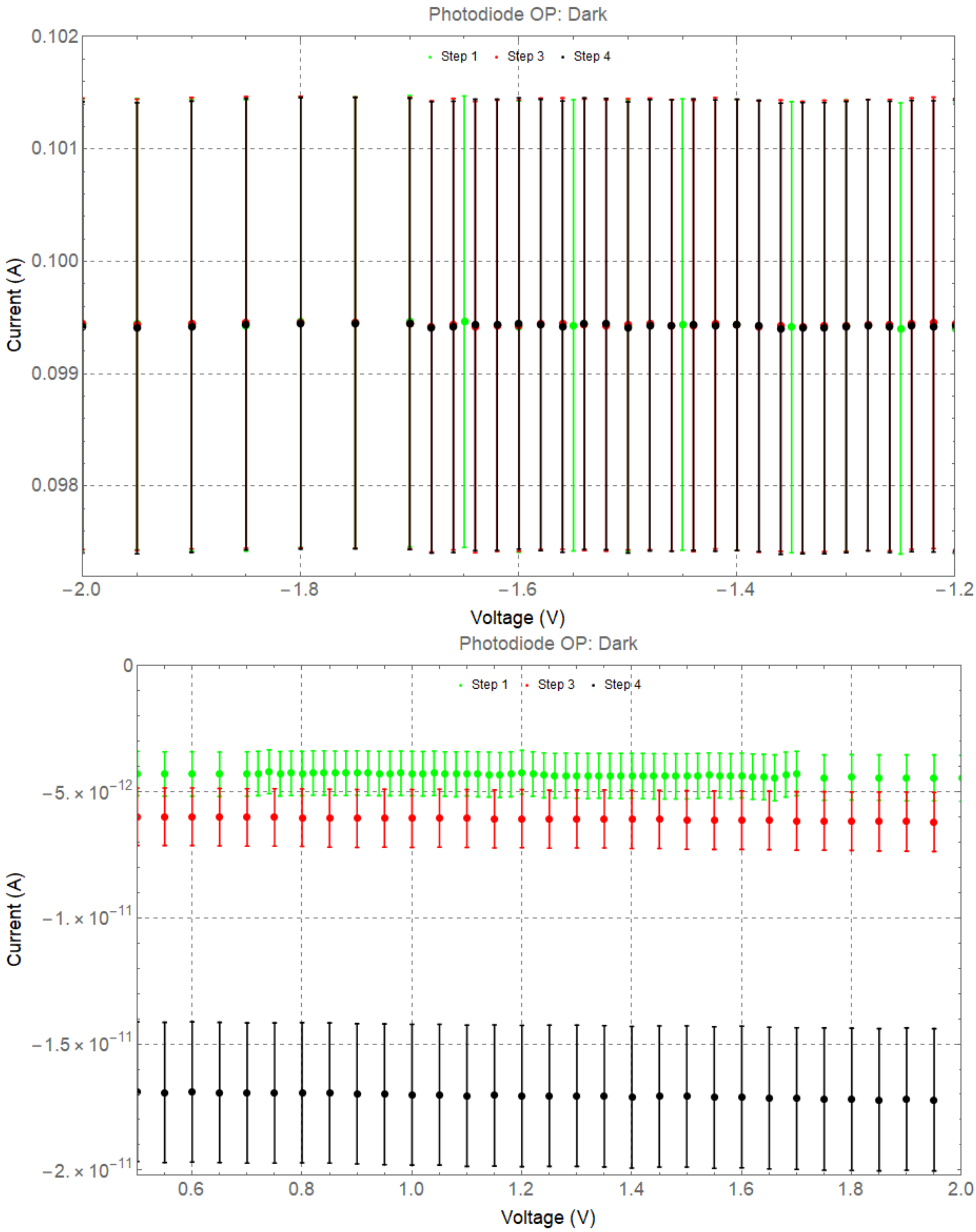

Figure A.20: Reference OP Photodiode's left and right saturation currents in the dark.

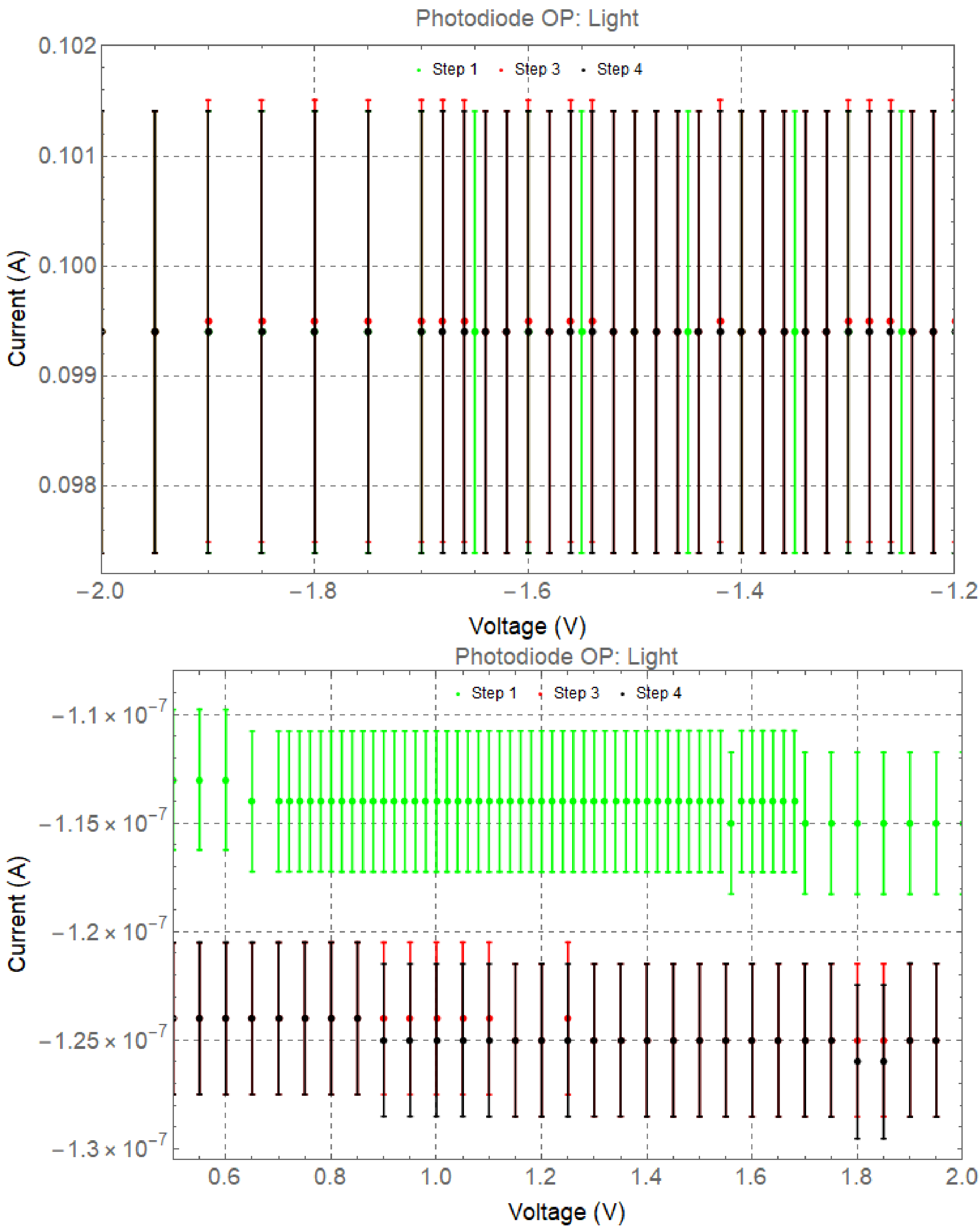

Figure A.21: Reference OP Photodiode's left and right saturation currents in the presence of light.

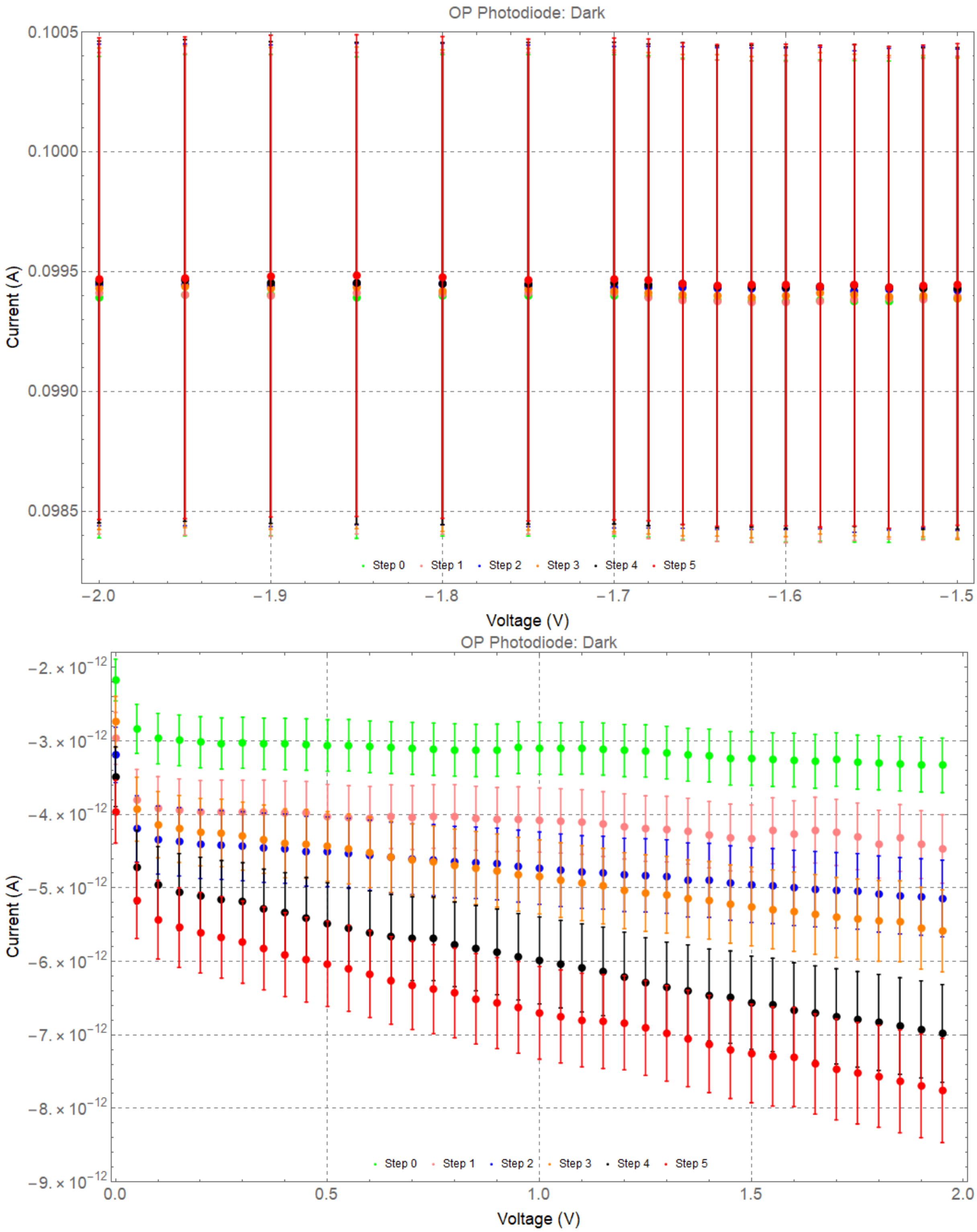

Figure A.22: OP photodiode's left and right saturation currents in the dark, for the 5 irradiation steps.

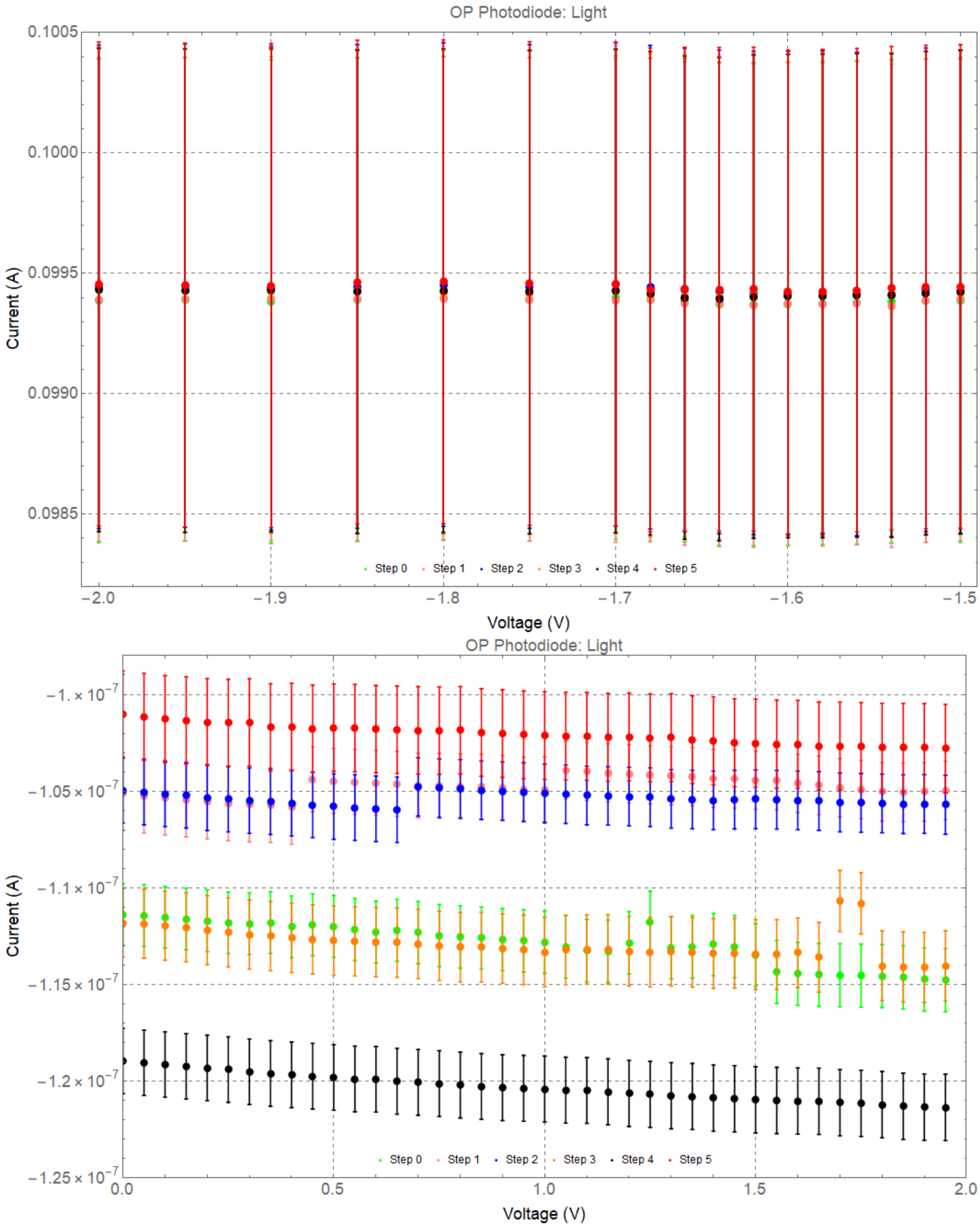

Figure A.23: OP photodiode's left and right saturation currents in the light, for the 5 irradiation steps.

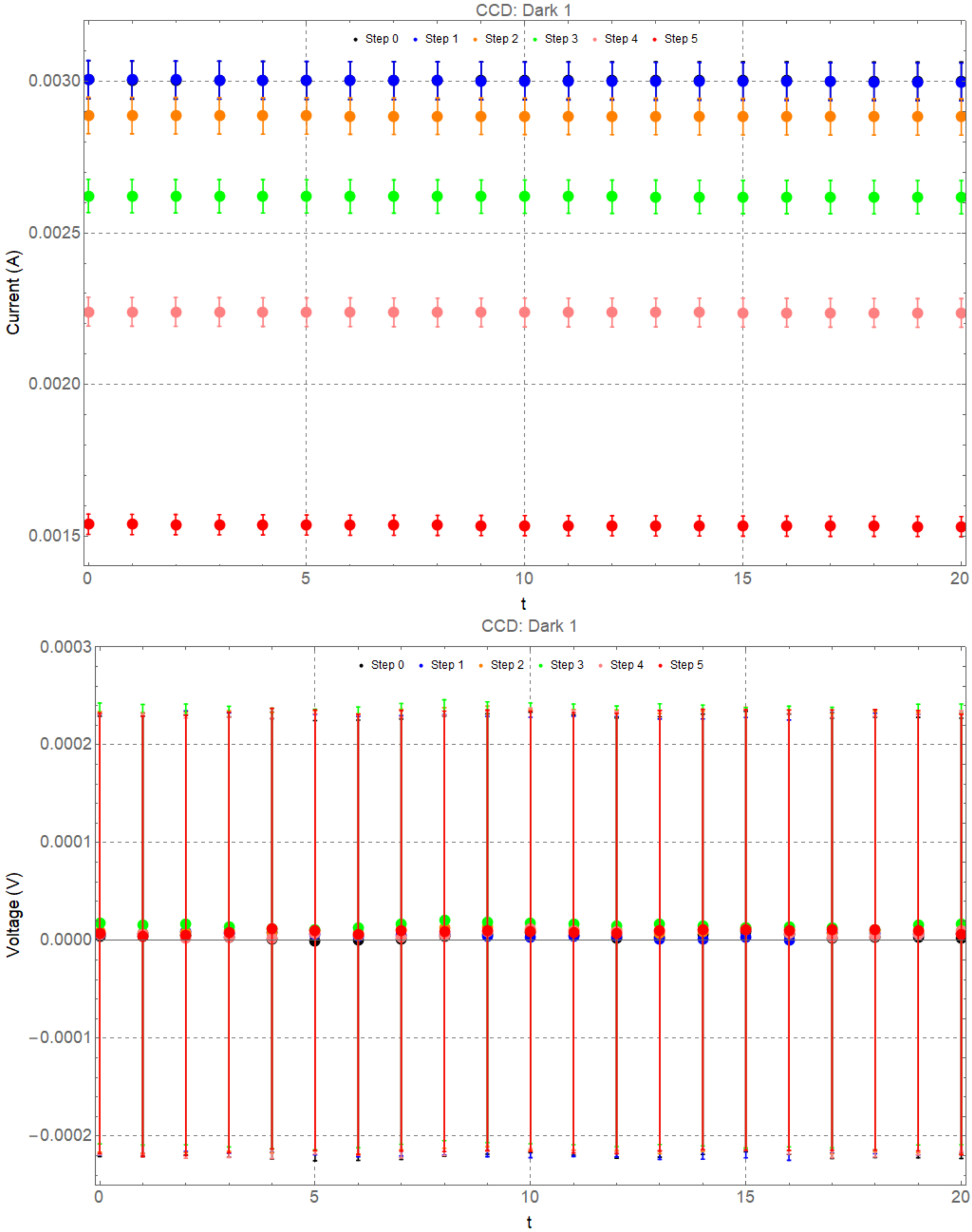

Figure A.24: CCD in the dark, for the 5 irradiation steps. t is an arbitrary time unit of the order of the second.

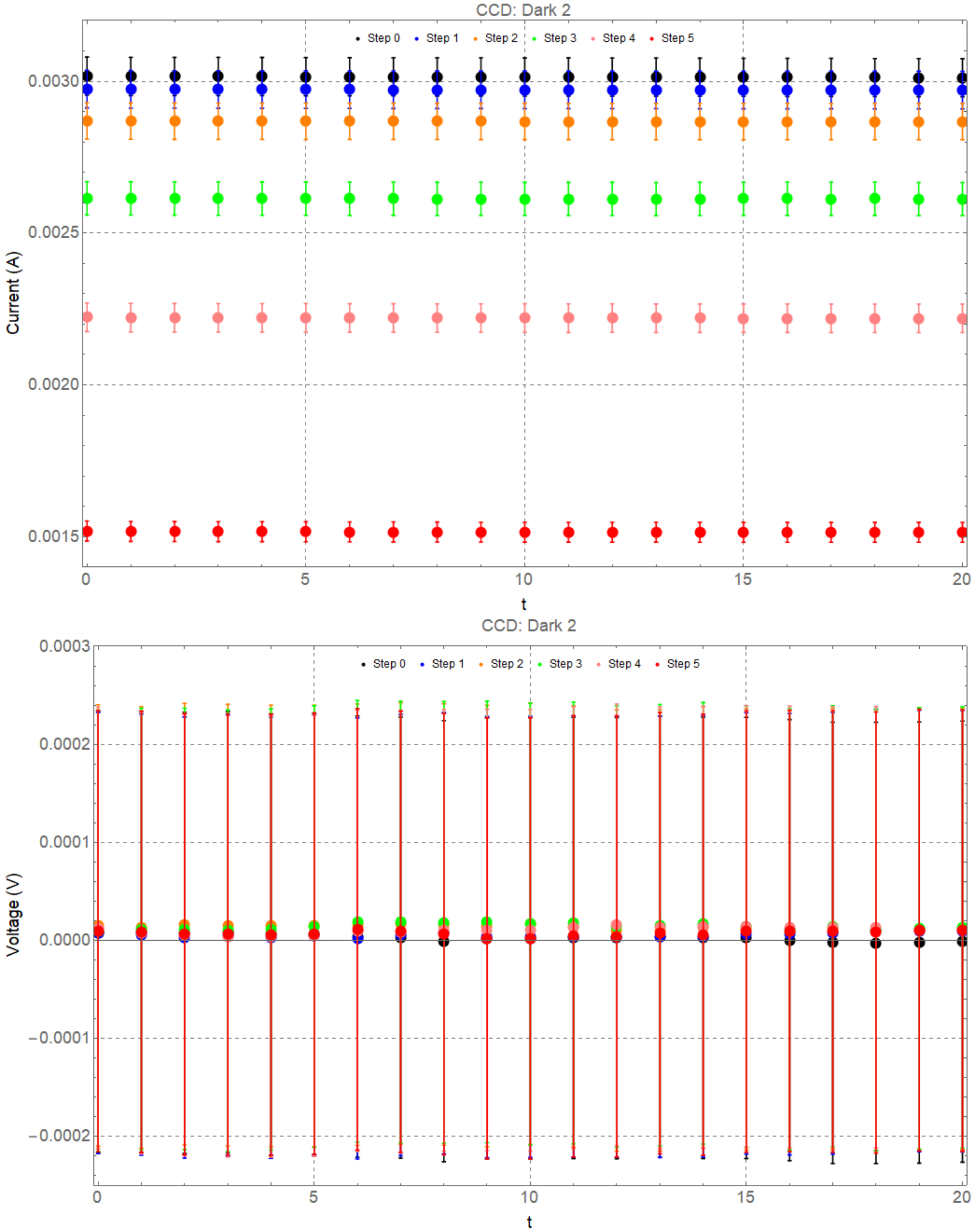

Figure A.25: CCD in the dark after light exposure, for the 5 irradiation steps. t is an arbitrary time unit of the order of the second.

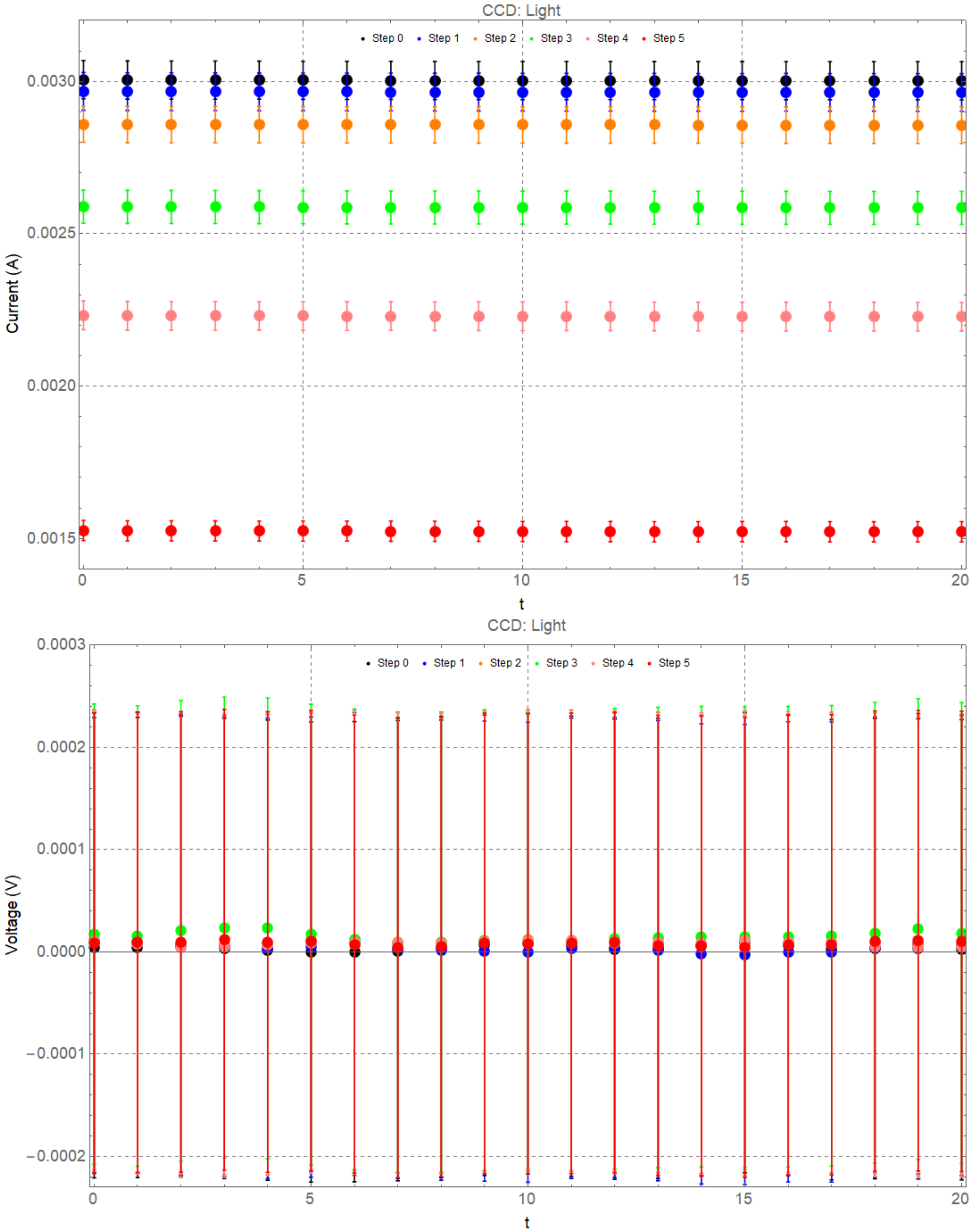

Figure A.26: CCD in the light, for the 5 irradiation steps. t is an arbitrary time unit of the order of the second.